ISSN: 1847-9286
Open Access Journal
www.jese-online.org

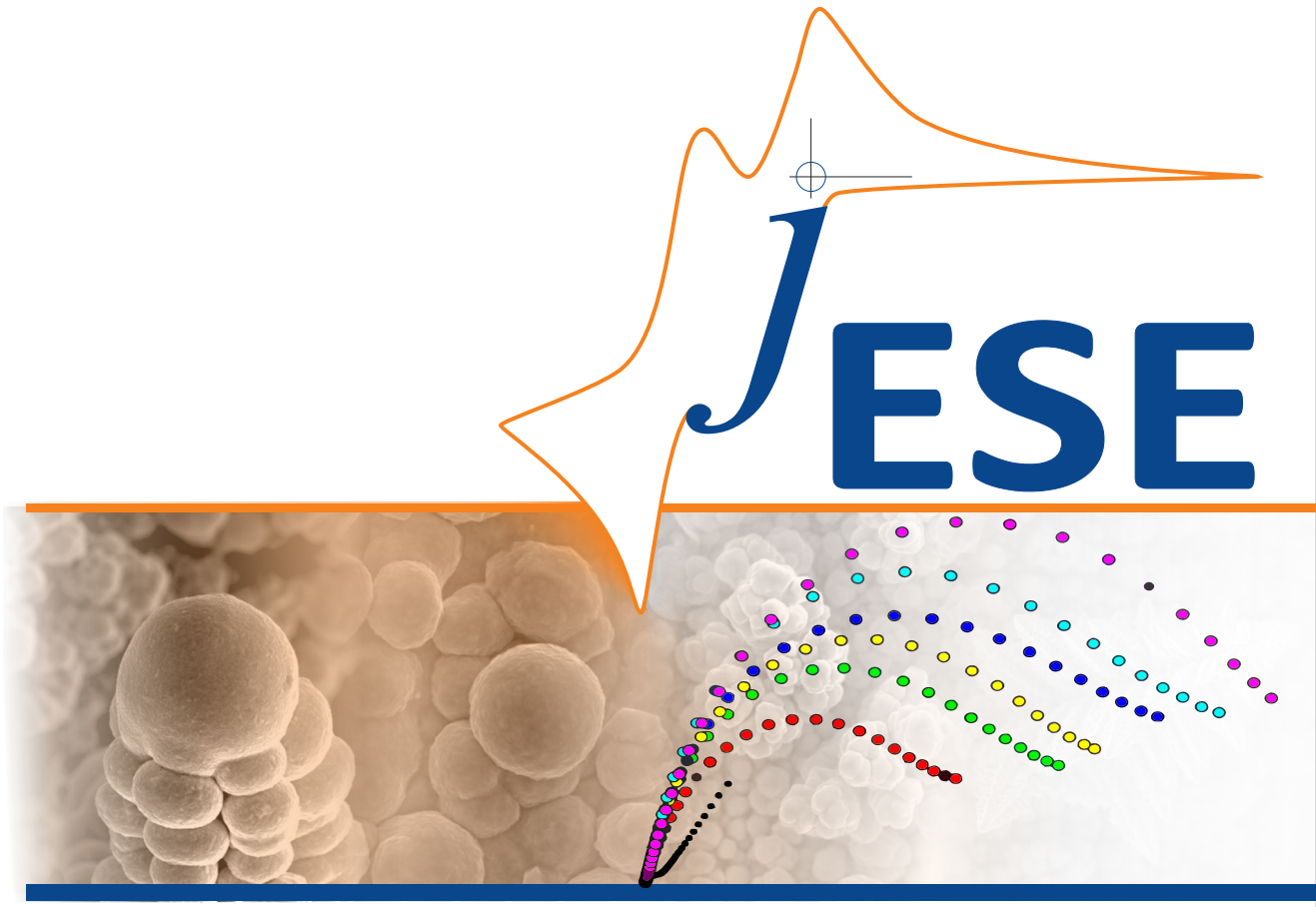

Journal of Electrochemical Science and Engineering

J. Electrochem. Sci. Eng. **8**(**2**) 2018, 111-195

Special Issue dedicated to the
6th Regional Symposium on Electrochemistry – South East Europe

IAPC Publishing

J. Electrochem. Sci. Eng. **8(2)** (2018) 111; DOI: http://dx.doi.org/10.5599/jese.548

Open Access : : ISSN 1847-9286

www.jESE-online.org

Editor's Note

This special issue is the second part of the proceedings of the 6th Regional Symposium on Electrochemistry – South East Europe (RSE–SEE 6), held in Balatonkenese, Hungary, from 11–15 June 2017 (part 1 has been published in J. Electrochem. Sci. Eng. 8(1) (2018)). These are some of the best papers presented at the RSE-SEE 6 meeting and reflect the broad interests of the electrochemical community, including both new techniques and application areas. Since its start in 2008, the series of RSE-SEE symposia provides *a* stimulating international forum for electrochemistry researchers to share their current research results. Following this tradition, more than 110 participants from 24 countries presented papers in Balatonkenese and discussed recent progress in electrochemistry and electrochemical engineering.

I would like to thank the authors for their contribution, the reviewers for their professional work and the jESE-Editorial Office for their assistance in the Proceedings publication. Also, I would like to acknowledge the financial and other support of the Hungarian Academy of Sciences, the International Society of Electrochemistry, the Furukawa Electric Group, Jászplasztik, Ametek, Zahner, Metrohm, PalmSens, Ivium, and Paks Nuclear Power Plant.

The next 7th Regional Symposium on Electrochemistry – South East Europe will be organized jointly with the 8th Kurt Schwabe Symposium in Croatia in the late spring of 2019.

***Gyözö G. Láng**, Guest Editor*

J. Electrochem. Sci. Eng. **8(2)** (2018) 113-127; DOI: http://dx.doi.org/10.5599/jese.478

Open Access : : ISSN 1847-9286

www.jESE-online.org

Original scientific paper

Enhancement of the cerium oxide primer layers deposited on AA2024-T3 aircraft alloy by preliminary anodization

Stephan Kozhukharov[1,✉], Christian Girginov[2]

[1]*LAMAR – Laboratory, University of Chemical Technology and Metallurgy – Sofia, 8 "Kliment Okhridsky" Blvd. 1756, Sofia, Bulgaria*

[2]*Department of Chemical Sciences, University of Chemical Technology and Metallurgy – Sofia, 8 "Kliment Okhridsky" Blvd. 1756, Sofia, Bulgaria*

Corresponding authors e-mail: ✉stephko1980@abv.bg; Tel.: +359 899 83 72 82

Received: November 28, 2017; Revised: February 2, 2018; Accepted: February 8, 2018

Abstract

The possibility for combination between anodized aluminum oxide (AAO) and cerium oxide primer layer (CeOPL) for elaboration of efficient protective coatings for AA2024-T3 aircraft alloy is proposed in the present research. The combined AAO/CeOPL coating characterizations include electrochemical impedance spectroscopy (EIS) combined with linear voltammetry (LVA), for extended times (until 2520 hours) to a model corrosive medium (3.5 % NaCl). Topographical and cross-sectional (SEM and EDX) observations were performed in order to determine the AAO/CeOPL film thickness and composition. The AAO/CeOPL layer durability tests were confirmed by standard neutral salt spray (NSS). The data analysis from all the used measurement methods has undoubtedly shown that the presence of AAO film significantly improves the cerium oxide primer layer (CeOPL) protective properties and performance.

Keywords

AA2024-T3 alloy; anodization; Cerium oxide primer layers; Barrier ability; Durability

Introduction

Although the anodization process is well investigated for pure aluminum [1], its highly doped alloys reveal significant deviations from the expected behavior, due to their compositional and structural heterogeneity [2-9]. In the latter case, the intermetallic inclusions entirely predetermine the mechanism and kinetics of both the primer protective layer deposition and the corrosion processes. Thus, the method applied for preliminary surface treatment completely predetermines the chemical composition of the Al-oxide surface layer in sense of correlation between anhydrous aluminum oxide Al_2O_3 and crystalline boehmite (AlOOH), the hydroxide and adsorbed water contents, *etc.* [10,11]. Besides, the surface oxide layer composition, thickness and properties are

of crucial importance for the primer coating layer adhesion [12,13]. Thus, in a previous work it was demonstrated that the anodization in sulfuric acid enables the growth of rather thick anodized alumina oxide (AAO) layers [14], efficiently compensating the AA2024-T3 heterogeneity.

On the other hand, the cerium conversion coatings (CeCC), appear to be an efficient environmentally compliant chromium substitute [15,16]. However, it is widely accepted to treat the metallic substrate only by chemical or mechanical methods [14,16], prior to CeCC deposition. Consequently, the preliminary anodization prior to cerium oxide primer layer (CeOPL) deposition should have a remarkable beneficial effect on the performance of the obtained AAO/CeOPL conjunction. The obtained double layer coating systems should possess significantly extended durability and enhanced barrier properties, providing reliable and durable corrosion protective ability. The expected synergism between the AAO and CeOPL is not limited only to the additive effect between the AAO and CeOPL barrier properties but it also includes CeOPL adhesion enhancement, due to the AAO porosity, providing enlarged contact surface area. Furthermore, the porous thick AAO provide uniform Ce-oxide distribution and thicker CeOPL layers. In this case, according to various authors the CeOPL layers should possess significant adhesion, predetermined by the Al–O–Ce covalent bonds composing the interfaces of the entire Al/AAO/CeOPL conjunction [17-21]. Finally, it is worth mentioning that the anodization procedure is easily controllable and provides AAO parameters variation via relatively simple regime parameter control. As a conclusion of all the above-mentioned facts, the combination between AAO and CeOPL should provide rather extended corrosion protective capabilities, being really successful strategy for efficient corrosion protection of various aluminum and other metallic substrates.

The aim of the present study is to determine the impact of the preliminary anodization process duration on the subsequent cerium oxide layer (CeOPL) properties and behavior in a model corrosive medium.

Experimental

Four sets of three AA2024-T3 plates were submitted to a sequence of procedures for repeatable AAO/CeOPL bi-layer primer coating deposition. Initially, each sample was etched in 50g/l NaOH alkaline medium at 60 °C, and desmutted in diluted HNO_3 (1:1 v/v). Each procedure was performed for 2 min, with subsequent vigorous washing with tap water for at least 2 min. Afterwards, the preliminary treated specimens were additively cleaned by distilled water and mounted in a two-electrode cell with similar design as described in a previous work [2]. This cell ensured uniform anodization of circular area of a 4 cm^2. The cathode was platinum mesh and the electrolyte was composed of 15 %wt. H_2SO_4 solution. The anodization procedures were performed in galvanostatic regime (15 mA cm^{-2}), in triplicate for 12, 24, or 48 min at room temperature and continuous stirring at 120 rpm.

This procedure was followed by spontaneous CeOPL deposition for 4 min at 60 °C, in cerium containing aqueous mixture. It was preliminary prepared by mixing of 16.8 g. of 98 % anhydrous diammonium pentanitrocerate ($(NH_4)_2Ce(NO_3)_5$, Fluka Chemica -Switzerland), 20.0 g. NaCl (Sigma-Aldrich) and 5.0 ml. of 30 % H_2O_2 (Sigma-Aldrich) in a volumetric flask (1000 ml.). This stock solution was used for all the depositions done. The specimen assignations are shown in Table 1.

Electrochemical studies were performed periodically (once a week), during continuous exposure to the 3.5 % NaCl model corrosive medium. The measurements were performed using electrochemical impedance spectroscopy (EIS), from 10 kHz to 10 mHz, distributed in 7 frequency steps per decade.

Table 1. *Assignations of the investigated specimens*

		CeOPL coated sets of samples		
Samples No	References	Anodized for 12 min	Anodized for 24 min.	Anodized for 48 min
1	1S0	1S12	1S24	1S48
2	2S0	2S12	2S24	2S48
3	3S0	3S12	3S24	3S48

The AC signal amplitude was 15 to 45 mV, according to open circuit potential (OCP). Its amplitude was determined as the lowest possible value, enabling the acquisition of readable impedance spectrum. It is worth noting that when the amplitude was too high, inductance appeared, indicating electrode polarization. The EIS spectra, as well as all the rest electrochemical measurements were recorded versus (Ag/AgCl 3 M KCl) reference electrode. The EIS spectra acquisitions were followed by linear voltammetry. The voltammetric measurements were performed in subsequence of cathodic (from 30 to –600 mV) and anodic (from –30 to 600 mV) ranges, both at 10 mV s^{-1} scan rate. These measurements were performed in similar cells, but without stirring. Besides, the exposed area was lower (2 cm^2), in order to avoid undesirable edge effect phenomena.

The resulting film morphology and thickness was determined by scanning electron microscopy, (SEM) performed by TESCAN, SEM/FIB LYRA I XMU working at 30 kV. The SEM observations were combined by elemental analysis, with energy dispersion spectroscopy (EDX) using energy dispersion spectrometer Quantax 200 of BRUKER.

In order to determine the coating performance in severe service conditions, neutral salt spray (NSS) test procedure was performed, according to ISO 9227 standard. This procedure was performed on nine square samples of the same alloy, but with larger dimensions (60×60 mm). Prior to the test procedures, AAO/CeOPL double layered coatings were deposited following the procedures described above. The surface areas of the double coatings were with 40 mm of diameter, (providing 12.50 cm^2). The test procedure was performed for one complete week cycle (168 h) in VSN 1000 humidity chamber (Heraeus-Vötsch GmbH, Germany) by spraying of 5 % NaCl aqueous solution with pH range between 6.5 and 7.2. The samples were positioned at 20 ± 5 ^{o} of slope. The in-chamber humidity was high enough to enable water to condense of at least 1 to 2 ml h^{-1}. The corrosion impact rate was observed visually and estimated as a number of localized corrosion damaged domains from the entire exposed surface, according to the Bulgarian National Standard, BDS 15258-81, method C.

Results and discussion

Performance in a model corrosive medium - The performance of the obtained AAO/CeOPL double layers was determined by electrochemical measurements executed once of week during extended exposition of the investigated samples to 3.5 % NaCl model corrosive medium. This approach enabled determination of the corrosion protective properties of the obtained oxide bilayers, conditionally divided into: barrier ability and durability [22].

Barrier ability - This property is actually the capability of any coating to obstruct the corrosive species access to the metallic surface. It can be evaluated by the electrical resistance increase, determined by electrochemical measurements (EIS and LVA), performed at the initial exposition period. Although the initial measurements were performed at the 24th hour of exposure to the NaCl solution, it was preferred to represent the results acquired after 168 hours of exposition. After one week of exposure, the reference samples, (prepared by CeOPL deposition without preliminary anodization) were obviously affected by pitting corrosion unlike the double layered specimens. The average EIS spectra, acquired after 168 hours of exposure are shown in Fig. 1.

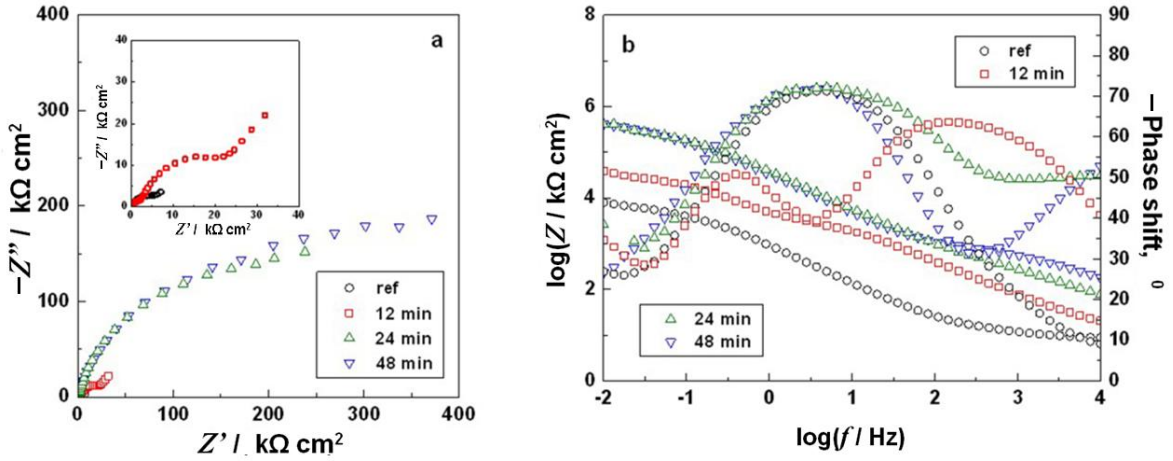

Figure 1. *EIS spectra acquired after 168 hours of exposure for the investigated specimens for CeOPL deposited coatings after 0, 12, 24 and 48 minutes of preliminary anodization.*

As can be seen from Fig 1, the average spectra obtained for the respective sample sets are rather distinguishable among themselves.

The already corroded references (0 minutes of anodization) show simple spectra. Their Nyquist plots consist of slightly depressed semi-circles and Warburg diffusion tails (*i.e.* sloped straight lines). Besides, the phase shift/frequency lines in the Bode plots showed only one, very narrow minimum at about 10 Hz.

The maxima in the spectra of the combined coating layers were wide (due to the overlapping of at least two peaks). Obviously, the appearance of additional peak is a contribution of the AAO formed during the anodization. This supplemental layer contributes for the increase of the total impedance logarithm (log|*Z*|) values, registered at 10 mHz, as well. These values increased from 10^4 Ω cm^2 for the references to almost 10^6 Ω cm^2 for the combined coatings.

The impedance spectra acquired after 168 hours of exposure were fitted to two different equivalent circuits (Fig. 2a, and b).

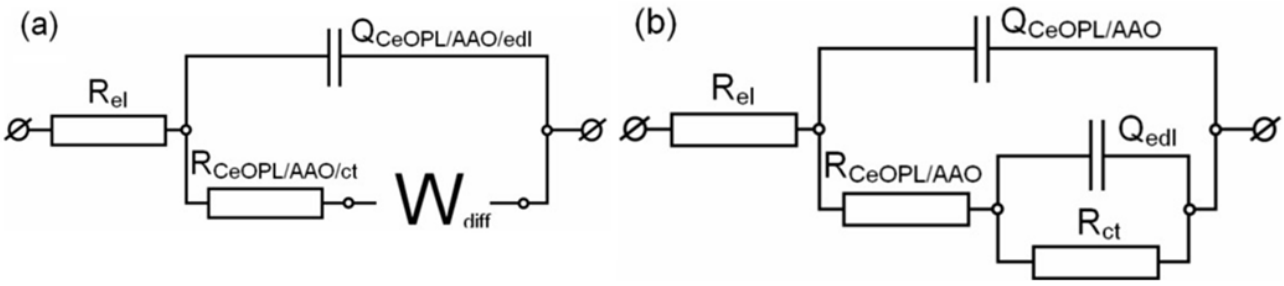

Figure 2. *Equivalent circuits used for EIS-data fitting*

R_{el} *– 3.5 % NaCl electrolyte resistance;* $Q_{CeOPl/AAO/edl}$ *– Total CPE of the CeOPL, AAO, and the metal/electrolyte electric double layer;* $R_{CeOPl/AAO/ct}$ *- Total resistance of the CeOPL, AAO, and the charge transfer across the metal/electrolyte interface;* W_{diff} *– Warburg element for description of the diffusion of the corrosive species across the CeOPL defects;* $Q_{CeOPl/AAO}$ *– CPE of the AAO/CeOPL interface;* $R_{AAO/CeOPl}$ *- Resistance of the AAO/CeOPL interface;* Q_{edl} *– CPE of the electyric double layer the metal/electrolyte interface;* R_{ct} *- charge transfer across the metal/electrolyte interface*

Thus, the spectra of the corroded reference samples have simple shapes, corresponding to only one RQ unit (parallel resistance and constant phase element circuit), which includes a Warburg diffusion element, related to the diffusion limitations against the access of corrosive species towards the metallic surface, across the surface layer defects. All the rest specimens (with additional AAO underlayer) revealed two consecutive RQ units.

Each one of the acquired impedance spectra, obtained after 168 hours of exposure was submitted to numerical fitting analysis by the equivalent circuits (Fig. 2). The obtained data for the impedance spectra elements are shown in Tables 2 and 3.

Table 2. *Fitting* results *of the EIS spectra recorded after 168 hours for the referent CeOPL coated specimens*

Element	Unit	Sample **1S0**	Sample **2S0**	Sample **3S0**
R_{el}	$\Omega\ cm^2$	19.44 ± 0.59	19.18 ± 0.49	20.02 ± 0.59
$Q_{coat+oxy+ct}$	$s^n\ \Omega^{-1}\ cm^{-2}$	0.76 ± 0.03×10^{-4}	1.19 ± 0.04×10^{-4}	1.12 ± 0.05×10^{-4}
n	-	0.83 ± 0.95	0.82 ± 0.91	0.81 ± 0.01
$R_{coat+oxy+edl}$	$\Omega\ cm^2$	17.98 ± 1.40×10^3	12.56 ± 0.87×10^3	7.68 ± 0.46×10^3
W_{diff}	$S^{0.5}\ \Omega^{-1}\ cm^{-2}$	3.68 ± 0.68×10^{-4}	6.50 ± 1.30×10^{-4}	12.70 ± 0.29×10^{-4}

The numerical data for the referent samples (Table 2) show relatively low deviations. These specimens, with clear corrosion features (*i.e.* multitudes of pits) have shown total admittance between 0.29×10^{-4} and 1.12×10^{-4} $s^n\ \Omega^{-1}\ cm^{-2}$ and ohmic resistance between 7.68 and 19.98 kΩ cm^2. These values are in the typical range for corroded bare AA2024-T3 alloy, established in previous studies [23-25]. Besides, the data fitting for these specimens required addition of Warburg element. This fact is an evidence of free diffusion of corrosive species across both the native Al-oxide and CeOPL layers. Both these findings indicated that the directly deposited CeOPL layer does not possess any protective activity after 168 hours of exposure to 3.5 % NaCl model corrosive medium. That was the reason for termination of the exposure tests after this period.

On the other hand, the data results for all the CeOPL coated specimens after anodization were more appropriate for fitting to the other equivalent circuit (Fig. 2b), composed by two-time constants. It should be noted that these time constants are not related to the interfaces between the AAO and CeOPL layers, but rather these correspond to the interfaces between the AAO/CeOPL conjunction, the AA2024-T3 metallic base and the aqueous NaCl electrolyte. Probably, this conjunction is composed by covalent Ce-O-Al bonds, suggesting that there is not clear interface between the AAO and CeOPL layers. Besides, both AAO and CeOPL layers are composed by metallic oxides with apparent dielectric properties.

Due to these reasons, the equivalent circuit used for the reference specimens (Fig. 2a) was inappropriate for EIS data result fitting of the spectra acquired for the preliminary anodized AA2024-T3 samples. The second equivalent circuit (Fig. 2b) has shown to be more suitable and the fitting results are shown in Table 3.

The data acquired by the EIS spectra fitting to the equivalent circuit (Fig 2b) possess different deviations rates among the results for each sample. Thus, the CeOPL specimens coated, after only 12 min of anodization possess remarkable deviations, in the range of entire orders of magnitude. This fact indicates that this anodization time is obviously insufficient for creation of thick enough AAO films with uniform coverage. Besides, probably the randomly distributed intermetallic inclusions of the alloy substrate interrupt this film.

The comparison between the charge transfer resistance (R_{ct}) data in Table 3 with the combined resistance ($R_{coat+oxy+edl}$), in Table 2 show obvious barrier ability elevation after the preliminary anodization. Consequently, the observed barrier ability improvement after anodization is an indication for the beneficial role of the preliminary anodization procedure on CeOPL performance.

Following the concept for island growth of Ce oxide layers [26], it should be assumed that the CeOPL formation begins from exactly these intermetallics. Besides, the most active CeOPL growth initiation centers should be the copper rich S-phase and θ-phase inclusions [3], according to the following reactions [3, 26]:

Table 3. *Fitting results of the EIS spectra acquired after 168 hours of exposure for the anodized, CeOPL coated specimens*

12 minutes of anodization				
Element	Unit	Sample **1S12**	Sample **2S12**	Sample **3S12**
R_{el}	$\Omega\ cm^2$	15.36 ± 0.21	22.78 ± 2.54	33.06 ± 8.95
$Q_{coat+oxy}$	$s^n\ \Omega^{-1}\ cm^{-2}$	$4.35 \pm 0.06\times10^{-5}$	$0.79 \pm 0.10\times10^{-5}$	$0.15 \pm 0.05\times10^{-5}$
n		0.78 ± 0.002	0.77 ± 0.02	0.68 ± 0.003
$R_{coat+oxy}$	$\Omega.cm^2$	$23.71 \pm 0.96\times10^{3}$	$6.72 \pm 1.15\times10^{3}$	$7.68 \pm 0.34\times10^{3}$
Q_{edl}	$s^n\ \Omega^{-1}\ cm^{-2}$	$30.92 \pm 5.18\times10^{-5}$	$2.89 \pm 0.55\times10^{-5}$	$0.05 \pm 0.08\times10^{-5}$
n		0.75 ± 0.08	0.67 ± 0.04	0.95 ± 0.01
R_{ct}	$\Omega\ cm^2$	$2.42 \pm 0.24\times10^{5}$	$0.91 \pm 0.08\times10^{5}$	$78.40 \pm 5.42\times10^{5}$
24 minutes of anodization				
Element	Unit	Sample **1S24**	Sample **2S24**	Sample **3S24**
R_{el}	$\Omega\ cm^2$	16.46 ± 1.69	45.86 ± 6.28	17.28 ± 1.73
$Q_{coat+oxy}$	$s^n\ \Omega^{-1}\ cm^{-2}$	$2.52 \pm 0.48\times10^{-6}$	$1.78 \pm 0.32\times10^{-6}$	$0.90 \pm 0.09\times10^{-6}$
n		0.71 ± 0.01	0.76 ± 0.02	0.71 ± 0.02
$R_{coat+oxy}$	$\Omega\ cm^2$	$2.39 \pm 0.44\times10^{3}$	$1.36 \pm 0.20\times10^{3}$	$4.62 \pm 0.23\times10^{3}$
Q_{edl}	$s^n\ \Omega^{-1}\ cm^{-2}$	$1.31 \pm 0.42\times10^{-6}$	$1.15 \pm 0.24\times10^{-6}$	$0.88 \pm 0.08\times10^{-6}$
n		0.86 ± 0.04	0.87 ± 0.03	0.94 ± 0.02
R_{ct}	$\Omega\ cm^2$	$4.91 \pm 0.19\times10^{5}$	$7.58 \pm 0.31\times10^{5}$	$30.64 \pm 1.32\times10^{5}$
48 minutes of anodization				
Element	Unit	Sample **1S48**	Sample **2S48**	Sample **3S48**
R_{el}	$\Omega.cm^2$	27.44 ± 6.91	25.82 ± 12.12	71.60 ± 17.95
$Q_{coat+oxy}$	$s^n\ \Omega^{-1}\ cm^{-2}$	$6.52 \pm 0.02\times10^{-6}$	$2.43 \pm 0.09\times10^{-6}$	$0.96 \pm 0.07\times10^{-6}$
n		0.58 ± 0.003	0.63 ± 0.004	0.67 ± 0.008
$R_{coat+oxy}$	$\Omega.cm^2$	$3.74 \pm 0.18\times10^{3}$	$2.60 \pm 0.06\times10^{3}$	$5.74 \pm 0.14\times10^{3}$
Q_{edl}	$s^n\ \Omega^{-1}\ cm^{-2}$	$0.90 \pm 0.10\times10^{-6}$	$1.36 \pm 0.07\times10^{-6}$	$1.93 \pm 0.07\times10^{-6}$
n		0.97 ± 0.02	0.96 ± 0.009	0.94 ± 0.009
R_{ct}	$\Omega\ cm^2$	$2.70 \pm 0.06\times10^{5}$	$11.16 \pm 0.31\times10^{5}$	$111.20 \pm 1.22\times10^{5}$

Oxygen reduction:

$$O_2 + 2H_2O + 4e^- \rightarrow 4OH^- \quad (1)$$

Formation of intermediated complex species:

$$2Ce^{3+}_{aq.} + H_2O_2 + 2OH\text{-} \rightarrow Ce(OH)_2{}^{2+}_{aq.} \quad (2)$$

Reaction of the obtained complex ions with hydroxyl ions near to the metallic surface:

$$Ce(OH)_2{}^{2+}_{aq.} + 2OH^- \rightarrow Ce(OH)_4 \quad (3)$$

Subsequent conversion of the cerium hydroxides to the respective oxides:

$$Ce(OH)_4 \rightarrow CeO_2 + 2H_2O \quad (4)$$

According to the authors, these reactions proceed accompanied by the following supplemental reaction of direct interaction of the Ce^{3+} with the hydroxyl ions:

$$Ce^{3+} + 3OH^- \rightarrow Ce(OH)_3 \quad (5)$$

However, all this chain of consecutive reactions is strongly dependent on the available anodic area, composed by the Al-matrix under the oxide layer defects, since it provides the electrons necessary for the oxygen reduction and the resulting in OH- ion generation. Namely, the predominant hydroxyl ion generation (*i.e.* alkalization) near these intermetallics causes $Ce(OH)_3$ and/or $Ce(OH)_4$ precipitation. Consequently, the oxygen reduction cathodic reaction rate on the intermetallics is strongly dependent on the anodic Al-dissolution (Reaction 6):

$$Al^0 \rightarrow Al^{3+} + 3e^- \quad (6)$$

Applying this model for the CeOPL deposited AA2024-T3 samples after anodization, it can be anticipated that the AAO film hinders the CeOPL formation, because it covers the Al-matrix anodic

area, necessary to supply electrons for the cathodic OH- generation reactions, and the resulting Ce-hydroxide precipitation.

Nevertheless, this concept is in contradiction with the data in Table 3. All the acquired resistance data (*i.e.* $R_{coat+oxy}$ and R_{ct}) reveal remarkably distinguishable dissipations among the specimens of each group (*e.g.* 12, 24 and 48 min of anodization). Simultaneously, the result deviations possess very similar deviation rates and orders of magnitude among the respective sample groups. Thus, no clear trend of these values was observed, although the obvious oxide layer thickness increases within the anodization procedure continuation, established in a previous work [27]. These facts provide undoubted evidence for the low oxide layer density due to its probably porous structure. In addition, the difference between the equivalent circuits suitable for the EIS-data fitting of the references and the anodized specimens reveal completely different mechanism of CeOPL deposition after AAO formation. Following the concepts of Arenas and Damborenea [28], it can be assumed that the AAO/CeOPL conjunction is alumina layer with partial substitution by Ce-ions. Obviously, the CeOPL layers deposited on thicker AAO layer, formed at extended anodization times possess better coverage. Indeed, Conde *et al.* [29] remark that the CeOPL layer formation is based on chemisorption processes on the superficial hydrated oxide layer of the aluminum, as follows:

$$\text{-Al-OH}^{2+} \leftrightarrow \text{-AlOH} + \text{H+} \quad (7)$$

$$\text{-Al-OH} + Ce^{3+} \leftrightarrow [\text{-Al-O}\cdots Ce(III)]^{2+} + 2H^{+} \quad (8)$$

Consequently, CeOPL deposition mechanism alteration occurs on the more completely hydrated AAO layers, occupying the entire metallic surface. Thus, the CeOPL deposition follows the mechanism, proposed by Conde *et al.* [29], described by reactions (7) and (8).

These trends of barrier ability enhancement by the preliminary anodization have been evinced by the concordance of the results acquired by both the EIS data analysis and the polarization curves, described below. Fig. 3 illustrates the general trends (of current densities decrease, combined by corrosion potential (E_{corr}) shift in positive direction) for the polarization curves recorded after 168 hours of exposure.

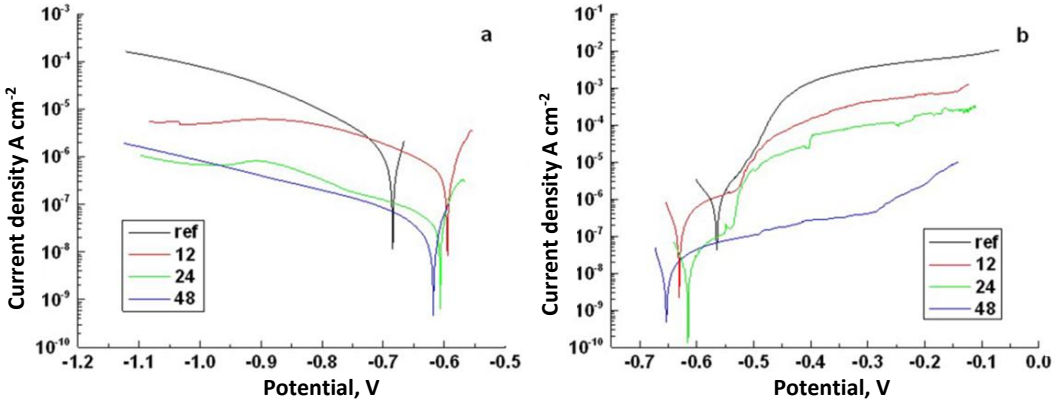

Figure 3. *Cathodic (a) and anodic (b) polarization cures recorded after 168 hours of exposure*

The polarization curves have been submitted to further Tafel plot analysis for determination of E_{corr} and polarization resistance (R_p). The numerical data of the obtained results for all the investigated specimens are represented in Table 4. Some trends can be seen from the inferred, regardless the considerable result dissipation. The largest E_{corr} difference between the cathodic and anodic curves belongs to the reference samples, showing that the relaxation time of about hours is not sufficient for E_{corr} value restoration, after the cathodic curve acquisition. Unexpec-

tedly, the E_{corr} values of the anodic curves are with about 100 mV more positive, although cathodic polarization of the specimens. Thus, during the cathodic curve acquisition, the investigated specimens (being negatively charged) attract cations from the model corrosive medium, like Na^+ and H_3O^+, shifting E_{corr} in positive direction. This assumption is additionally confirmed by the occurrence of Warburg diffusion elements, commented in the previous section.

Table 4. *Tafel plot analysis of the obtained results from the polarization cures, recorded after 168 hours of exposure*

	Cathodic						Anodic					
	E_{corr} / V *vs.* Ag/AgCl			R_p / kΩ cm^2			E_{corr} / V *vs.* Ag/AgCl			R_p / kΩ cm^2		
	1S	2S	3S	1S	2S	3S	1S	2S	3S	1S	2S	3S
Ref.	-0.658	-0.685	-0.718	17.8	14.0	8.6	-0.557	-0.565	-0.536	18.4	10.0	8.4
12 min	-0.628	-0.595	-0.611	300.0	240.0	160.8	-0.589	-0.631	-0.608	248.6	220.0	170.0
24 min	-0.633	-0.607	-0.773	480.0	280.0	196.0	-0.571	-0.615	-0.685	600.80	380.0	214.0
48 min	-0.673	-0.617	-0.639	1980.0	3800.0	2200.0	-0.676	-0.653	-0.614	2345.0	3600.0	2400.0

The cathodic curves acquired from the reference specimens approximated straight lines, possessing indistinguishable curvature. Their slopes are probably result of electrolyte ohmic drop, and diffusion hindering in the electrolyte bulk. All other polarization curves obtained from the preliminary anodized samples had more similar E_{corr} values, with deviations of about 35 to 40 mV. Besides, their cathodic curves stay at lower current densities compared to those of the reference samples. Consequently, the AAO/CeOPL conjunctions possess much better insulating properties, compared to the reference CeOPL monolayers. This inference is additionally confirmed by the relatively higher R_p values of the combined layer coatings, although the considerable value deviations among the samples. In all cases, the CeOPL coated specimens after 48 min of anodization possess at least an order of magnitude higher R_p values, compared to those, anodized for only 12 min. The specimens treated for 24 min have intermediate position, being similar either to the former, or to the latter specimens. The higher barrier ability of the AAO/CeOPL layers suggests extended durability, and this fact was the reason to continue the experiments, related to the sample exposure to the model corrosive medium.

Durability – This property was evaluated by further extension of the sample exposure until corrosion pits appear, combined with regular EIS and LVA measurements, according to the regimes, described in the experimental section. Since this approach has provided a huge number of data collections, only the final measurements will be commented in detail. The sample durability of the specimens increases progressively with the anodization process duration (and the AAO thickness, respectively). Thus, the reference CeOPL monolayers have already failed until the 168th hour of exposure, whereas the AAO/CeOPL layers, obtained by 48 min of anodization have resisted whole 2,520 hours in the model corrosive medium (Fig. 4)

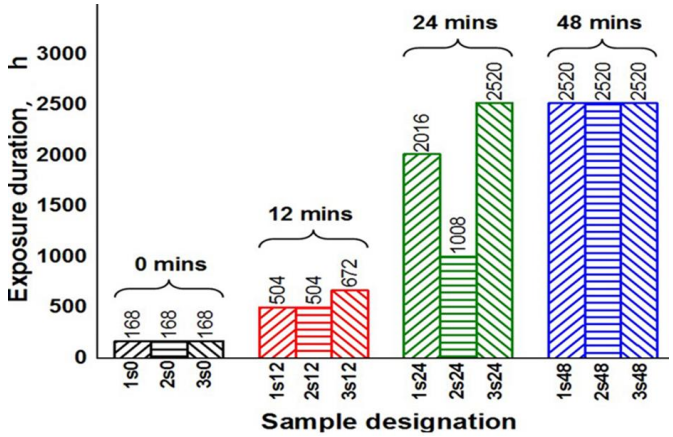

Figure 4. *Durability diagram of the investigated specimens*

The EIS spectra recorded for the final exposure times were appropriated for fitting to the equivalent circuit shown in Fig. 2b. Since the CeOPL coated specimens, after 24 min of anodization fall between the anodized for 12 and 48

min, their results were not submitted to fitting. Furthermore, the significant difference of the exposure times registered for these samplers (*e.g.* the anodized for 24 min) should lead to remarkable deviation among the respective EIS data fitting. The results, obtained from the final EIS spectra fitting are represented in Table 5.

It is worth mentioning, that at the final measurements (Fig. 4) all the preliminary anodized specimens possessed superior charge transfer resistance (R_{ct}) values (Table 5), compared to those of the references after 168 hours of exposure (Table 2). Although the fact that the equivalent circuit was appropriate for data fitting in both cases of the specimens, preliminary anodized for 12 and 48 min, their spectra had rather distinguishable shapes (Fig. 5). Since the specimens anodized for 24 min have shown great deviations among themselves, their spectra are not shown.

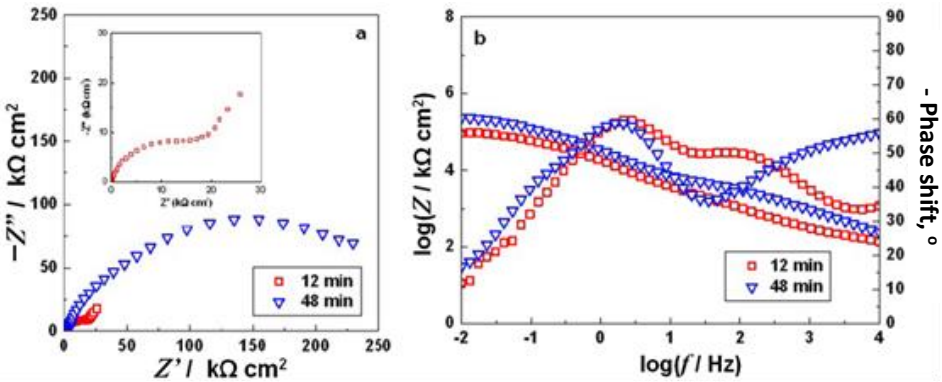

Figure 5. *Averaged EIS spectra Bode plots of CeOPL deposited coatings after 12 and 48 minutes of anodization, acquired at the end of the exposition to the model corrosive medium*

Both the real (Z') and the imaginary ($-Z''$) values of the smples anodized for 48 min are much superior to these of the samples with 12 min of anodization (Fig. 5a). The real impedance component reaches 250 kΩ cm^2 for the thicker AAO layer, whereas in the other case, its value is only 25 kΩ cm^2. Similar difference is observable for the logarithm of the total impedance in the respective Bode plot (Fig. 5b). The $\varphi(f)$-dependence recorded after 2,520 hours of exposure have two clearly distinguishable maxima, related to the AAO and CeOPL layers, at the lower and the higher frequency ranges. These maxima are almost completely overlapped in the EIS spectra acquired after (504/672 hours of exposure) of the samples anodized for 12 min. This fact indicates that the coatings deposited after 48 min of anodization possess residual protective capabilities, although the interruption of their integrity after 2520 hours of exposure to the model 3.5 % NaCl corrosive medium.

The EIS results are further confirmed by the respective LVA measurements, performed after the sample exposure, shown in Fig. 6.

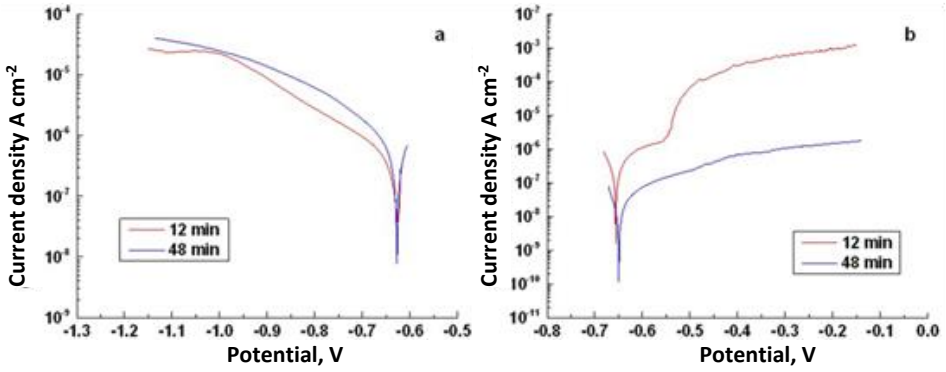

Figure 6. *Cathodic (a) and anodic (b) polarization curves acquired at the end of the exposure of CeOPL coated samples after 12 and 48 minutes of anodization*

The cathodic polarization curves acquired after the corrosion tests for the specimens anodized for 12 and 48 min overlap, where there is obvious difference between the respective anodic curves. This fact is indication for the almost equal cathodic activity in the former case. However, there is a sharp current rise, in the anodic curve of the sample anodized for 12 min, as a result of localized corrosion activity as is proposed elsewhere [30]. Consequently, the corrosion processes proceed with almost the same rate, but with a different mechanism.

Table 5. *Fitting results for the anodized CeOPL coated specimens at the final exposure measurements*

12 minutes of anodization				
Element	Unit	Sample **1S12** After 504 hours	Sample **2S12** After 504 hours	Sample **3S12** After 672 hours
R_{el}	$\Omega\ cm^2$	14.18 ± 0.20	18.92 ± 0.67	57.48 ± 16.28
$Q_{coat+oxy}$	$s^n\ \Omega^{-1}\ cm^{-2}$	$0.68 \pm 0.01\times10^{-4}$	$2.00 \pm 0.06\times10^{-5}$	$1.44 \pm 0.09\times10^{-6}$
n		0.86 ± 0.03	0.82 ± 0.05	0.66 ± 0.06
$R_{coat+oxy}$	$\Omega\ cm^2$	$22.08 \pm 1.00\times10^{3}$	$44.94 \pm 2.36\times10^{3}$	$11.62 \pm 0.74\times10^{3}$
Q_{edl}	$s^n\ \Omega^{-1}\ cm^{-2}$	$0.51 \pm 22.96\times10^{-3}$	$3.42 \pm 12.92\times10^{-4}$	$0.78 \pm 0.08\times10^{-6}$
n		0.95 ± 0.09	0.96 ± 0.01	0.92 ± 0.02
R_{ct}	$\Omega.cm^2$	$49.24 \pm 15.20\times10^{3}$	$10.20 \pm 68.63\times10^{3}$	$3.52 \pm 0.21\times10^{3}$
48 minutes of anodization				
Element	Unit	Sample **1S48** After 2520 hours	Sample **2S48** After 2520 hours	Sample **3S48** After 2520 hours
R_{el}	Ωcm^2	187.20 ± 10.95	85.60 ± 10.46	48.56 ± 3.88
$Q_{coat+oxy}$	$s^n\ \Omega^{-1}\ cm^{-2}$	$0.681 \pm 0.06\times10^{-5}$	$3.22 \pm 0.09\times10^{-6}$	$4.10 \pm 0.43\times10^{-5}$
n		0.65 ± 0.01	0.57 ± 0.03	0.69 ± 0.01
$R_{coat+oxy}$	$\Omega\ cm^2$	$15.06 \pm 4.29\times10^{3}$	$23.04 \pm 0.96\times10^{3}$	$19.36 \pm 7.22\times10^{3}$
Q_{edl}	$s^n\ \Omega^{-1}\ cm^{-2}$	$0.81 \pm 0.43\times10^{-6}$	$0.94 \pm 0.07\times10^{-6}$	$2.37 \pm 1.08\times10^{-6}$
n		1.00 ± 0.11	0.99 ± 0.02	1.00 ± 1.48
R_{ct}	$\Omega\ cm^2$	$21.84 \pm 11.40\times10^{5}$	$12.30 \pm 0.27\times10^{5}$	$71.60 \pm 6.29\times10^{4}$

The anodic areas of the specimens, anodized for 48 min suffer uniform corrosion and the current density is distributed equally on the entire aluminum matrix, probably due to the initial galvanic corrosion stage. On the other hand, strong localized corrosion occurs for the samples anodized for 12 min, after only 504/672 hours of exposure. This fact shows that the durability of the samples anodized for 48 min exceeds 2,520 hours, whereas the other samples (anodized for 12 min) have already failed. All the polarization curves, recorded at the sample exposure termination, were submitted to further analysis and the obtained results for 12 and 48 min of anodization are summarized in Table 6.

Table 6. *Tafel plot analysis of the polarization curves, recorded at the end of the exposure period*

	Cathodic						Anodic					
	E_{corr} / V *vs.* Ag/AgCl			R_p / kΩ cm^2			E_{corr} / V *vs.* Ag/AgCl			R_p / kΩ cm^2		
12 min	1S12	2S12	3S12	1S12	2S12	3S12	1S12	2S12	3S12	1S12	2S12	3S12
504 h	-0.673	-0.637	-	32.0	62.0	-	-0.568	-0.655	-	16.4	42.0	-
6,672 h	-	-	-0.641	-	-	17.8	-	-	-0.699	-	-	1610.0
48 min	1S48	2S48	3S48	1S48	2S48	3S48	1S48	2S48	3S48	1S48	2S48	3S48
2,520 h	-0.623	-0.656	-0.627	142.0	460.0	38.0	-0.624	-0.627	-0.538	134.0	1380.0	960.0

In both cases of the CeOPL coated samples anodized for 12 and 48 min, the R_p values are by entire orders of magnitude higher than those of the reference samples, registered after 168 hours of exposure (Tables 4 and 6). Furthermore, the values of the samples anodized for 48 min are similar or slightly higher than those of the treated for only 12 min. The R_p values of the anodized specimens do not vary remarkably for the entire exposition period. Besides, this trend is in

concordance with the EIS data fitting (Tables 3 and 5). All these facts indicate that both sets of anodized specimens possess residual barrier ability even after extended exposure periods. This conclusion was additionally confirmed by the morphological observations, which show weaker corrosion impact of the preliminary anodized samples.

Scanning Electron Microscopy and EDX-chemical analysis - The CeOPL coated AA2024-T3 specimens after 12, 24 and 48 min of anodization were submitted to systematic SEM observations before (Fig. 7) and after (Fig. 8) the corrosion tests, described in the previous sections.

The comparison among the positions in Fig. 7 reveal clear differences among the CeOPL layers, deposited after different anodization durations. Although the CeOPL layers were deposited, following the same procedure, these possess rather distinguishable morphologies, predetermined by the AAO underlayer formation process duration. Obviously (positions (a) and (b)), the AAO formed for only 12 min is disrupted over the alloys' intermetallic particles locations. That is the reason for the occurrence of brighter coarse particles in the locations of the coating disruptions. For comparison, such intermetallics were not observed in the other cases (24 and 48 min). Another distinguishable feature observed in the case of 48 min of anodization (positions (c) and (f)) is the occurrence of net of cracks throughout the entire AAO/CeOPL layer surface.

This coating cracking is an indirect indication for a probably greater CeOPL layer thickness, achieved after 48 min of anodization. Besides, the cracks are not deep enough to cross the AAO underlayer, because these AAO/CeOPL conjunctions have shown remarkable durability, as was already commented. The concavities on the metallic surface observed for all the samples are result of the preliminary sample treatment procedures, as is discussed in previous works [31 - 33].

Similar systematic SEM observations have been done on the already corroded specimens. (i.e. CeOPL coatings after 0, 12, 24, and 48 min of anodization and subsequent corrosion tests for 168, 504, 1008 and 2520 hours of exposure). The obtained SEM images are shown in Fig. 8.

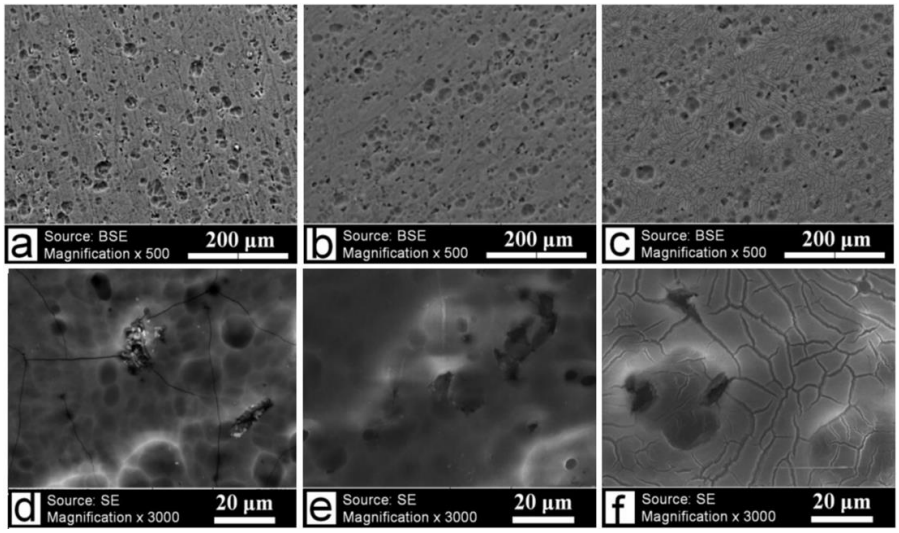

Figure 7. *Low (a, b, c) and high (d, e, f) resolution SEM images of the investigated specimens after 12 (a, d), 24 (b, e) and 48 (c, d) minutes of exposure*

The SEM images in Fig. 8 clearly demonstrate the lack of corrosion pits on the sample, anodized for 48 min, whereas in all the other cases occurrence of such pits was observed. Consequently, the AAO/CeOPL combined layers coatings, formed at the largest anodization duration possess durability superior to 2,520 hours. In addition, these samples did not show any remarkable differences before and after the corrosion tests (Fig. 7 and 8). This fact is additional evidence for the superior sample durability.

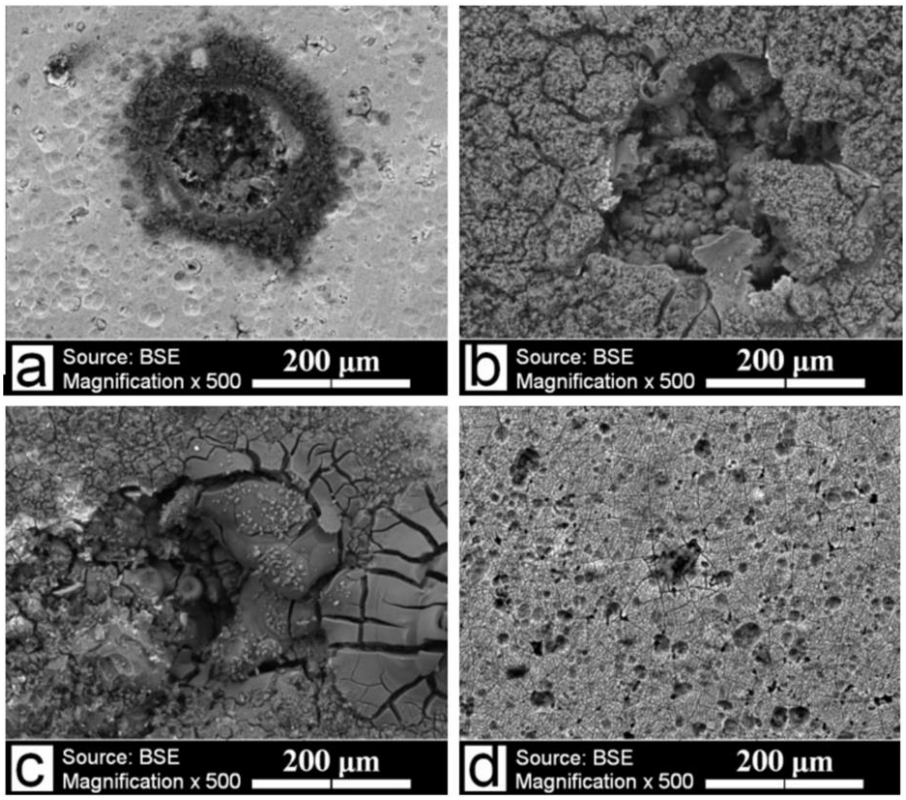

Figure 8. *Low resolution SEM images of CeOPL coatings deposited after: (a) – 0, (b) – 12, (c) – 24 and (d) – 48 minutes of anodization*

The SEM observations were followed by EDX chemical analyses, in order to illustrate the coating chemical compositions, the elements distribution regularity, and the AAO/CeOPL coverage rate before the corrosion test procedures (Fig. 9 and 10).

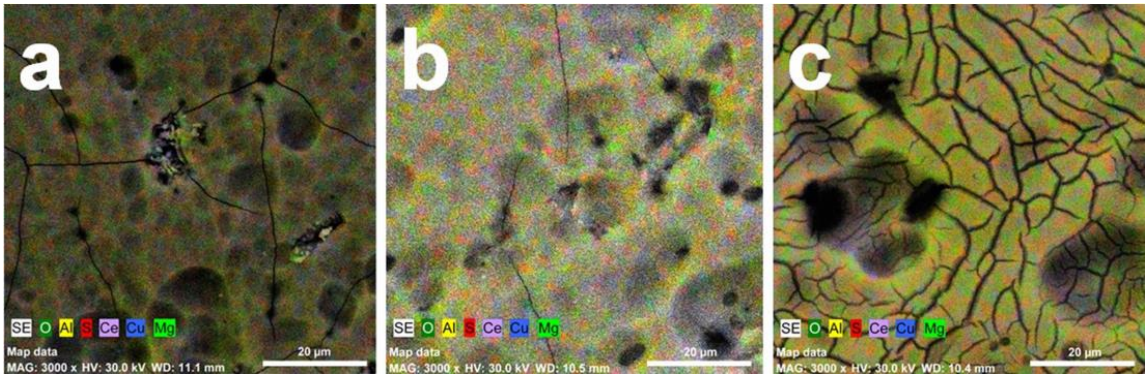

Figure 9. *EDX map analyses of CeOPL coated AA2024-T3 samples, after (a) - 12, (b) – 24 and (c) – 48 minutes of anodization*

The EDX map analyses reveal uniform element distribution, indicating uniform coverage of the metallic surface by the AAO and the further CeOPL layers. The basic alloy (Al, Cu and Mg), AAO (Al, S and O) and CeOPL (Ce and O) elements were selected for observation.

The EDX images clearly reveal Mg re-deposition and sulfur entrapment in the AAO/ CeOPL layer composition. Unlike the results from previous works [8] the CeOPL layers deposited on the already anodized AA2024-T3 samples cover completely the metallic surface possessing dense structure and uniform element distribution (Fig. 10).

The SEM cross-sectional observations (Fig. 11) reveal gradual increase of the oxide layer thickness from 8 to 18 µm, within increasing of the anodization process duration from 12 to 48 min, respectively.

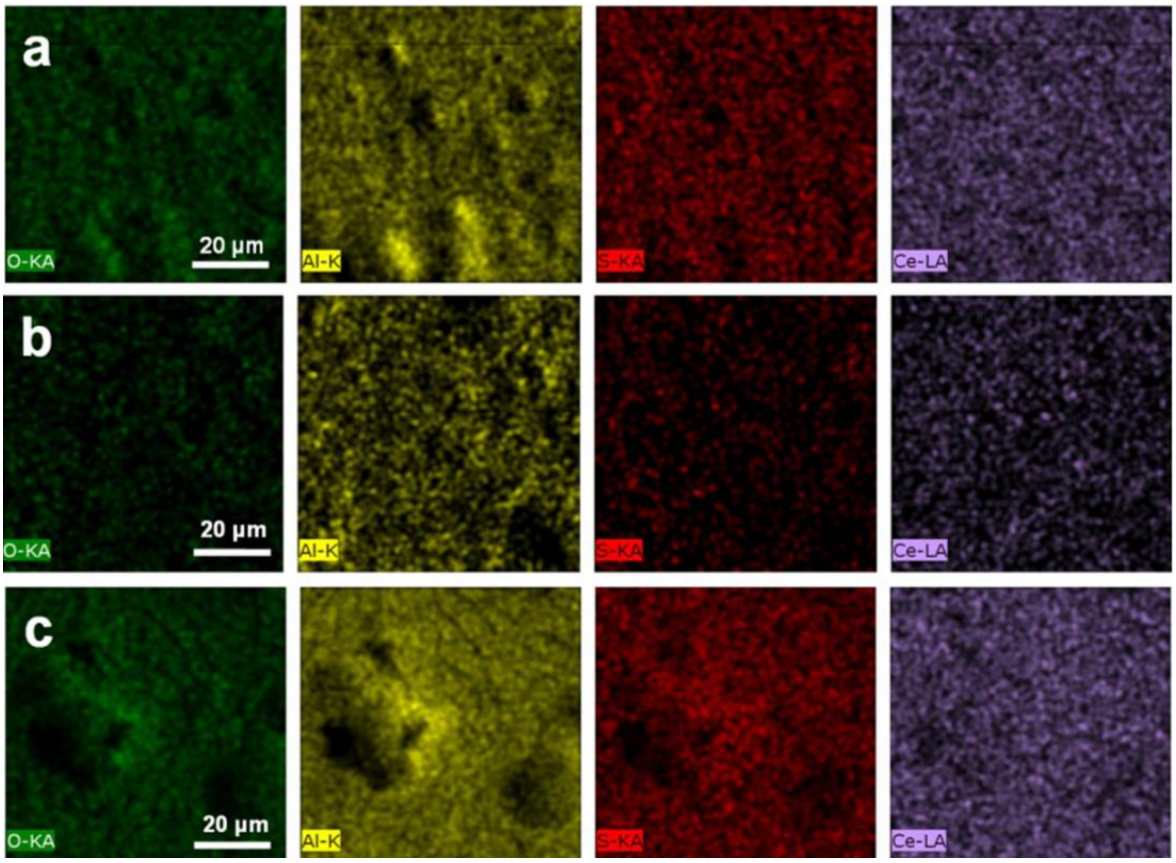

Figure 10. *Element distribution of CeOPL coated AA2024-T3 samples,* after (a) – 12, (b) – 24 and (c) – 48 minutes of anodization

The correlation between the anodization process duration and the resulting AAO/ CeOPL layer thickness reveals an AAO thickness growth rate of about 600 nm min^{-1}. An interesting trend was established when the coating thickness and durability (Section 3.1) were compared.

For instance, the mathematical ratio between the durability test data (504 h) and the film thicknesses (7.5 µm) of the AAO/CeOPL obtained after 12 min of anodization results in 70 h $µm^{-1}$. For the thickest film (18.8 µm), obtained after 48 min of anodization with 2,520 h of durability this relation has 134 h $µm^{-1}$. This difference leads to the assumption that the anodization procedure proceeds with simultaneous film densification.

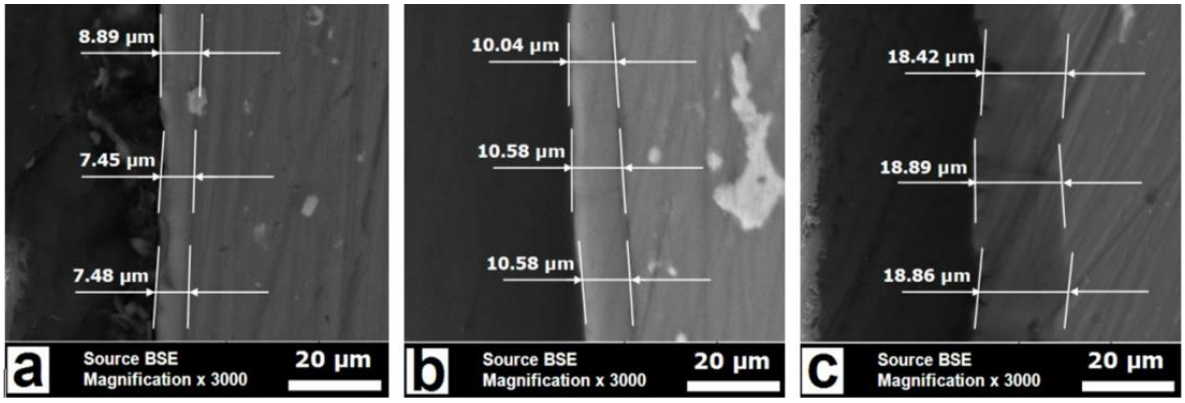

Figure 11. *Cross-sectional SEM images of AAO/CeOPL double layered coatings deposited after: (a) – 12, (b) – 24 and (c) – 48 minutes of anodization*

Another interesting point is the element distribution inside the AAO/CeOPL film. The EDX map analyses reveal relatively equal cerium- and sulfur distributions across the investigated films (Fig. 12).

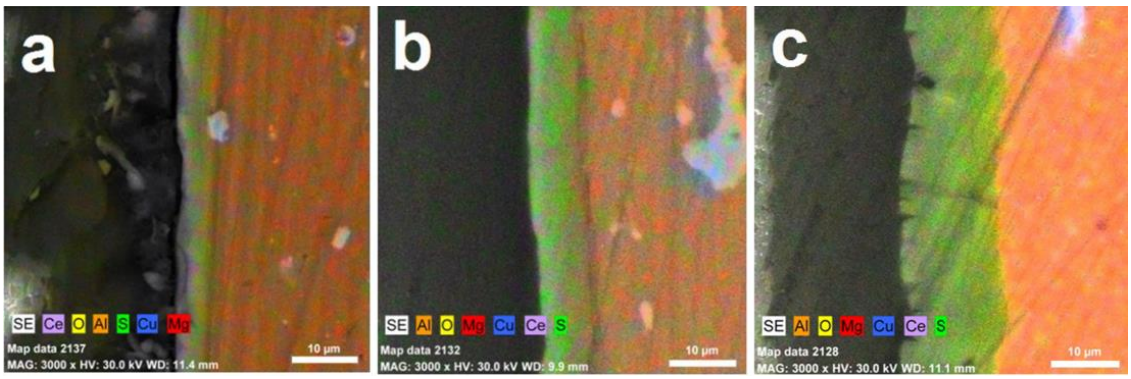

Figure 12. *Cross-sectional EDX maps of AAO/CeOPL double layered coatings deposited after: (a) – 12, (b) – 24 and (c) – 48 minutes of anodization*

NSS-test procedures - The excellent performance of the AAO/CeOPL combined coating primers obtained by 48 min (18.8 µm) of anodization was undoubtedly confirmed by the NSS test procedures, because no corrosion pits were not registered after entire 168 hours of spraying with relatively concentrated NaCl solution.

Conclusions

The possibility for combination of Anodized Alumina Oxide (AAO) and Cerium Oxide Primer Layer (CeOPL) for elaboration of efficient protective coatings for AA2024-T3 aircraft alloy was proposed. The correlation between the anodization process duration (the resulting film thickness, respectively) and protective capabilities was evaluated by systematical characterization procedures. These procedures included electrochemical measurements (EIS, LVA), combined with morphological observations (SEM) and chemical element distribution (EDX). The protective properties of all investigated coatings were evaluated by extended exposure (up to 2,520 hours) to a 3.5 % NaCl model corrosive medium and regular electrochemical measurements. Additional cross-sectional SEM and EDX observations were performed in order to determine the AAO/ CeOPL film thickness (related to the anodization duration).

The obtained results regarding significant AAO/CeOPL layer durability were confirmed by standard neutral salt spray (NSS) test. The combination among these characterization methods has enabled to create complementary image for the coating properties and their performance. In addition, the correlations between the applied deposition procedures and the resulting AAO/CeOPL coating layers were determined.

The measurement results have shown that the AAO/CeOPL conjunctions possess remarkable corrosion protective capabilities, unlike the reference CeOPL monolayers. The EIS spectra of the AAO/CeOPL conjunctions registered after 168 hours of exposure reveal much higher resistance values, compared to the referent CeOPL. Furthermore, the EIS spectra fitting required equivalent circuit for combined AAO/CeOPL layers, different from those for CeOPL reference coatings. This fact has revealed completely different performance in the model corrosive medium for both kinds of coatings. These conclusions from the EIS spectra analysis were confirmed by the respective polarization curves. The R_p values of the AAO/CeOPL layers were by entire orders of magnitude higher than those of the CeOPL references. The layers' durability increases progressively with the anodization duration. The specimens anodized for 12 minutes have resisted only about 600 hours, whereas 48 min of anodization has led to more than 2,520 hours of exposure until pitting appearance. The further data analysis, based on the film thickness determination has led to the inference that the coating durability increases progressively with the thickness growth (the ratio between the coating durability (600 to 2,520 hours) versus the film thickness (from 7.5 to 18.5 µm).

The cross-sectional EDX map analyses have undoubtedly evinced the uniform distribution of the AAO/CeOPL combined layer components (O, Al, S and Ce).

The NSS test procedures have undoubtedly confirmed the excellent performance of the thickest AAO/CeOPL combined coatings (with 18.5 µm, obtained by 48 min of anodization).

Acknowledgements: *The authors are grateful for the funding of this research to the Bulgarian National Scientific Research Fund, under contract NFNI: ДМ-19/6 - 2017.*

References

[1] W. J. Stepniowski, M. Moneta, K. Karczewski, M. Michalska-Domanska, T. Czujko, J.M.C. Mol, J. G. Buijnsters, *J. Electroanal. Chem.* **809** (2018) 59-66.
[2] S. Kozhukharov, C. Girginov, I. Avramova, M. Machkova, *Mater. Chem. Phys.* **180** (2016) 301-313.
[3] K. A. Yasakau, M. L. Zheludkevich, S. V. Lamaka, M. G. S, Ferreira, *J. Phys. Chem. B* **110** (2006) 5515-5528,
[4] G. Brunner, N. Birbilis, K. D. Ralston, S. Virtanen, *Corros. Sci*. **57** (2012) 209-214.
[5] K. D. Ralston, D. Fabijanic, N. Birbilis, *Electrochim. Acta* **56** (2011) 1729-1736.
[6] E. Kus, Z. Lee, S. Nutt, F. Mansfeld, *Corrosion* **62** (2006) 152-161.
[7] E. Sikora, X. J. Wei, B. A. Shaw, *Corrosion* **60** (2006) 387-398.
[8] S. Kozhukharov, M. Milanes, C. Girginov, M. Machkova, *Mater. Corros.* ***67*** (2016) 710-720.
[9] T. C. Tsai, T. H. Chuang, *Mater. Sci. Eng.* **A 225** (1997) 135-144.
[10] A. E. Hughes, C. MacRae, N. Wilson, A. Torpy, H. T. Muster, A. M. Glenn, *Surf. Interface Anal.* **42** (2010) 334-338.
[11] J. van den Brand, W. G. Sloof, H. Terryn, J.H.W.de Wit, *Surf. Interface Anal.* **36** (2004) 81-88.
[12] E. Koroleva, G. Thompson, G Hollrigl, M Bloeck, *Corros. Sci.* **41** (1999) 1475-1495.
[13] S. S. Golru, M. M. Attar, B. Ramezanzadeh, *Appl. Surf. Sci.* **354** (2015) 360-368.
[14] S. Kozhukharov, Ch. Girginov, I. Avramova, M. Machkova, *Mater. Chem. Phys.* **180** (2016) 301-313.
[15] T. G. Harvey, *Corros. Eng. Sci. Technol.* **48** (2013) 248-269.
[16] M.J. O'Keefe, S. Geng, S. Joshi, *Metalfinishing*, **105** (2007) 25-28.
[17] V. Matolŕın, M. Cabala, V. Chŕab, I. Matolıŕnovaŕ, K. Prince, M. Skoda, F. Sutara, T. Skaŕla, K. Veltruskŕa, *Surf. Interface Anal.* **40** (2008) 225-230.
[18] M. Škoda, M. Cabala, V. Cháb, K.C. Prince, L. Sedláček, T. Skála, F. Šutara, V. Matolín, *Appl. Surf. Sci.* **254** (2008) 4375-4379.
[19] I. Avramova, S. Suzer, D. Guergova, D. Stoychev, P. Stefanov, *Thin Solid Films* **536** (2013) 63-67.
[20] Y. Liu, J. Huang, J. B. Claypool, M. J. O'Keefe, *J. Electrochem. Soc.* **163** (2016) C198-C204.
[21] N. V. Skorodumova, S. I. Simak, B. I. Lundqvist, I. A. Abrikosov, B. Johansson, *Phys. Rev. Lett*. **89** (2002) 166601-166605.
[22] S. Kozhukharov, V. Kozhukharov, M. Schem, M. Wittmar, M. Veith, *Prog. Org. Coat.* **73** (2012) 95-103
[23] E. A. Matter, S. Kozhukharov, M. Machkova, V. Kozhukharov, *Corros. Sci.* **62** (2012) 22-33.
[24] E. A. Matter, S. Kozhukharov, M. Machkova, V. Kozhukharov, *Mater. Corros.* **64** (2013) 408-414
[25] M. Machkova, E.A. Matter. S. Kozhukharov, V. Kozhukharov, *Corros. Sci.* **69** (2013) 396-405.
[26] A. J. Aldykiewicz, A. J. Davenport, H. S. Isaacs, *J. Electrochem. Soc.* **143** (1996) 147-154.
[27] Ch. Girginov, S. Kozhukharov, M. Milanes, M. Machkova, *Mater. Chem. Phys.* **198** (2017) 137-144.
[28] M. A. Arenas, J. J. de Damborenea, *Rev. Metal.* **Extra Vol.** (2005) 433-437. (In Spanish)
[29] A. Conde, M.A. Arenas, A. de Frutos, J. de Damborenea, *Electrochim. Acta* **53** (2008) 7760-7768.
[30] M. Bethencourt, F. J. Botana, J. J. Calvino, M. Marcos, M. A. Rodriguez-Chacon, *Corros. Sci.* **40** (1998) 1803–1819
[31] E. A. Matter, S. Kozhukharov, M. Machkova, V. Kozhukharov *J. Chem. Technol. Metall.* **50** (2015) 52-64.
[32] E. A. Matter, S. V. Kozhukharov, M. S. Machkova, *Bul. Chem. Commun*. **43**(1) (2011) 23-30.
[33] E. Matter, S. Kozhukharov, *Ann. proceeds. Univ. Rousse* (Bulgaria), **49** (2010) 14-19, acces via: http://conf.uni-ruse.bg/bg/docs/cp10/9.1/9.1-2.pdf

J. Electrochem. Sci. Eng. **8(2)** (2018) 129-139; DOI: http://dx.doi.org/10.5599/jese.469

Open Access : : ISSN 1847-9286

www.jESE-online.org

Original scientific paper

Internal resistance and temperature change during over-discharge of lead-acid battery

Balázs Broda✉, György Inzelt

Institute of Chemistry, Laboratory of Electrochemistry and Electroanalytical Chemistry, Eötvös Loránd University, Pázmány P. s. 1/A, H-1117 Budapest, Hungary

Corresponding authorsE-mail: ✉balazsbroda@gmail.com

Received: October 26, 2017; Revised: January 29, 2018; Accepted: January 29, 2018

Abstract

In recent decades, more and more electronic systems (start-stop, drive-by-wire, brake-by-wire) have been developed in the automotive industry therefore reliable power sources are necessary. It is essential to understand thoroughly the detailed behaviour of the battery to increase its efficiency, stability and monitorability which is the most popular field nowadays. Over-discharge plays an important role in aging because it increases the probability of initiation of grid corrosion, sulfation and loss of active mass. In this work, the effects of over-discharge of lead-acid battery have been investigated via internal resistance increase and temperature change separately for both the negative and the positive electrode. Most of the measurements were carried out in a prepared test cell (which contained a negative and a positive plate, an $Ag|Ag_2SO_4$ reference electrode, a shunt for measuring current accurately) connected to a dummy battery and an electronic load.

Keywords

Energy storage; Deep discharge; Aging; Battery sensor

Introduction

Despite of the fact that the lead-acid battery is a 150-year-old system, its over-discharge characteristic is a less investigated area. During this process, different reactions can occur which lead to the aging of the battery (for example sulfation, loss of active mass or loss of water) [1-4]. In the 21st century, lead-acid batteries are still used in most of cars for starting the gasoline or diesel engine and for the operation of the electronic system (drive-by-wire, brake-by wire, start-stop systems) too. In this case, reliable and well-monitorable power sources are necessary. For this purpose, better understanding of over-discharge is still necessary.

At the end of the 20th century, Garche *et al.* [5] estimated the basic reactions during over-discharge. The cell voltage, the potential of the positive and the negative electrode, the intensity

of gas evolution and the density of sulfuric acid at the top of the cell were measured. It was stated that the basic reaction during discharge proceeded to a lesser extent and was replaced by other reactions (for example increased gas evolution). In case of positive electrode, the capacity loss is mainly caused by mechanical stress, because of different molar volumes of the reactants ($V_{\text{lead-dioxide}}$:$V_{\text{lead-sulfate}}$:V_{lead}=1.4:2.7:1.0). In case of negative electrode, the main reason of the aging is the irreversible oxidation of the expanders.

This capacity loss was investigated by Blank et al. [6] setting depth of discharge (DOD) from 100 % to 130 %. It was stated that significant part of the initial capacity was lost because of over-discharge just after a few cycles. The amount of decreasing was closely related to DOD level, at higher DOD, the loss of capacity was also larger. It is also stated by the authors that the area of deep discharge has so far been mostly neglected in published research apart from fundamental material investigations [7].

In this paper, we present the effects of over-discharge on the internal resistance of the negative and the positive electrode and the whole cell and on the temperature of the electrolyte at different places of the cell (in the vicinity of the negative and the positive electrode and in the bulk solution).

Experimental

Two types of batteries were investigated. We used a Furukawa HiDash battery (type: flooded, voltage: 12 V, capacity: 48 Ah) for the internal resistance measurements and a test cell which contains a negative and a positive plate of a dry Unibat battery (type: flooded, voltage: 12 V, capacity: 9 Ah) and 650 ml 37 m/m% sulfuric acid for temperature experiment.

Internal resistance measurement

The potential of the positive and the negative electrode against $Ag|Ag_2SO_4$ reference electrode and another cell voltage were measured by using labjack data acquisition device. We apply 4.8 A current [which is the *C*/10 current for a battery which capacity (*C*) is 48 Ah] until it reduced to the 10 % of its initial value. During this procedure, we measured the impedance of the battery every 10 minutes at 1 kHz excitation frequency which is good approximation to the battery's internal resistance (Figure 1). The 1 kHz-resistance $R_{1\text{kHz}}$ is defined as the real part of the battery impedance at 1 kHz frequency. This is a practical definition, since it is quickly measurable with an active excitation device. The standard handheld battery testers usually measure this value. [8]

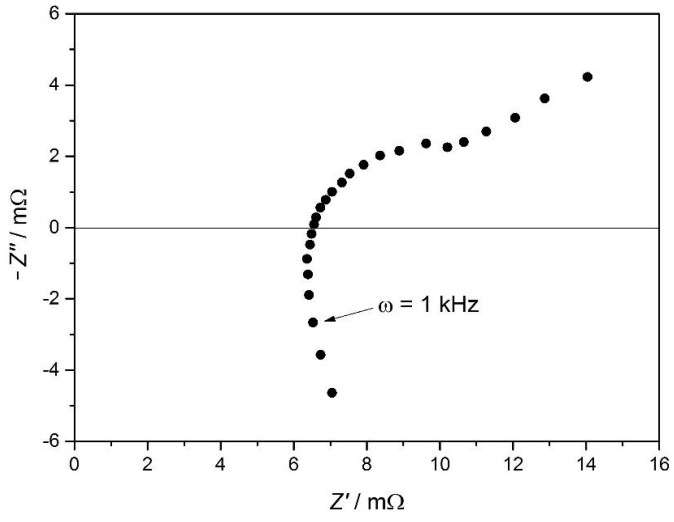

Figure 1. *Measured impedance spectrum of the examined cell during discharge (Nyquist plot)*

Temperature experiment

An Ag|Ag_2SO_4|saturated aqueous K_2SO_4 solution (0.69 V *vs.* SHE) reference electrode and J-type thermocouples were used. The schematic representation of the experimental system is shown in Figure 2.

Four thermocouples were used to measure the temperature at different places in the cell, their positions are presented in Figure 3. We used a heat chamber to hold the external temperature constant (25 °C).

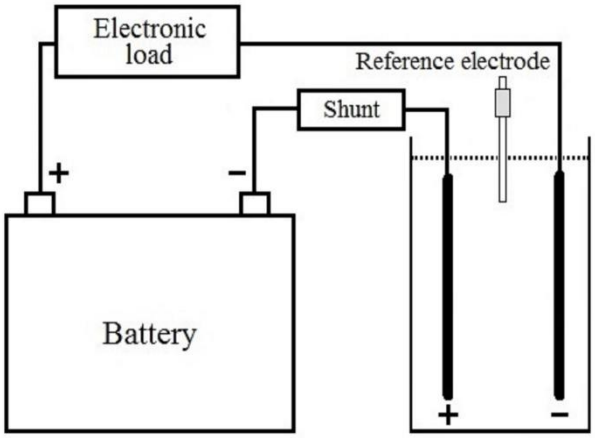

***Figure 2**. Experimental system*

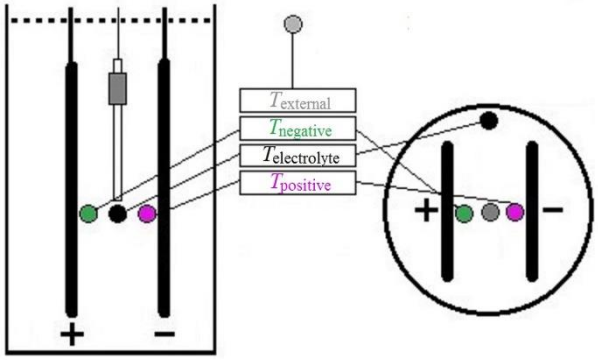

***Figure 3**. Temperature measurement*

The procedure is summarized in Table 1.

***Table 1.** Procedure of the measurements*

	Operation *(details)*		**Circumstances** (T = 25 °C)
1	**Preparation**	*Cell preparation*	–
2		*Immersion*	U_{cell} > 2.1 V
3	**Pretreatment**	*Charge*	I_{lim} = 0.16 A; U_{lim} = 2.4 V; t = 2 h
4		*Discharge*	I = 0.16 A; t = 1 h
5		*Charge*	I_{lim} = 0.16 A; U_{lim} = 2.4 V; t = 2 h
6		*Discharge*	I = 0.16 A; t = 1 h
7		*Charge*	I_{lim} = 0.16 A; U_{lim} = 2.4 V; t = 2 h
8		*Discharge*	I = 0.16 A; t = 1 h
9	**Achieving full charge**	*Charge*	I_{lim} = 0.16 A; U_{lim} = 2.4 V; I < 0.016 A
10		*Delay*	–
11	**Capacity measurement**	*Discharge*	I = 0.16 A; U_{cell} < 1.75 V
12	***„Over-discharge"***	*Discharge*	I = 0.16 A; $t = t_{capacity\ measurement} \cdot (x\text{-}1)$
13	***Setting DOD* (100·*x*%)**	*Delay*	t = 1 h
14	**„Recharge"**	*Charge*	I_{lim} = 0.16 A; U_{lim} = 2.4 V; t = 16 h
15		*Delay*	–

In step 12, *x* can be 1.0, 1.1 and 1.2, which means that the DOD level is 100 %, 110 % and 120 %. The duration of step 12 is the product of the duration of step 11 ($t_{\text{capacity measurement}}$) and *x*-1.

Results and discussion

Internal resistance measurement

Negative electrode

In Figure 4 (regarding to the end of step 11, step 12 and 13 and the beginning of step 14 of Table 1), it can be seen that during the over-discharge (between ca. 3-8 h) the negative electrode's internal resistance changed to nearly 100 times of its initial 2-3 mΩ value when a large change in the potential of the negative electrode occurred. When the potential has become practically constant (there is only a small decrease because of the uncertainty of potential measurement), the electrode's internal resistance has begun to decrease at a similar rate to the previous one and reached about 2 times of its initial value. The internal resistance of the negative electrode hasn't changed until the end of discharge, but when the current has become zero (between ca. 8-9 h) a significant increase could be observed. This process lasted until the charging has been started. During recharging (between ca. 9-16 h), the internal resistance highly decreased and returned to its initial value after several minutes.

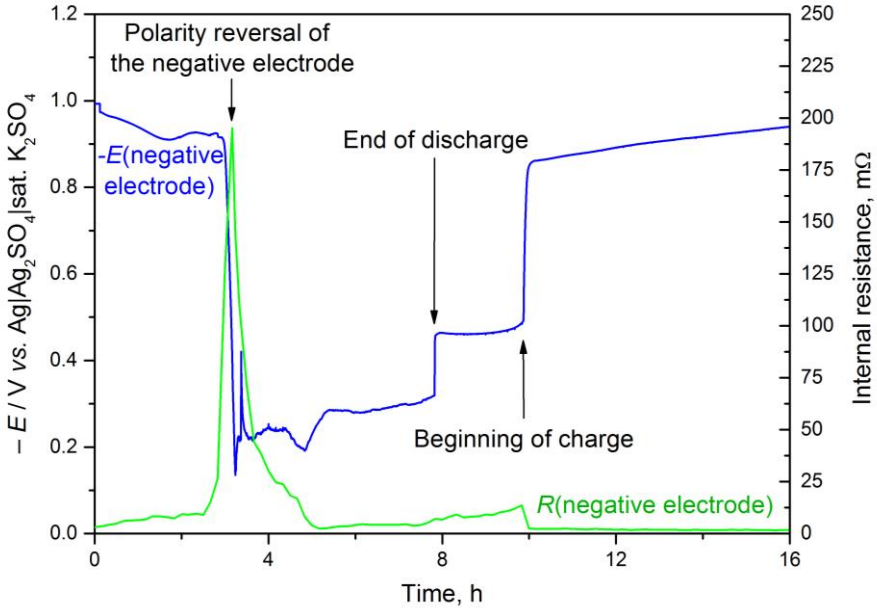

***Figure 4**. Change of the potential of the negative electrode (multiplied by minus 1) and internal resistance during a discharge-charge cycle*

During discharge (between ca. 0-3 h), porous metallic lead is converted to lead sulfate at the negative electrode (Reaction 1).

$$Pb + HSO_4^- \rightarrow PbSO_4 + H^+ + 2\ e^- \qquad \text{(Reaction 1)}$$

The specific volume of $PbSO_4$ is approximately 3 times higher than the specific volume of Pb and its conductivity is lower by orders of magnitude [9]. Thus, the porosity decreases during this process as well as the pores become clogged (so the diffusion coefficient of the different species in the electrolyte decreases). At the same time, sulfuric acid reacts with lead, that's why its concentration becomes smaller and the amount of acid required for the reaction isn't available on the surface of the active material. As the result of these two processes, the potential of the negative electrode and the internal resistance highly increase.

The Nernst equation provides an approximate calculation of the potential of the negative electrode. Although the system is not in equilibrium during discharge, this relationship can be used to interpret the direction of the processes.

$$E_{PbSO_4/Pb} = E^o{}_{PbSO_4/Pb} + \frac{RT}{2F}\ln\frac{a_{PbSO_4}a_{H^+}}{a_{Pb}a_{HSO_4^-}} \quad (1)$$

Where $E_{PbSO_4/Pb}$ is the potential of the negative electrode, $E^o{}_{PbSO_4/Pb}$ is the standard electrode potential of the $PbSO_4$/Pb system (-0.356 V *vs.* SHE), R is the gas constant, T is the temperature of the system, F is the Faraday constant and a_{PbSO_4}, a_{Pb}, a_{H^+}, $a_{HSO_4^-}$ are the activities of the given species.

Based on Equation 1, if the lead ion or the sulfate ion activity changes on the electrochemically active surface of the electrode, the potential of the negative electrode will change too. The concentration (also the activity) of the sulfuric acid decreases continuously during discharge, due to this, the potential also gradually increases. The reason of the high change at the end of discharge is the decrease of both species' activity.

At more positive potential, other reactions can take place. The most significant reactions are the following:

$PbSO_4 + 2\ H_2O \rightarrow PbO_2 + HSO_4^- + 3\ H^+ + 2\ e^-$ (Reaction 2)

$2\ H_2O \rightarrow 4\ H^+ + O_2 + 4\ e^-$ (Reaction 3)

In Reaction 2 lead sulfate with high resistance and specific volume is converted to lead dioxide. Due to this reaction, the electrode's internal resistance is decreased and the average size of the pores is increased. In Reaction 3 (which is significant when the polarity reversal of the negative electrode takes place), oxygen gas evolves, which phenomena was observed by Garche *et al.* [5]. On the one hand, these gas bubbles mix the electrolyte, so the inhomogeneities can be eliminated. On the other hand, a non-conductive layer of gas is formed on the active surface resulting in increased internal resistance. If all electrochemically active lead reacted due to the Reaction 1, the potential changes (even the potential of the positive electrode can be reached) and the Reactions 2 and 3 take place. Based on this, the over-discharge of the negative electrode is very similar to the charge/over-charge of the positive electrode. During this process, the internal resistance of the electrode doesn't change significantly until the end of over-discharge.

After over-discharge, the system is left alone for 2 hours and synproportionation can occur (Reaction 4), in which the remaining lead content of the active mass reacts with lead-dioxide generated during over-discharge (Reaction 2).

$Pb + PbO_2 + 2\ HSO_4^- + 2\ H^+ \rightarrow 2\ PbSO_4 + 2\ H_2O$ (Reaction 4)

In this case, the concentration of sulfuric acid decreases, lead and lead dioxide with lower resistance and specific volume converted to lead sulfate with high resistance and specific volume. Based on these phenomena, pores can become clogged and the internal resistance can significantly increase.

During the recharge, both lead sulfate and lead dioxide can be converted into lead with better conductivity and lower specific volume. Although the transformation of the whole amount of lead sulfate requires a long time, the internal resistance significantly decreases during ca. 10 minutes. This phenomenon can be explained with the opening of pores and higher sulfuric acid concentration inside them which resulted in low resistivity connectors to the grid. Several hours later, the internal resistance reaches to its initial value.

Positive electrode

The observed phenomena during discharge of the positive electrode (Figure 5) were similar to the previously mentioned ones. In Figure 5, the end of step 11, step 12 and 13 and the beginning of step 14 of Table 1 are shown. The internal resistance increased continuously as the cell lost its capacity ("normal" discharge between ca. 0-3 h) and when high decrease of the potential occurred, it increased by approximately two orders of magnitude compared to the initial value. During over-discharge (between ca. 3-8 h), it approached its initial value, and after that, when discharge was over (between ca. 8-9 h), we experienced some increase again. After starting the recharge (between ca. 9-16 h), it reached its initial value in about half an hour.

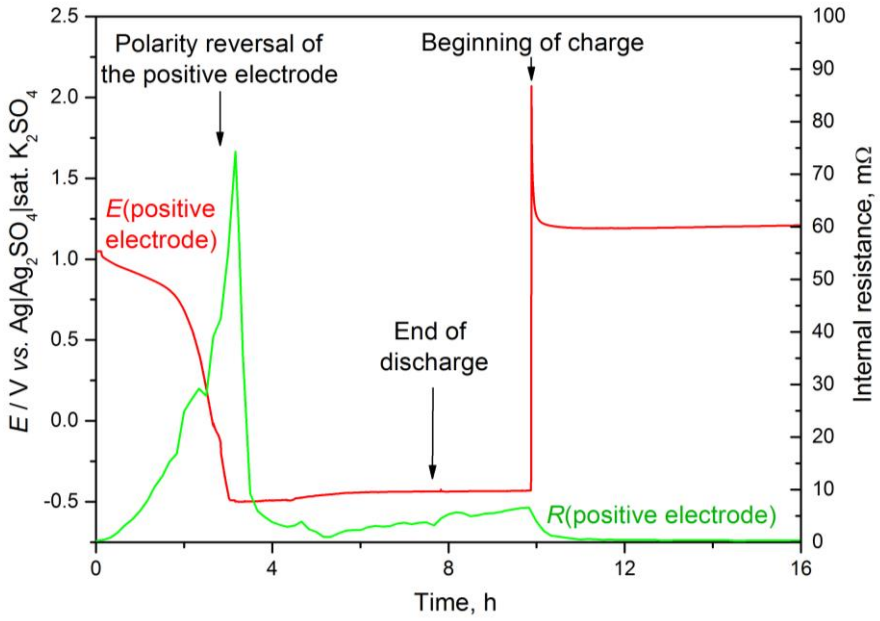

Figure 5. *Change of positive electrode's potential and internal resistance during a discharge-charge cycle*

In this case, the potential of the positive electrode can also be estimated from the Nernst equation.

$$E_{PbO_2/PbSO_4} = E^o{}_{PbO_2/PbSO_4} + \frac{RT}{2F}\ln\frac{a_{PbO_2}a_{H^+}^3 a_{HSO_4^-}}{a_{PbSO_4}a_{H_2O}^2} \quad (2)$$

where $E_{PbO_2/PbSO_4}$ is the potential of the positive electrode, $E^o{}_{PbO_2/PbSO_4}$ is the standard electrode potential of the $PbO_2/PbSO_4$ system (+1.685 V vs. SHE), R is the gas constant, T is the temperature of the system, F is the Faraday constant and a_{PbO_2}, a_{PbSO_4}, a_{H_2O}, a_{H^+}, $a_{HSO_4^-}$ are the activities of the given species.

This case is a little bit more complex than the case of negative electrode. Although, the reason of the potential's monotone decrease is the sulfuric acid consumption, but the fall of potential can be caused by several processes: the decrease of activity of lead-dioxide (in extreme case when the battery is "fully" discharged, almost the whole surface of the active material is covered by lead-sulfate, so the activity of the lead-dioxide must be less than one) or sulfuric acid or the increase of activity of water next to the electrochemically active surface (the activity of the water in such a concentrated electrolyte is less than one [10]). It can be stated that the potential doesn't change dramatically when the over-discharge of the positive electrode completed. There may be two

different explanations: Reaction 4 isn't significant during over-discharge at all or it becomes significantly important before the process is over. It can be distinguished betweem the two possibilities by analyzing the results of the resistance measurement.

Looking at the change in internal resistance of the positive electrode, the phenomenon is similar to the case of the negative electrode. The initial increase is caused by clogged pores and high resistivity lead sulfate. The interpretation of sudden decrease in the potential is practically the same as mentioned before, but there is an important difference in the further part of over-discharge, the internal resistance begins to increase before the process is over. Based on this, it is concluded that the Reaction 4 becomes significant before over-discharge is over.

Cell

In Figure 6, the voltage of a whole cell is shown (regarding to the end of step 11, step 12 and 13 and the beginning of step 14 of Table 1). Besides the previously mentioned phenomena, interesting behavior could be observed after the cell reversal (between ca. 5-8 h) and after the over-discharge was finished (between ca. 8-10 h). The internal resistance of the cell didn't decrease during the over-discharge period as much as shown in the previous sections. This phenomenon can be justified by the worse structural properties of the active material. If the pores inside the electrodes and the electrochemically active surface of them are smaller, the effects of the same processes can be much larger as it can be seen until the beginning of recharge (between ca. 5-10 h). After the end of discharge, the internal resistance increased just as in the case of the negative and positive electrode, but the rate was much higher than it can be expected, which also refers to the poor structural properties of the electrode. But after this region, the resistance decreased (between ca. 8-10 h). If we consider that the impedance measurement has an impact on the system, it can be explained by the discharge current which was applied in every 10 minutes for a short time resulting in a decrease of internal resistance (the pulsating curve also suggests this phenomenon).

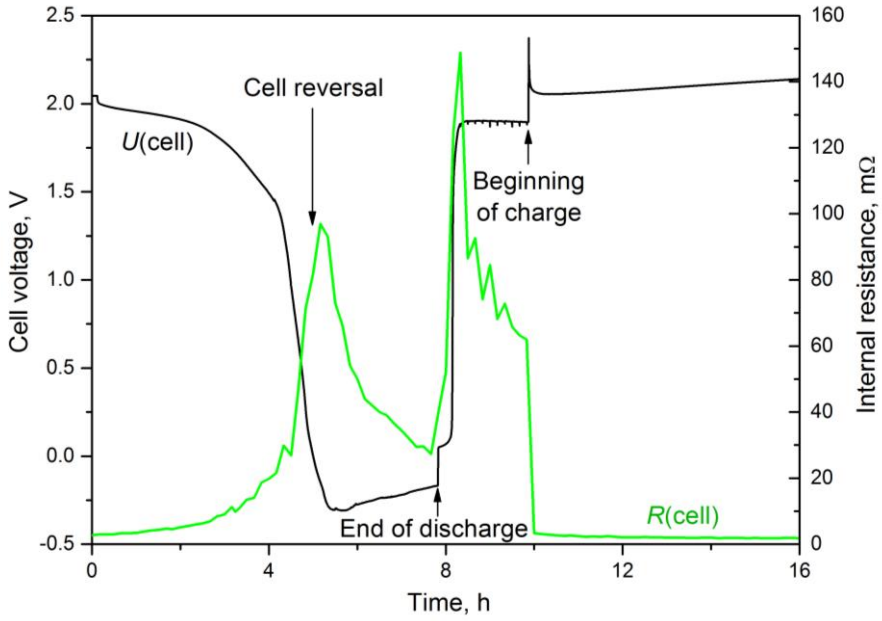

Figure 6. *Change of cell's voltage and internal resistance during a discharge-charge cycle*

Based on this, it can be said that during the measurements when current flowed through the system, this phenomenon hadn't caused an error, because the current was applied for a short time. It was only significant when neither discharge nor charge was executed. In the experiments

shown in Figure 4 and Figure 5, this phenomenon was negligible because the system was not in a labile state contrast to the measurement shown in Figure 6.

Temperature measurement

Over-discharge

In Figure 7, it is shown that during the negative electrode polarity reversal, at first the value of that thermocouple changes ($T_{negative}$) which is located in the direct vicinity of the negative electrode and the other ones follow later. The temperature near the positive electrode ($T_{positive}$) and in the bulk electrolyte ($T_{electrolyte}$) starts to increase 15 minutes after the negative electrode polarity reversal. According to our expectations, $T_{negative}$ changed the biggest (0.4 °C), $T_{positive}$ and $T_{electrolyte}$ increased by 0.3 °C. The phenomenon regarding to the positive electrode polarity reversal was essentially the same.

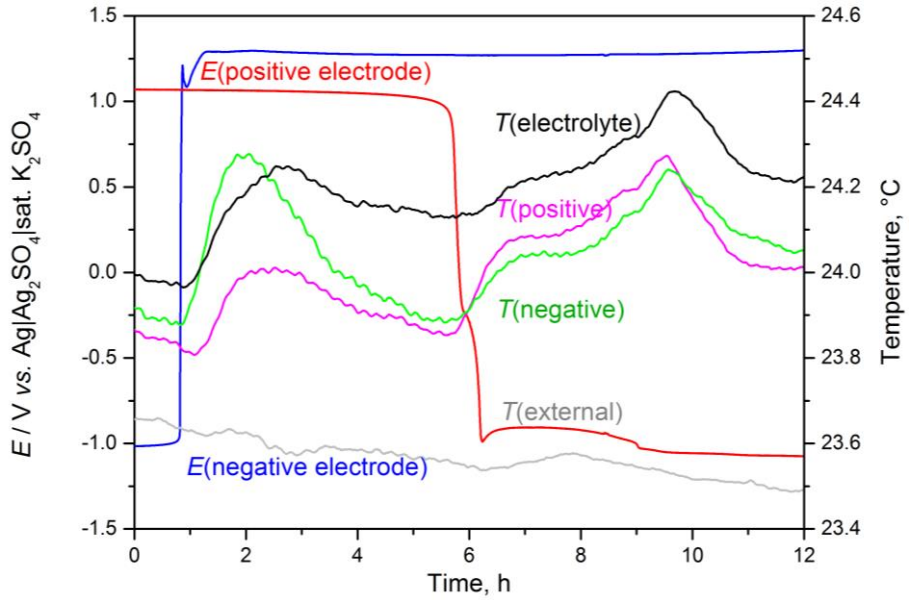

Figure 7. *Temperature change due to over-discharge (potential of negative and positive electrode, temperature in the vicinity of the negative and the positive electrode, in the electrolyte and in the heat chamber)*

These changes may not seem very significant at first sight, but if they are converted for the original cell, the effects are much higher. In Table 2, the most important differences between the test cell and the original cell are summarized.

Table 2. *Parameters of the cells.*

	Test cell	**Original cell**
Amount of electrolyte, ml	650	75
Number of negative electrodes	1	5
Number of positive electrodes	1	4
Measured capacity, Ah	ca. 3	ca. 8

Based on the measured values by the thermocouple placed in the electrolyte, it can be assumed that the temperature of the whole cell has increased by more than 0.3 °C. During over-discharge if the same processes take place, the original cell generates about 3 times as much heat

as the test cell based on the capacity differences. The cell voltages are practically the same in these cases, but approximately 3 times higher charge goes through the original cell than the test cell. The generated heat can be calculated as the product of voltage and charge based on Equation 5.

We need to estimate the heat capacity of the electrodes. For this calculation, we used the following molar heat capacity values: 2 J/(mol·°C) for lead, 103 J/(mol·°C) for lead sulfate and 61 J/(mol·°C) for lead dioxide. The weight of the negative electrode is approximately 40 g of which the lead grid is 12 g and the active mass is the remaining 30 g (we suppose that it contains mostly lead at the beginning of the measurement). The positive electrode's weight is approximately 50 g, of which the lead grid is 12 g and the active mass is 38 g (we suppose that it is mostly lead dioxide at the beginning). By the time the cell was discharged, approximately 3 Ah of charge was passed through it. According to the Faraday law, it is possible to calculate how much active mass was converted during discharge procedure (Table 3, Table 4).

Table 3. *Transformation of active material and sulfuric acid in the test cell during discharge*

	Negative electrode		**Positive electrode**		**Electrolyte**	
Compound	Lead	Lead sulfate	Lead dioxide	Lead sulfate	Sulfuric acid	Water
m_{beg} / g	28	0	38	0	308	524
m_{trans} / g	-12	+17	-13	+17	-11	+2
m_{end} /g	16	17	25	17	297	526

We used the following data for the calculation: ρ (37 m/m% sulfuric acid) = 1.28 g/cm^3; M(Pb) = 207.2 g/mol; M($PbSO_4$) = 303.3 g/mol; M(PbO_2) = 239.2 g/mol; M(H_2SO_4) = 98.1 g/mol; M(H_2O) = 18.0 g/mol; F = 96500 C/mol.

Table 4*. Transformation of active material and sulfuric acid in the original cell during discharge.*

	Negative electrode		**Positive electrode**		**Electrolyte**	
Compound	Lead	Lead sulfate	Lead dioxide	Compound	Lead	Lead sulfate
m_{beg} / g	140	0	152	0	36	61
m_{trans} / g	-31	+45	-36	+45	-29	+5
m_{end} /g	109	45	116	45	6	66

Based on the measured capacity of the original cell, it is stated that approximately 8 Ah charges could pass through the cell until reaching the fully discharged state. At that time, the mass fraction of the sulfuric acid in the test cell was 36 m/m% [heat capacity=2.9 J/(g·°C)] and it was 9 m/m% in the original cell [heat capacity=3.9 J/g·°C). [11]

Based on Table 3, Table 4 and the above-mentioned data, the heat capacity of the cells can be calculated (active mass+grid+electrolyte): $C_{test\ cell}$=2410 J/°C, $C_{original\ cell}$=374 J/°C.

We can make a calculation to estimate the generated heat ($Q_{test\ cell}$) in the test cell:

$$Q_{test\ cell} = C_{test\ cell}\ \Delta T_{test\ cell} = 2410\ \text{J} / {}^{o}\text{C} \times 0.3{}^{o}\text{C} = 723\ \text{J} \approx Q_{original\ cell}/3 \quad (3)$$

where $\Delta T_{test\ cell}$ is the temperature change during the negative electrode polarity reversal, $Q_{orginal\ cell}$ is the generated heat in the original cell due to the previously mentioned effect.

Based on this, we can roughly calculate how many degrees of Celsius the original cell will warm with the same current density and process:

$$\Delta T_{\text{original cell}} = Q_{\text{original cell}} \approx \frac{732\ \text{J} \times 3}{364\ \frac{\text{J}}{^{\circ}\text{C}}} = 5.8\ ^{\circ}\text{C} \tag{4}$$

The temperature in the original cell would increase by about 6 °C due to the electrode polarity reversal. However, it is important to note that this will be the average value in the whole cell, so inside the electrode, the temperature can rise significantly higher which has a very significant role in aging processes. [12]

It can be assumed that not the different reactions cause the temperature rise, because the system cools down later and it approaches its initial state in the vicinity of the electrodes' surface, although the reactions don't change significantly at that time. However, the high resistance increase can cause this phenomenon.

The initial resistance of the cell was 0.02 Ω, the current (I) during the whole procedure was 0.16 A, the duration (t) of the temperature rise (also the duration of the high resistance increasing) was approximately 1 hour. The generated heat (Q) can be estimated from Equation 5.

$$Q = P\,t = U_{\text{cell}}\,I\,t = R\,I^2\,t \tag{5}$$

where P is the electrical power, U_{cell} is the cell voltage and R is the resultant resistance.

We can calculate the resultant resistance from Equation 6.

$$R = \frac{Q}{I^2 t} = \frac{723\ \text{J}}{(0.16\ \text{A})^2 \times 3600\ s} \approx 8\ \Omega \tag{6}$$

Although the calculation contains many approximations and estimates, it shows that the resultant resistance, as in the previous section, increased by more than two orders of magnitude during over-discharge process (when the potential of the electrode and the temperature greatly changed at the same time).

"Recharge"

The recharging of an over-discharged cell is shown in Figure 8.

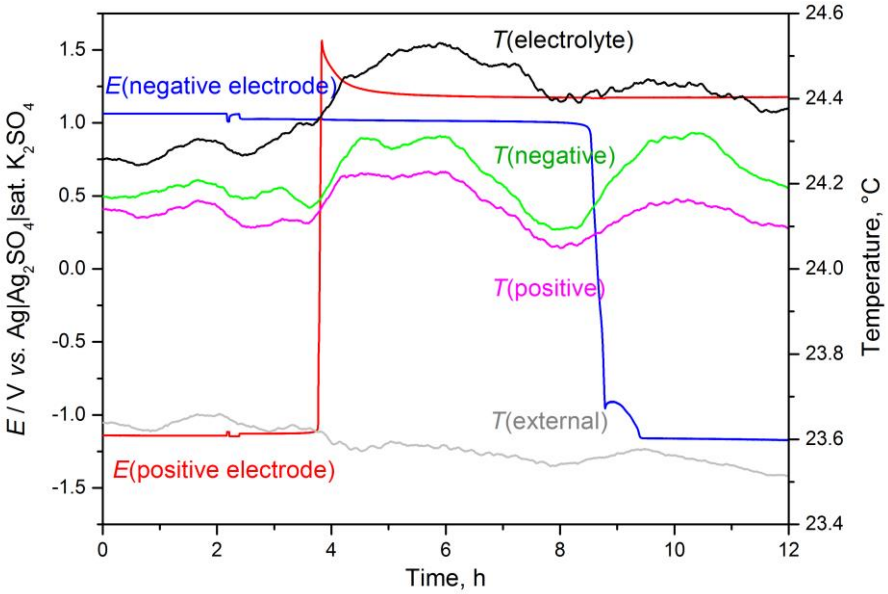

Figure 8. *Temperature change due to "recharge" (potential of negative and positive electrode, temperature in the vicinity of the negative and the positive electrode, in the electrolyte and in the heat chamber)*

During the recharging, temperature rise was also experienced which was similar to the previously described one (during over-discharge) and the heat capacity of the cell was practically the same. Based on these results, we can state that the internal resistance of the examined cell increased by several orders of magnitude compared to its initial value during the recharging.

Conclusions

By investigating a lead-acid test cell, it was proved that the internal resistance highly increased during the cell reversal. This process and the increasing gas evolution caused significant temperature to rise inside the electrode undergoing the reversal and consequently in the whole cell. This is a very reproducible phenomenon which has a serious influence on aging specifically on the loss of capacity because there is high temperature increase and gas flow at the same time.

Acknowledgements: Financial and spiritual support from the Bolyai Collage is gratefully acknowledged.

References

[1] P. Ruetschi, *Journal of Power Sources* **127** (2004) 33-44.
[2] T. B. Reddy, *Linden's Handbook of Batteries*, Elsevir, New York, USA, 2002
[3] J. Garche, E. Karden, P. T. Moseley, D. A. J. Rand, *Lead-Acid Batteries for Future Automobiles*, Elsevir, Amsterdam, Netherland, 2017
[4] L. G. Mallison, *Ageing Studies and Lifetime Extension of Materials,* Springer, Oxford, United Kingdom, 2001
[5] J. Garche, A. Jossen, H. Doring, *Journal of Power Sources* **67** (1997) 201-212.
[6] T. Blank, J. Badeda, J. Kowal, D. U. Sauer, IEEE Conference, Deep discharge behavior of lead-acid batteries and modeling of stationary battery energy storage systems, Scottsdale, USA, 2012, p. 1-4.
[7] D. Pavlov, *Lead-Acid Batteries: Science and Technology*, Elsevier, Oxford, United Kingdom, 2011, p. 178.
[8] G. Bárány, *Lead-acid battery state detection for automotive electrical energy management*, PhD dissertation, Budapest University of Technology and Economics, 2015, p. 70-81.
[9] H. Bode, *Lead-Acid-Batteries*, John Wiley & Sons, New York, United States, 1977
[10] K. R. Bullock, *Journal of Power Sources* **35** (1991) 197-223.
[11] J. E. Kunzler, W. F. Giauque, *Journal of the American Chemical Society* **74** (1952) 3472-3476.
[12] A. Jossen, H. Karl, G. Lehner, F. Hummel, 9. Symposium Photovoltaische Solarenergie, Betriebserfahrungen mit unterschiedliechen Bleibatterien, Bad Staffelstein, Germany, 1994, p. 271.

J. Electrochem. Sci. Eng. **8(2)** (2018) 141-149; DOI: http://dx.doi.org/10.5599/jese.502

Open Access : : ISSN 1847-9286

www.jESE-online.org

Original scientific paper

Investigating products of titanium dissolution in the presence of fluoride ions with dual dynamic voltammetry

Noémi Kovács✉, Laura Sziráki, Soma Vesztergom, Győző G. Láng

Department of Physical Chemistry, Laboratory of Electrochemistry and Electroanalytical Chemistry, Eötvös Loránd University, Pázmány Péter sétány 1/A, 1117 Budapest, Hungary

Corresponding author's E-mail: ✉kovacsnoemi@chem.elte.hu; Tel.: +36-1-372-2500/1527

Received: January 15, 2018; Accepted: February 21, 2018

Abstract

Products of titanium dissolution in the active state are investigated in fluoride containing 1 M H_2SO_4 solutions. The novel method of dual dynamic voltammetry, applied to Ti disk/Pt ring rotating ring–disk electrodes, is utilized for the simultaneous detection of different dissolution products. Potential regions where certain products (primarily, Ti^{III} and H_2) are formed are identified by a 3D electrochemical map constructed based on the ring–disk electrode measurements. Besides dissolution in the form of Ti^{III} species and hydrogen evolution, the formation and prompt oxidation of Ti^{II} can also be presumed under the applied conditions.

Keywords

Rotating ring–disk electrodes; electrochemical map; cyclic voltammetry; dental implant materials; corrosion

Introduction

Due to its extensive application, the electrochemical stability of titanium has been the subject of investigations for more than fifty years [1–14]. The pure metal itself, and also some of its alloys are widely applied as materials of dental implants and braces. Thus, being aware of the possible dissolution processes of Ti, which can take place in acidic media and in the presence of fluoride ions, is paramount. Assessing the possible corrosion products of Ti alloys that contain materials with toxic forms is of special importance. Accordingly, the literature of the topic is abundant and continuously expanding [1–22].

In this paper we demonstrate the applicability of a novel experimental method, dual dynamic voltammetry [23–25], for the detection of different dissolution products of titanium. The described technique is applicable to the vast majority of generator-collector systems, in what follows, however, we will concentrate on rotating ring–disk electrodes (RRDEs).

In conventional RRDE experiments the potential (or the current) of at least one of the two working electrodes is held constant. It was recently shown, however, that independent and dynamic potential programs can also be applied simultaneously to the disk and the ring electrodes [23–26]. By means of dual dynamic potential control, the sensitivity of the RRDE system can significantly be increased, and this control technique also enables the application of several new methods such as the so-called fast ring scanning technique [24]. In this paper, we apply this latter technique for investigating the dissolution of titanium in the presence of fluoride ions.

Since dual dynamic potential control is not feasible by the application of commercially available bipotentiostats, our measurements were carried out by using our self-built measurement station [27]. As it is going to be shown, fast ring scanning experiments on an RRDE can be applied very effectively for studying the dissolution of titanium in acidic media, and in particular, for the detection of different dissolution products.

In order to demonstrate the advantages of this technique, we chose a relatively simple target system: a Ti disk/Pt ring RRDE immersed into 1 M H_2SO_4 solutions, containing F^- in different concentrations.

Titanium dissolution under similar conditions has been investigated before. Titanium exhibits excellent corrosion resistance in sulfuric acid solutions, due to the easy formation of a highly protective oxide film (mainly TiO_2). This oxide coating possesses a rather high chemical stability [2,3], preventing the corrosion of the metal. However, researchers seem to agree that fluoride ions, when present in the electrolyte solution, can dissolve the protective oxide layer, exposing fresh titanium surface, and thus destroying the corrosion resistance [2,4,5].

Titanium dissolution in sulfuric acid solutions can also be observed in the absence of F^- [6–10], although at a considerably lower rate compared to F^- containing media. Dissolution in the oxidation state of Ti^{IV} is likely to occur at positive potentials, in the passive potential region [7], while the formation of Ti^{III} and Ti^{II} species is supposed to occur at negative potentials, in the active potential region [6]. Ti^{II} can, however, easily be oxidized in aqueous media, resulting the formation of elemental hydrogen [6,11]. At negative potentials, evolution of hydrogen occurs in two parallel paths: one path involves the usual solvated proton and the other involves the adsorbed surface species $(TiOH)^+_{ads}$, followed by a fast recombination reaction [11].

The aim of this work is to present how dual dynamic voltammetry, when used with RRDEs, can allow the simultaneous detection of the different dissolution products of titanium, formed in a broad potential range.

Experimental

Measurements were carried out with rotating ring–disk electrodes in standard four electrode cells. In all cases, the cell contained a separate reference compartment being connected to the cell by a Luggin capillary positioned close to the RRDE surface. A NaCl saturated calomel electrode (SSCE) was applied as reference and two glassy carbon rods surrounding the RRDE tip were connected and used as a counter electrode. During the presented measurements the electrode tip was rotated at 500 min^{-1}.

The 1 M H_2SO_4 solution was made by dilution of concentrated sulfuric acid (Merck) with Milli-Q water. The fluoride ion containing solutions were prepared by addition of a 1 M H_2SO_4 + + 1 M NaF solution, made from solid NaF (VWR Chemicals). Solutions were purged by and maintained under argon. Measurements were carried out in a water-jacketed glass cell at 37 °C.

All the glass parts used in the experiments were previously immersed in piranha solution for several hours, rinsed with de-ionized water, and cleaned by steam.

RRDE measurements were controlled by our self-built electrochemical workstation [27]. This system relies on the state-of-the-art data acquisition devices of National Instruments (PCI-4461 and PCI-6014 boards) that can be used in combination with analogue bi-potentiostats. For the measurements presented here, the measuring system was equipped with a PINE Model AFCBP1 bi-potentiostat. The measuring system was controlled by a software written in the National Instruments LabVIEW development environment.

During the experiments we used the following three configurations.

Configuration A

For the experiments concerning titanium dissolution in 1 M H_2SO_4 solution and in 1 M H_2SO_4 + + 20 mM NaF solution we applied a PINE AFE6R1PtPK ChangeDisk rotating ring–disk electrode tip containing a fixed platinum ring (A_r = 0.1100 cm^2) with a PINE AFED050P040 titanium disk (99.999 %, A_d = 0.1963 cm^2). The gap size between the ring and the disk was 0.75 mm. Collection efficiency calculated from the geometric parameters is 25.6 % [28]. Prior to measurements, the disk and the ring were separately polished by SiC paper and diamond suspension (finest grain size: 1 µm). After polishing, the electrode surfaces were rinsed with pure ethanol and Milli-Q water.

Before recording the presented experiments, the titanium disk was left for 1 hour in 1 M H_2SO_4 solution at OCP. Meanwhile, high speed cyclic voltammograms were recorded at the ring in order to clean its surface and to gain a stable baseline CV shape for the collection experiments [24]. After the addition of the fluoride ion containing solution the disk was etched for 15 min at OCP, then we started to polarize it slowly towards positive potentials. The presented data are results of the first cathodic sweep.

Configuration B

Experiments investigating hydrogen evolution and oxidation on platinum were carried out with the PINE AFE6R1PtPK ChangeDisk rotating ring–disk electrode tip containing a fixed platinum ring mentioned above. Instead of the titanium disk insert, in this case we used a PINE AFED050P040 platinum (99.99 %) disk. The geometric parameters and the applied polishing procedure were the same as in case of configuration A. Before recording the presented data, high speed cyclic voltammograms were simultaneously recorded at the disk and ring electrodes for 1 hour.

Configuration C

For the experiments demonstrating the effect of fluoride ion concentration in the electrolyte we used a fixed “home-made” titanium (99.99 %) disk/platinum ring rotating ring–disk electrode (A_d = 0.1963 cm^2, A_r = 0.2134 cm^2) with collection efficiency of 37.5 %, calculated from the geometric parameters [28]. The gap size between the ring and the disk was 0.60 mm. Prior to measurements, the surface of the electrode tip was renewed by lathe machining followed by rinsing with ethanol and Milli-Q water.

The presented measurement series were carried out with step by step additions of fluoride ion containing solution. After every addition step, the titanium disk was etched for 15 min at OCP before starting the individual measurements.

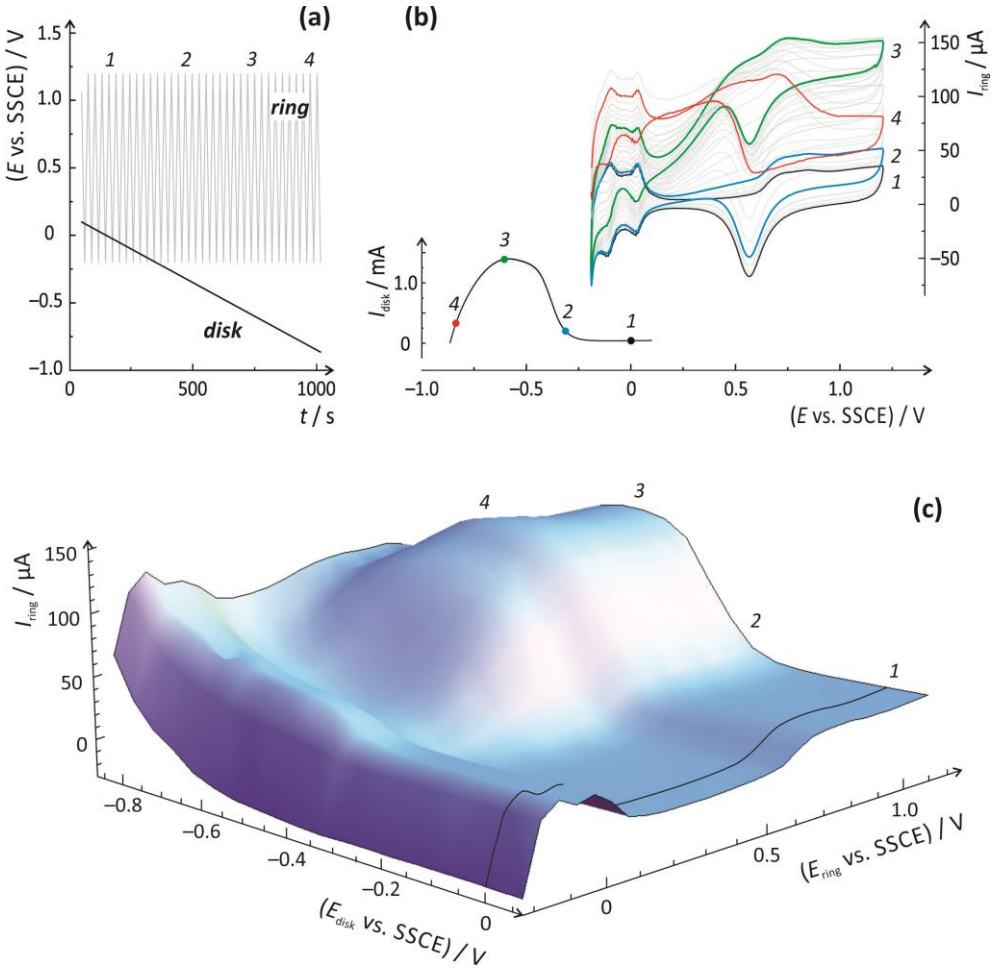

Figure 1. (a) *Control signal of the disk and the ring electrodes. While the disk electrode was polarized at a relatively slow sweep rate (1 mV/s), high speed cyclic voltammograms were recorded at the ring electrode (sweep rate: 100 mV/s).* ***(b)*** *Measured current at the disk and the ring electrodes as a function of the electrode potential. The emphasized cyclic voltammograms on the ring (1–4) were recorded while the disk potential was at the marked values.* ***(c)*** *3D representation of the measured data created by bilinear interpolation (grid resolution: 50 x 50 mV). The current measured on the ring electrode during the anodic ring scans is plotted as a function of the disk and ring potentials,* E_{disk} *and* E_{ring}*.*

Results and discussion

For the investigation of titanium dissolution in the active potential region in the presence of fluoride ions, a special example of dual dynamic voltammetry, the fast ring scanning technique [24] was applied. The essence of this technique is that the disk electrode is polarized at a sufficiently low and the ring electrode at a sufficiently high scan rate. Potential and current data measured this way can be used for the creation of a 3D map that may reveal the electroactive products or intermediates formed in the electrode processes taking place on the disk electrode.

The results of the measurements with a Ti disk / Pt ring RRDE in 1 M H_2SO_4 + 20 mM NaF and the applied potential program can be seen in Figure 1. The disk electrode was polarized at 1 mV/s sweep rate from 100 mV *vs.* SSCE, towards negative potentials. At the same time, cyclic voltammograms were recorded at 100 mV/s on the ring between potential limits of –200 mV and 1200 mV *vs.* SSCE. These experiments were carried out using cell configuration A (described in the Experimental section). Due to the hydrodynamic flow created by rotation, the products formed on the disk reach the surface of the ring where the electroactive species can be detected.

When using fast ring scanning, the current yielded by the detected species is superimposed on a baseline, the cyclic voltammogram of the ring.

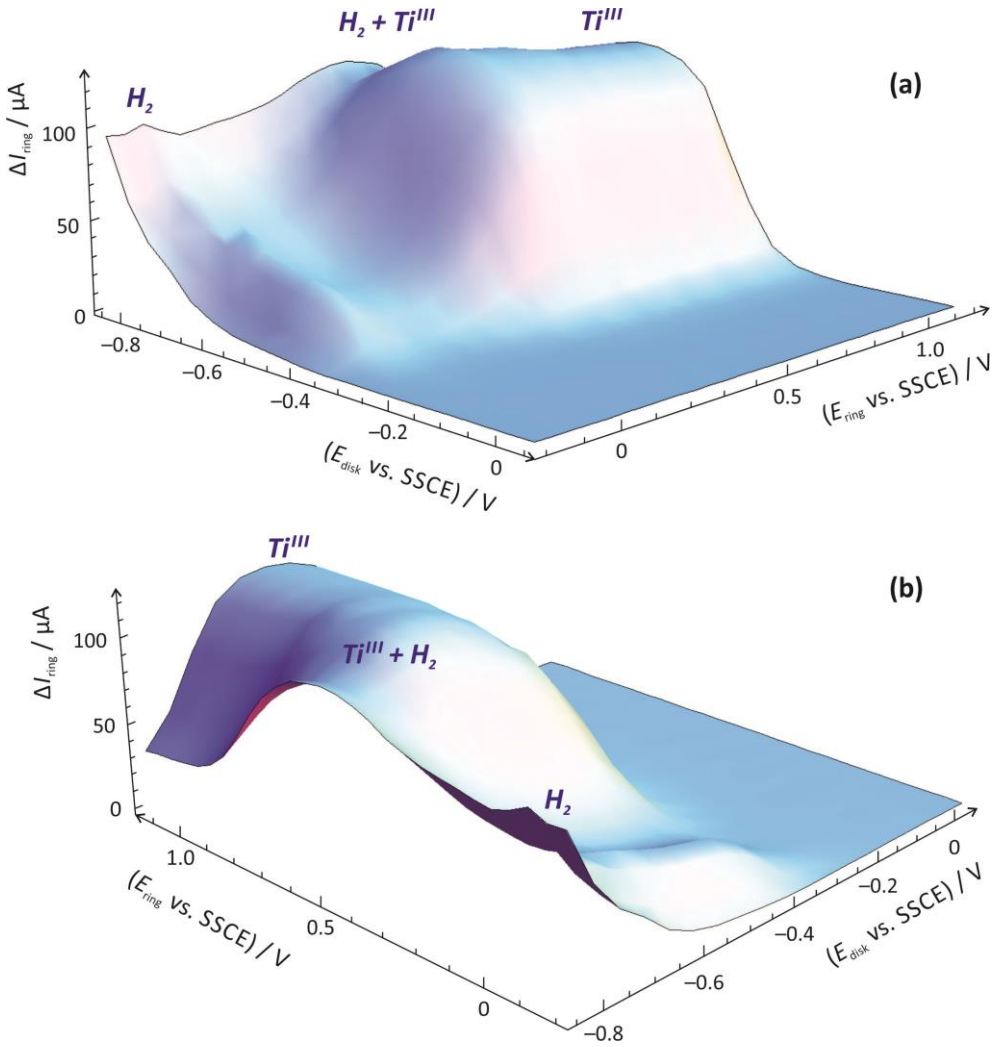

Figure 2. *Difference (*ΔI_{ring}*) of the ring current and the reference anodic scan (*$E_{ref,\ disk}$ *= 0 V* vs. *SSCE) as a function of* E_{disk} *and* E_{ring} *from two different perspectives:* ***(a)*** *and* ***(b)****.*

In Figure 1(b) it is apparent that the polarization of the disk towards negative potentials results in no significant change of the ring CVs; at least, until no current on the disk is measured (see point *1* on the disk voltammogram in Figure 1(b) and the corresponding ring CV). As the disk current starts to increase (*2*), the positive potential parts of the ring CVs start to lift and, later on (*3*), the negative potential parts also start slowly to increase. After the disk current reaches its maximum, the positive potential parts of the ring CVs tend to fall back, while the negative potential parts keep increasing. In order to show all these changes at the same time, a 3D map can be constructed (Figure 1(c)) by means of bilinear interpolation, using the measured disk potential, ring potential and ring current data. For details of the interpolation algorithm, see [29].

The ring scan marked as *1* in Figure 1(c), recorded while the disk was at about 0 V *vs.* SSCE, was chosen as reference and subtracted from the 3D map in order to obtain the "surface of changes": the changes measured in the ring currents resulted by the polarization of the disk (ΔI_{ring}) as a function of the disk and ring potentials. Figure 2 shows the electrochemical map constructed in this way from two different view-points.

For the identification of the peaks on Figure 2, similar measurements were carried out in 1 M H_2SO_4 solution with a Ti/Pt, and also with a Pt/Pt RRDE using cell configuration A and B, respectively. Figure 3 shows the results of these experiments. During the slow cathodic polarization of the platinum disk electrode in 1 M H_2SO_4, the evolution of hydrogen starts to occur at suitably negative disk potentials. The hydrogen originating from the disk can be oxidized on the ring electrode, resulting in the changes of the measured Pt CVs, as shown in Figure 3(a).

We note that similar changes in the ring CVs can be measured if we supply hydrogen from an outside source (gas bottle) to the electrolyte. At most potentials, where the platinum surface is active, the collected hydrogen causes an increase of the measured ring current. This increase seems to be independent of the electrode potential of the ring over a broad potential range. When the ring potential is high enough, however, so that the platinum surface is oxidized, the oxidation rate of hydrogen is much slower [30–32]. Thus, the positive potential parts of the ring CVs hardly lift during the experiment.

The situation is rather different in the case when a Ti disk is applied in combination with a Pt ring (1M H_2SO_4). In case of a slow, negative-going polarization, the titanium disk begins to dissolve even in a fluoride-free electrolyte, as a result of a passive-active transition. This is shown by the moderate hump in the polarization curve of Ti, shown in Figure 3(b) at point *2*. As a result, a moderate increase of current can be observed at positive ring potentials: an effect that was not present in the case of Pt, and which is due to the collection of Ti^{III} species [6]. At more negative potentials (see point *3*), hydrogen evolution and slow titanium dissolution take place simultaneously [6,9] and current signals related to hydrogen detection dominate the ring CVs.

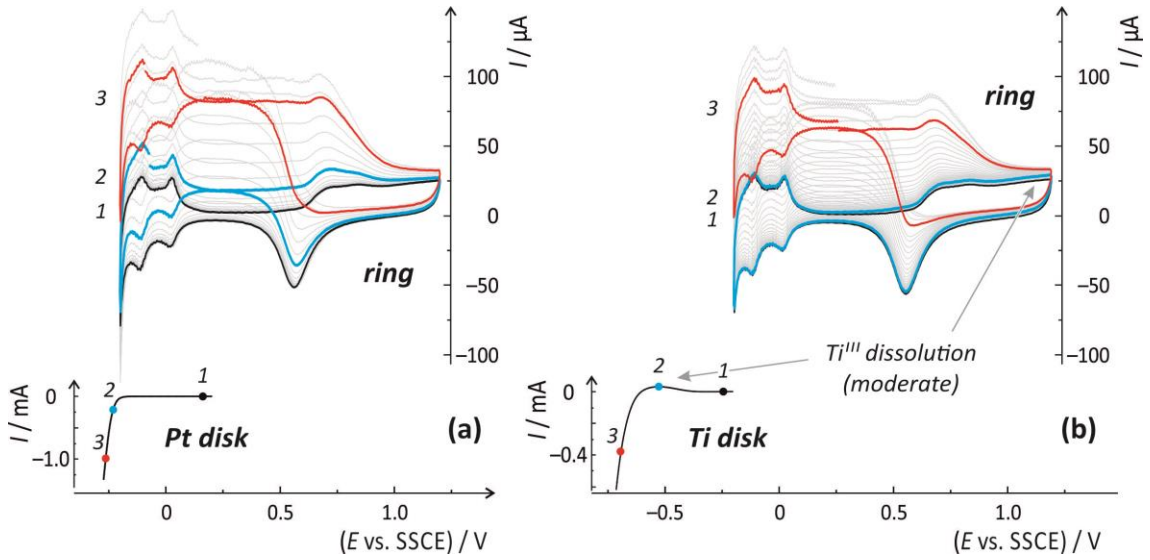

Figure 3. (a) *Hydrogen evolution resulted by a slow, negative-going scan on the platinum disk and oxidation of the produced hydrogen on the platinum ring of a Pt/Pt RRDE in 1 M H_2SO_4.* ***(b)*** *Slow, negative-going scan on the titanium disk and oxidation of the formed products and intermediates on the platinum ring of a Ti/Pt RRDE in 1 M H_2SO_4. In both cases the disk electrode was polarized towards negative potentials at 0.25 mV/s sweep rate while on the ring cyclic voltammograms were recorded between –200 mV and 1200 mV* vs. *SSCE at 100 mV/s scan rate.*

Based on the experiments presented in Figure 3, we can come to the conclusion that the lift of the positive potential parts of the platinum CVs in Figure 1(b) and 1(c) is caused mainly by the collection of Ti^{III} species formed on the disk, while the lift of the negative potential parts of the ring CVs corresponds to the oxidation of hydrogen.

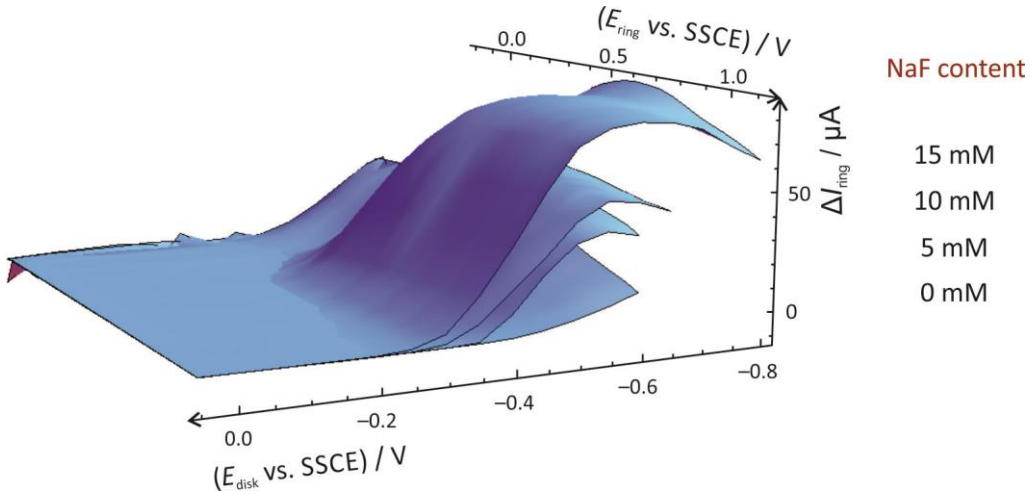

Figure 4. *Illustration of the effect of varying the fluoride ion concentration on the detectable ring current changes during fast ring scanning measurements. Measurements were taken in 1 M H_2SO_4 solutions containing NaF at different concentrations as indicated. Measurements were taken using configuration C, as described in the Experimental Section. A reference disk potential of 0 V vs. SSCE was used for creating the presented surfaces.*

Here we note that hydrogen detection on the ring electrode may either be a result of direct hydrogen formation or of Ti^{II} production on the disk. As Ti^{II} is unstable in aqueous environments, it is expected to react quickly with water and/or protons to form hydrogen and Ti^{III} [11]. Accordingly, at negative disk potentials, Ti^{III} formed as a result of Ti^{II} oxidation may contribute to the Ti^{III} collection signal.

It is interesting to note that the 3D surfaces of Figure 2 apparently exhibit three, relatively distinct features. While one of these clearly corresponds to the collection of H_2 and another to that of Ti^{III} species, the third peak-like feature —based on the results shown in Figure 3— can be attributed to the combined collection of hydrogen and Ti^{III} species.

In our interpretation, Figure 2 describes the following scheme: while at not very negative potentials, the main dissolution product is Ti^{III}, at more negative potentials, the disk generates H_2, Ti^{III} and, probably, also Ti^{II}. As Ti^{II} is very unstable in aqueous solutions, it gets oxidized resulting the formation of Ti^{III} and additional hydrogen. Note that the ring signal corresponding to Ti^{III} does not fully decay, not even at extreme cathodic disk polarization (Figure 2(b)). Thus it can be assumed that even at these very negative potentials some Ti^{III} is formed on the disk or that —more likely— the disk generates Ti^{II}, the subsequent oxidation of which results in the collection of Ti^{III} on the ring. In a narrow potential region on the ring, the collection of Ti^{III} and hydrogen co-occurs, resulting in the peak-like feature marked as "Ti^{III} + H_2" in Figure 2(b).

The qualitative interpretation of the measurements, outlined above, remains the same for fluoride concentrations between 5 and 20 mM, although the intensity of the ring current signals (the amount of dissolved species) grows in strict correlation with the fluoride concentration. This is shown by Figure 4 and can also be expected based on literature [5,14].

Summary

By using the method of dual dynamic voltammetry, applied to a Ti disk/Pt ring RRDE, products formed during the polarization of titanium in 1 M H_2SO_4 + 20 mM NaF solution in a broad potential range were simultaneously detected. In the applied fast ring scanning technique, high speed cyclic voltammograms were recorded on the ring electrode while the disk electrode was polarized slowly from the edge of the passive potential region to the active potential region. As a

result, a 3D electrochemical map of the dissolution products was constructed, giving a comprehensive illustration of potential regions where the different products are formed and where they can be converted electrochemically. Besides dissolution in the form of Ti^{III} species and hydrogen evolution, the formation and prompt oxidation of Ti^{II} can be presumed under the applied conditions.

Acknowledgements*: This work was supported by the ÚNKP-16-3 and ÚNKP-17-3 New National Excellence Program of the Ministry of Human Capacities (ELTE/8495/60(2016) and ELTE/12422/82(2017)). Financial support from the National Research, Development and Innovation Office & Hungarian Scientific Research Fund (NKFI OTKA K109036) is gratefully acknowledged. S. Vesztergom gratefully acknowledges support from grant NKFI PD-124079 from the National Research, Development and Innovation Office, Hungary.*

References

[1] M. Stern, H. Wissenberg, *Journal of The Electrochemical Society* **106** (1959) 755-759.
[2] J. J. Kelly, *Electrochimica Acta* **24** (1979) 1273-1282.
[3] D. J. Blackwood, L. M. Peter, D. E. Williams, *Electrochimica Acta* **33** (1988) 1143-1149.
[4] M. J. Mandry, G. Rosenblatt, *Journal of The Electrochemical Society* **119** (1972) 29-33.
[5] Z. B. Wang, H. X. Hu, C. B. Liu, Y. G. Zheng, *Electrochimica Acta* **135** (2014) 526-535.
[6] R. D. Armstrong, J. A. Harrison, H. R. Thirsk, R. Whitfield, *Journal of The Electrochemical Society* **117** (1970) 1003-1006.
[7] E. J. Kelly, *Journal of The Electrochemical Society: Electrochemical Science and Technology* **123** (1976) 162-170.
[8] J. A. Harrison, D. E. Williams, *Electrochimica Acta* **27** (1982) 891-895.
[9] W. B. Utomo, S. W. Donne, *Electrochimica Acta* **51** (2006) 3338-3345.
[10] D. Devilliers, M. T. Dinh, E. Mahé, D. Krulic, N. Larabi, N. Fatouros, *Journal of New Materials for Electrochemical Systems* **9** (2006) 221-232.
[11] E. J. Kelly, H. R. Bronstein, *Journal of The Electrochemical Society: Electrochemical Science and Technology* **131** (1984) 2232-2238.
[12] W. Wilhelmsen, A.P. Grande, *Electrochimica Acta* **32** (1987) 1469-1474.
[13] D.-S. Kong, *Langmuir* **24** (2008) 5324-5331.
[14] M. S. Amrutha, F. Fasmin, S. Ramanathan, *Journal of The Electrochemical Society* **164** (2017) H188-H197.
[15] D. J. Wever, A. G. Veldhuizen, J. de Vries, H. J. Busscher, D. R. A. Uges, J. R. van Horn, *Biomaterials* **19** (1998) 761-769.
[16] J. E. G. González, J. C. Mirza-Rosca, *Journal of Electroanalytical Chemistry* **471** (1999) 109-115.
[17] M. Nakagawa, S. Matsuya, K. Udoh, *Dental Materials Journal* **20** (2001) 305-314.
[18] N. Schiff, B. Grosgogeat, M. Lissac, F. Dalard, *Biomaterials* **23** (2002) 1995-2002.
[19] A. S. Mogoda, Y. H. Ahmad, W. A. Badawy, *Journal of Applied Electrochemistry* **34** (2004) 873-878.
[20] B. Lindholm-Sethson, B. I. Ardlin, *Journal of Biomedical Materials Research Part A* **86A** (2008) 149-159.
[21] V. A. Alves, R. Q. Reis, I. C. B. Santos, D. G. Souza, T. de F. Gonçalves, M. A. Pereira-da-Silva, A. Rossi, L. A. da Silva, *Corrosion Science* **51** (2009) 2473-2482 .
[22] J. C. M. Souza,S. L. Barbosa, E. A. Ariza, M. Henriques, W. Teughels, P. Ponthiaux, J.-P. Celis, L. A. Rocha, *Materials Science and Engineering C* **47** (2015) 384-393.
[23] S. Vesztergom, M. Ujvári, G. G. Láng, *Electrochemistry Communications* **13** (2011) 378-381.
[24] S. Vesztergom, M. Ujvári, G. G. Láng, *Electrochemistry Communications* **19** (2012) 1-4.
[25] N. Kovács, M. Ujvári, G. G. Láng, P. Broekmann, S. Vesztergom, *Instrumentation Science and Technology* **43** (2015) 633-648.
[26] S. Vesztergom, M. Ujvári, G. G. Láng, *Electrochimica Acta* **110** (2013) 49-55.
[27] S. Vesztergom, N. Kovács, M. Ujvári, G. G. Láng, *tm - Technisches Messen* **84** (2017) 683-696.

[28] S. Vesztergom, in *Reference Module in Chemistry, Molecular Sciences and Chemical Engineering*, Elsevier, Amsterdam, Netherlands, 2018, chapter id. 13563-2.
[29] S. Vesztergom, M. Ujvári, G.G. Láng, in *Voltammetry: Theory, Types and Applications*, Y. Saito, T. Kikuchi, Eds., Nova Science Publishers, New York, USA, 2013, p. 249.
[30] S. Schuldiner, *Journal of The Electrochemical Society* **115** (1968) 362-365.
[31] J. Bao, D. D. Macdonald, *Journal of Electroanalytical Chemistry* **600** (2007) 205-216.
[32] A. E. von Mengershausen, N. V. Almeida, M. N. Barzola, J. O. Zerbino, S. M. Esquenoni, M. G. Sustersic, *Green and Sustainable Chemistry* **4** (2014) 55-59.

J. Electrochem. Sci. Eng. **8(2)** (2018) 151-162; DOI: http://dx.doi.org/10.5599/jese.508

Open Access : : ISSN 1847-9286

www.jESE-online.org

Original scientific paper

Electrochemical behaviour of poly(3,4-ethylenedioxytiophene) modified glassy carbon electrodes after overoxidation – the influence of the substrate on the charge transfer resistance

Dora Zalka✉, Soma Vesztergom, Mária Ujvári, Győző G. Láng

Institute of Chemistry, Laboratory of Electrochemistry and Electroanalytical Chemistry, Eötvös Loránd University, Pázmány P. s. 1/A, H-1117 Budapest, Hungary

Corresponding author E-mail: ✉zalkadora@caesar.elte.hu; Tel.: +36 1 372 2500 / 1527

Received: February 12, 2018; Revised: March 22, 2018; Accepted: March 22, 2018

Abstract

*Time dependence of the electrochemical impedance of an overoxidized glassy carbon|poly(3,4-ethylenedioxytiophene) (PEDOT)|0.1 mol·dm^{-3} sulfuric acid (*aq.*) electrode has been investigated. To follow the changes occurring at the film/substrate interface after the overoxidation procedure, successive impedance measurements were carried out. Although the system is intrinsically nonstationary, the charge transfer resistance (*R_{ct}*) corresponding to different time instants could be determined by using the so-called 4-dimensional analysis method. The same post-experimental mathematiccal/analytical procedure could be used also for the estimation of the charge transfer resistance corresponding to the time instant just after overoxidation of the PEDOT film. The increase of the charge transfer resistance of the overoxidized system with respect to that of the pristine electrode suggests that during overoxidation the electrochemical activity of the film decreases and the charge transfer process at the metal/film interface becomes more hindered. After the overoxidation procedure, when the electrode potential was held in the "stability region" (at* E *= 0.4 V* vs. *SSCE in the present case) the* R_{ct} *decreased continuously with experiment time to a value somewhat higher than that of the pristine electrode. By comparing the properties of the GC|PEDOT|0.1 M* H_2SO_4 *and the Au|PEDOT|0.1 M* H_2SO_4 *electrodes a possible mechanistic explanation for the observed behavior has been proposed. This is based on the assumption that in the case of the GC|PEDOT|0.1 M* H_2SO_4 *electrode two processes may occur simultaneously during the impedance measurements: (a) reduction of the oxidized surface of the GC substrate, including the reduction of the oxygen-containing surface functionalities and (b) readsorption of the polymer chains (polymer chain ends) on the surface.*

Keywords

Non-stationary system; 4-dimensional analysis method; substrate-polymer interaction; oxidation of glassy carbon.

* This paper is dedicated to the memory of our friend and colleague Professor Zdravko Stoynov in recognition of his great contribution to electrochemistry.

Introduction

Intrinsically conducting organic polymers such as polythiophenes, polyanilines and polypyrroles have been studied intensively during the last decades. Poly(3,4-ethylenedioxythiophene) [1], often abbreviated as PEDOT, and its derivatives are relatively stable compared to other conducting polymers. The conjugated polymer backbone, consisting of alternating C-C double bonds, provides for π-orbital overlap along the molecule. PEDOT can be doped with many anions, including macromolecular polyanions such as poly(styrene sulfonate) (PSS). Previous studies have shown that PEDOT is highly insoluble in most solvents, electroactive in aqueous solutions [2-4], and exhibits a relatively high conductivity. The behavior of PEDOT in electrochemical systems is a hot topic nowadays due to its important applications in a variety of fields. Many studies have been performed recently to investigate the electrochemistry of PEDOT in more detail by using voltammetric techniques (in most cases cyclic voltammetry). It has been found in Refs. [5-9] that at sufficiently positive electrode potentials, degradation of the polymer occurs. The oxidative degradation of polypyrroles, polythiophenes is known as „overoxidation". That is, when the positive potential limit of the cyclic voltammogram (CV) is extended to the region in which the "overoxidation" of the polymer film takes place, an oxidation peak (without a corresponding reduction peak) appears in the 1st CV (with a maximum in the vicinity of 1.4 V *vs.* SCE in 0.1 M H_2SO_4 solution). The oxidative degradation of PEDOT has been studied most frequently using cyclic voltammetry, impedance spectroscopy (EIS) or electron spin resonance (ESR) spectroscopy [5,10-13]. On the other hand, in Refs. [6-8] it has been shown that PEDOT films in modified electrodes undergo structural changes during the degradation process. The most probable stages involved in the overoxidation/degradation process are:

1) Overoxidation results in stress generation in the PEDOT film [14].
2) Formation of cracks due to internal stress.
3) The products of the degradation of the polymer leave the polymer layer.
4) After the formation of the line cracks, the film stress is partially released.
5) The partial delamination of the polymer layer leads to the exposure of the underlying metal substrate to the electrolyte solution.

Nevertheless, the polymer film still present on the substrate after overoxidation remains electroactive; and the areas with the polymer form a barrier between the metal substrate and the surrounding electrolyte solution. Apart from the morphological changes, overoxidation can also affect the charge structure of the polymer film. Poly(3,4-ethylenedioxythiophene) is a redox conductive polymer that incorporates counterions from the electrolyte solution to maintain electroneutrality; thus, its charging processes involve a detectable counter-ion flux leaving the film [15]. The above conclusions seem to be confirmed by the experimental data, but they give no information about the processes occurring after overoxidation of the polymer film.

For instance, it is known that the impedance spectra of overoxidized poly(3,4-ethylen-edioxytiophene) (PEDOT) films on gold recorded in aqueous sulphuric acid solutions differ from those measured for freshly prepared films [12]. The most interesting feature is the appearance of an arc (or a "depressed semicircle") at high frequencies in the complex plane impedance plot. The time evolution of the impedance spectra is another remarkable feature of the electrodes with overoxidized PEDOT films [16,17]. According to this observation, the charge transfer resistance (R_{ct}) at the (electronically conductive) substrate/polymer film interface decreases continuously over several hours when the potential is held in the "stability region" after overoxidation of the film. This means that the impedance spectra recorded using the consecutive frequency sweep

mode (typical of EIS) are corrupted by typical errors caused by the system evolution during the experiment. According to the usual interpretation of the concept of impedance, impedance is not defined as time-dependent and, therefore, there should not exist an impedance out of stationary conditions. This means that if the requirement of stationarity in impedance spectroscopy is in conflict with the essential properties of the object, the measured data points are not "impedances", the obtained sets of experimental data are not "impedance spectra" and they cannot be used in any analysis based on impedance models.

There are some methods proposed in the literature to deal with a non-stationary behavior. Stoynov proposed a method of determining "instantaneous" ("calculated", "corrected" or "synthetic") impedance diagrams for non-stationary systems based on a four-dimensional approach [18-22] (see Supplementary Material). Recently, the method have been successfully applied for the determination of the charge transfer resistance and some other characteristic impedance parameters of the gold|poly(3,4-ethylenedioxytiophene) (PEDOT)| sulfuric acid (*aq*) electrode corresponding to different time instants, including the time instant just after the overoxidation of the polymer film, demonstrating that the 4-dimensional analysis method can not only be used for the correction of the existing (experimentally measured) impedance data, but it opens up the possibility of the estimation of the impedance spectra outside the time interval of the impedance measurements. According to the results presented in [16,17], the high and medium frequency regions of the impedance spectra are stronger affected by the time evolution than the values measured at low frequencies.

In ref. [17] the following explanation was given for the decrease of the charge transfer resistance with time after overoxidation: During overoxidation at sufficiently positive potentials a significant fraction of the polymer chains become detached from the substrate surface (i.e. "desorption", "deactivation" or "delamination" occurs). In contrary this, at a less positive potential the readsorption of the polymer chains (polymer chain ends) becomes possible, that is the number of the polymer chains directly contacted with (adsorbed on) the substrate surface is increasing with the passing time. This means that during overoxidation the "effective" coverage of the substrate by the polymer decreases, and at less positive potentials the coverage may start to increase again. The direction of the change in R_{ct} is in complete agreement with this hypothesis. On the other hand, there are also objections that can be raised against the above arguments. For instance, an opponent could argue that the gold oxide layer formation on the gold substrate surface plays the most important role in the observed relaxation process by preventing adsorption (or readsorption) of the polymer chains on the surface. However, this would mean that the behavior of the pedot/gold system is special, and in case of other substrates (*e.g.* glassy carbon) the post-overoxidation properties of the PEDOT-modified electrodes are different.

In the present study the electrochemical properties of poly(3,4-ethylenedioxythiophene) films deposited on glassy carbon substrates have been investigated in aqueous sulfuric acid solutions with the aim to reveal the similarities and differences between the behavior of PEDOT-modified glassy carbon (GC) and gold electrodes.

Experimental

All electrochemical measurements were performed with a computer driven electrochemical workstation (Zahner IM6 controlled by a Thales software package) in a three-electrode arrangement.

Electrodeposition of PEDOT: Poly(3,4-ethylenedioxytiophene) films were prepared by galvanostatic deposition on both sides of thin gold and glassy carbon plates from 0.01 mol·dm^{-3} ethylenedioxytiophene (EDOT) solution containing 0.1 mol·dm^{-3} Na_2SO_4 supporting electrolyte. Analytical grade 3,4-ethylenedioxythiophene (Aldrich), *p.a.* Na_2SO_4 (Fluka), and ultra-pure water (specific resistance 18.3 MΩ cm) were used for solution preparation. All solutions were purged with oxygen-free argon (Linde 5.0) before use and an inert gas blanket was maintained throughout the experiments.

The deposition was performed with galvanostatic method. The gold or glassy carbon plate in contact with the solution served as the working electrode (WE). A Pt wire immersed in the same solution served as the counter electrode (CE), and a KCl-saturated calomel electrode (SCE) as the reference electrode (RE). A constant current density of j = 0.2 mA·cm^{-2} (I = 0.2 mA) was applied for 1000 s (the geometric surface areas of the working electrodes were A = 1.0 cm^2). The film thickness was estimated from the polymerization charge by using the charge/film volume ratio determined earlier by direct thickness measurements [2,23,24]. The average thickness of the PEDOT film was about 0.8 μm, the structure of the PEDOT film was globular, cauliflower-like[8,9], i.e. the thickness of the film was non-uniform.

Cyclic voltammetry and impedance measurements: Solutions used for cyclic voltammetric and impedance measurements were prepared with ultra-pure water and p.a. H_2SO_4 (Merck). The solutions were purged with oxygen-free argon (Linde 5.0) before use and an inert gas blanket was maintained throughout the experiments. In the conventional three-electrode cell configuration the PEDOT-modified gold or glassy carbon substrate in contact with the solution was used as the working electrode (WE), a bended gold plate immersed in the same solution as the counter electrode (CE), and a NaCl-saturated calomel electrode (SSCE) as the reference electrode (RE). The counter electrode was arranged cylindrically around the working electrode to maintain a uniform electric field. The overoxidation of the PEDOT film was carried out in 0.1 mol·dm^{-3} H_2SO_4 solution a day after the deposition.

Results and discussion

Cyclic voltammetry

According to Fig.1 cyclic voltammograms in the potential range -0.1 – 0.6 V vs SSCE were recorded before the overoxidation. Both in the cases of Au |PEDOT and GC |PEDOT the cyclic voltammograms change significantly if the positive limit of the electrode potential is extended to 1.5 V vs. SCE ("strong" overoxidation, curves 2–4 in Fig. 1a and 1b). It is well known [5-9,12,25] that between –0.3 and 0.8 V *vs.* SSCE the oxidation-reduction process of the PEDOT films is reversible. However, at more positive potentials irreversible degradation of the polymer layer occurs. As it can be seen in Fig. 1a and in Fig. 1b (curve 1), the cyclic voltammograms of PEDOT-modified electrodes show almost pure capacitive behavior in the potential range between -0.1 V and +0.6 V, i.e. if the positive potential limit is kept below 0.8 V *vs.* SSCE. If the polarization potential exceeds this critical value an oxidation peak without corresponding reduction peak appears (see curves 2-4 in Fig. 1a and 1b).

As can be seen from from Fig. 2 the charge consumed during the oxidation process is different for the two types of electrodes. According to the results the overoxidation is more intensive in the case of Au|PEDOT electrodes than in the case of the GC|PEDOT system. The different shapes of the 2nd and 3rd CV-s may indicate that the anodic overoxidation results in a more passive surface in the case of the GC substrate.

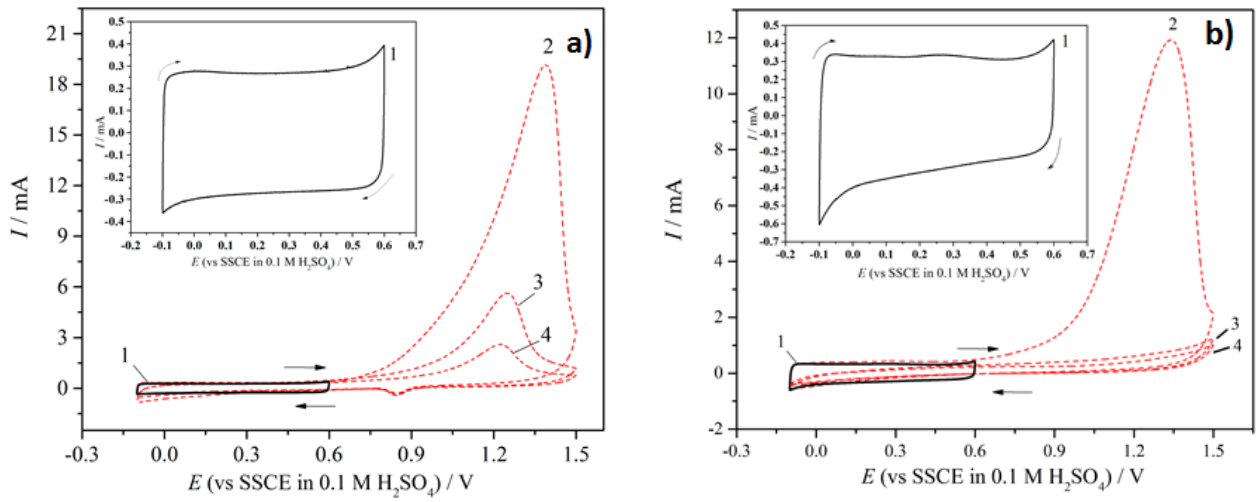

Fig. 1. *Curve 1: Cyclic voltammetric curves recorded before overoxidation a) Au|PEDOT|0.1 M H_2SO_4 b) GC|PEDOT|0.1 M H_2SO_4 electrode in the potential range from -0.1 V to 0.6 V* vs. *SSCE. Curves 2-4: Successive cyclic voltammograms („overoxidation cycles") recorded on a) Au|PEDOT|0.1 M H_2SO_4 b) GC|PEDOT|0.1 M H_2SO_4 electrode in the potential range from -0.1 V to 1.5 V* vs. *SSCE. The sweep rate was* ν *= 50 mV/s in all case*

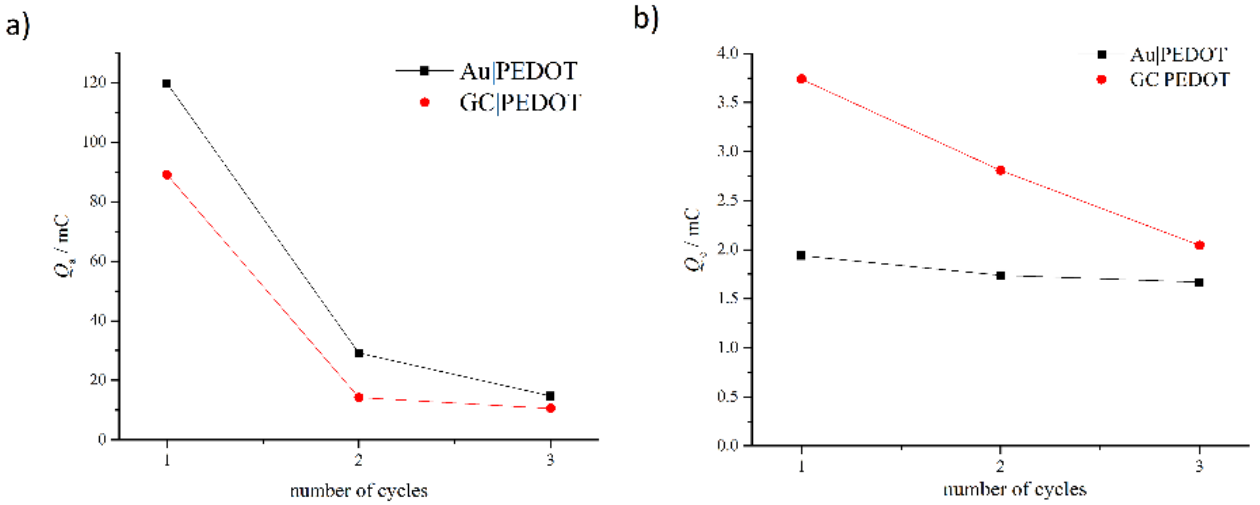

Fig. 2 *Change of the (a) anodic and (b) cathodic charges with the number of overoxidation cycles.*

The decrease in the cathodic charges of the (over)oxidized polymer films are considerably smaller.

Fig. 3 shows the schematic representation of the suggested process in connection with the Au|PEDOT system. In the beginning, *i.e.* in the pristine films, the sulfur atoms of the PEDOT chains are connected to the gold surface. As already mentioned in the introduction, during overoxidation at sufficiently positive potentials a significant fraction of the polymer chains become detached from the substrate surface. In parallel with this process the oxidation of the electrode leads to the formation of a gold oxide layer. This atomic oxide layer can block the active surface temporarily and ad interim hinders the adhesion interactions with the polymer chains. This effect may be operative in the present case too. On the other hand, after the overoxidation treatment, at a less positive potentials the readsorption of the polymer chains (polymer chain ends) becomes possible. This means that during overoxidation the "effective" coverage of the substrate by the polymer decreases, and at less positive potentials the coverage may start to increase again. The direction of

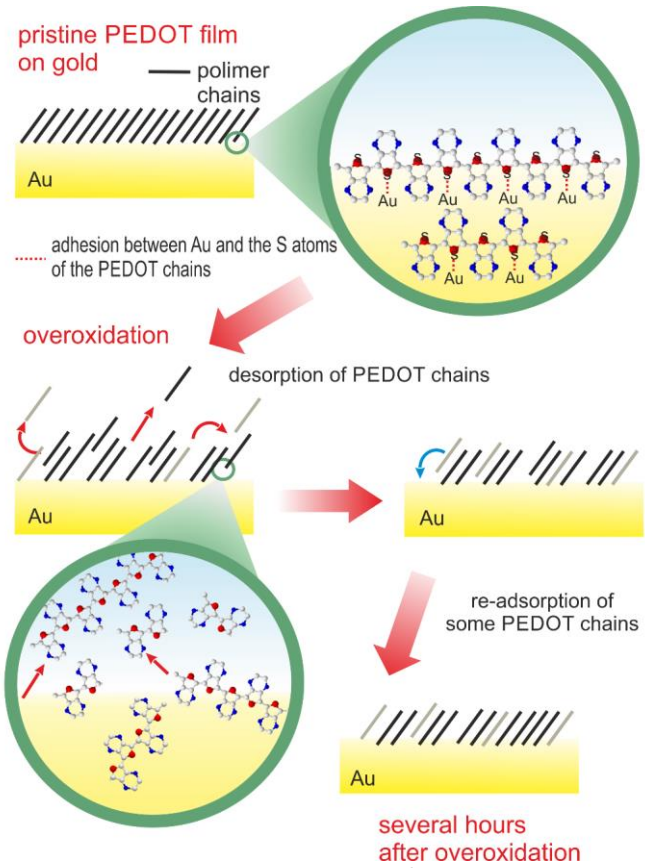

Fig.3 *The suggested mechanism of the desorption and re-adsorption polymer chains during the overoxidation process and after overoxidation (when the potential is held in the "stability region").*

the change in R_{ct} is in agreement with this hypothesis. In the case of glassy carbon substrate, the overoxidation of PEDOT can take place in the same way in the polymer chains, however, no reduction peak can be observed in the cyclic voltammograms of the GC|PEDOT|0.1 M H_2SO_4 electrode (see Fig. 1b). This difference can be explained on the basis of the electrochemical properties of the two substrates. It is well known that the electrochemical behavior of gold in aqueous media has been thoroughly studied, and the voltammetric behavior of gold in acidic media can be explained by monolayer oxide formation/removal and adsorption phenomena. The structure and electrochemical characterization of vitreous or glassy carbon has been the subject of research since it was first produced in the early 1960s. Some early structural models assumed that both complex sp2- and sp3-bonded carbon atoms were present, but this idea is now discarded and many of the properties suggest a 100 % sp2 bonding [27]. The Jenkins–Kawamura [28] model suggests that glassy carbon consists a long, narrow and imperfect aromatic ribbons. More recent studies have revealed that glassy carbon be made up of graphitic sp2 ribbons (*i.e.* the structure of glassy carbon consists of long, randomly oriented microfibrils, however, it has also been suggested that glassy carbon comprises a fullerene-type structure [29]) and hybridized carbon atoms with oxygen-containing groups (including oxygen-containing surface functionalities as hydroxyl, phenol, lactone, carbonyl, o-quinone and p-quinone, *etc.*) along the edges of these ribbons where the graphite layer terminates [30,31]. PEDOT that contains ethylenedioxy-bridge and sulfur atom at the end of the polymer chain can easily grow on and strongly adhere to the GC surface. Cyclic voltammograms recorded in 0.1 M sulfuric acid solution reveal that irreversible oxidation of the (bare) glassy carbon surface takes place at electrode potentials more positive than about 0.6 V *vs.* SSCE (Fig 4a). The negative limit of this potential range roughly coincides with the PEDOT overoxidation onset potential region therefore the surface oxidation may occur in parallel with the (gradual) desorption of the polymer chains.

On the other hand, the smooth surface of the pristine polished GC becomes roughened with electrochemical oxidation [32,33], the surface becomes more and more porous and the effective surface area increases. The electrolyte solution can penetrate into the pores, which leads to the increase of the capacitance.

The contribution of pseudo-capacity to double-layer charging/discharging currents originates mostly from fast faradaic reactions of redox active surface carbon oxygen containing species (*e.g.* hydroquinione/quinone couple), formed at the exposed edge plane sites of carbon [34]. As it can be seen in Fig 4b there is no significant difference between cyclic voltammograms obtained before

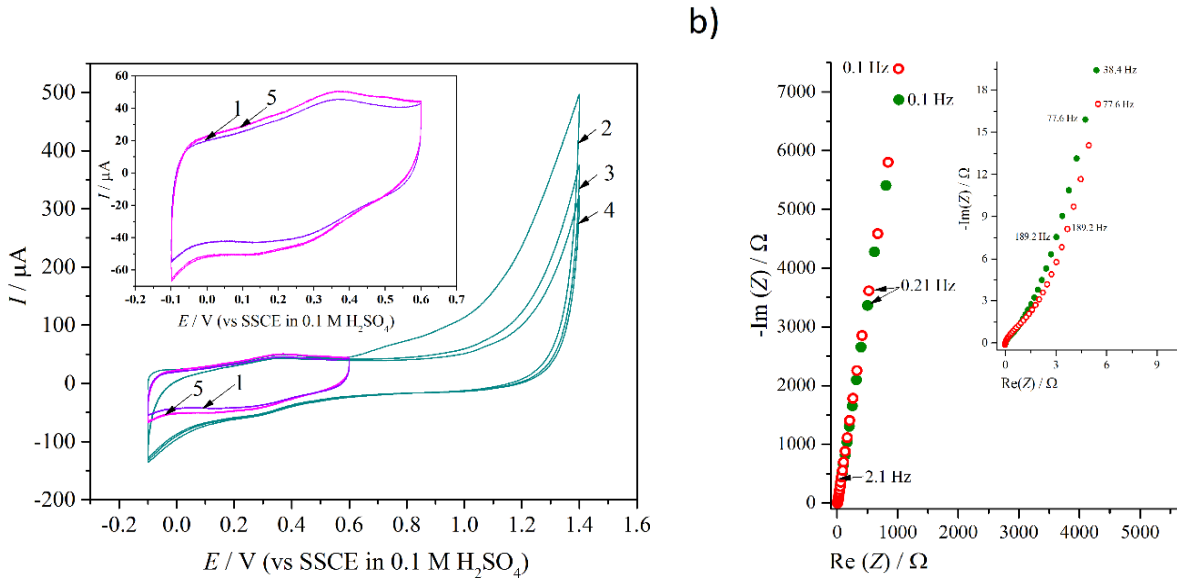

Fig. 4. *a) Cyclic voltammograms recorded on bare glassy carbon in 0.1 M H_2SO_4 vs SSCE. Curve 1 was recorded before, and curve 5 after the three subsequent oxidation cycles (curves 2-4). The sweep rate was 50 mV / s. b) Complex plane impedance diagram of the bare GC in 0.1 M H_2SO_4 recorded at 0.4 V* vs. *SSCE before (○) and immediately after (●) three oxidation cycles. The impedance spectra were recorded at 60 discrete frequencies between 0.1 Hz and 100 kHz (amplitude: 5 mV rms).*

and after the oxidative treatment. (It should also be noted here that the same statement is true for the charge transfer resistances determined by impedance spectroscopy before and after the oxidation.)

Impedance measurements

After overoxidation, subsequent impedance measurements were performed on the GC|PEDOT|0.1 M H_2SO_4 electrode at the electrode potential E = 0.4 V *vs.* SSCE over a frequency range from 100 mHz to 100 kHz as described in the experimental section (starting at τ_2 in Fig. 5a). The Fig. 5b and Fig. 5c data points were measured using AC signal amplitude of 5 mV at 60 discrete frequencies in the frequency region investigated during each scan. The time moment corresponding to τ_2 was taken as the starting time of the impedance measurements ("timestamp": t = 0 s), and 63 successive impedance spectra were recorded. It is (somewhat arbitrarily) assumed that the overoxidaton process stopped completely at τ_1, *i.e.* at t = -50.0 s and $\Delta\tau$ = 50.0 s (see Fig. 5a). The recording time of a "single" spectrum was about 346 s. In Fig. 5b and in Fig. 4b the results are presented in the complex plane (where Re(Z) is the real part and Im(Z) is the imaginary part of the complex impedance, respectively). For the sake of comparison sets of impedance data measured for an Au|PEDOT|0.1 M H_2SO_4 electrode after overoxidation under similar conditions are presented in Fig. 5c. As we can see from Figs. 5b and 5c, the pristine PEDOT films show very small charge transfer resistances and close to ideal capacitive characteristics. On the other hand, the diameters of the capacitive arcs at high frequencies (and hence the charge transfer resistances) increase significantly during overoxidation both in the case of GC|PEDOT|0.1 M H_2SO_4 and Au|PEDOT|0.1 M H_2SO_4 electrodes. The analysis of the impedances obtained for the GC|PEDOT|0.1 M H_2SO_4 electrode were carried out in the same way described in refs [16,17,21, see also Supplementary Material]. The calculation of the "instantaneous" impedance diagrams was carried out using the real and imaginary parts of the impedances measured at identical frequencies („isofrequential components"). The charge transfer resistances at t = 0 s has been obtained by extrapolation of the iso-frequency dependencies to this time instant.

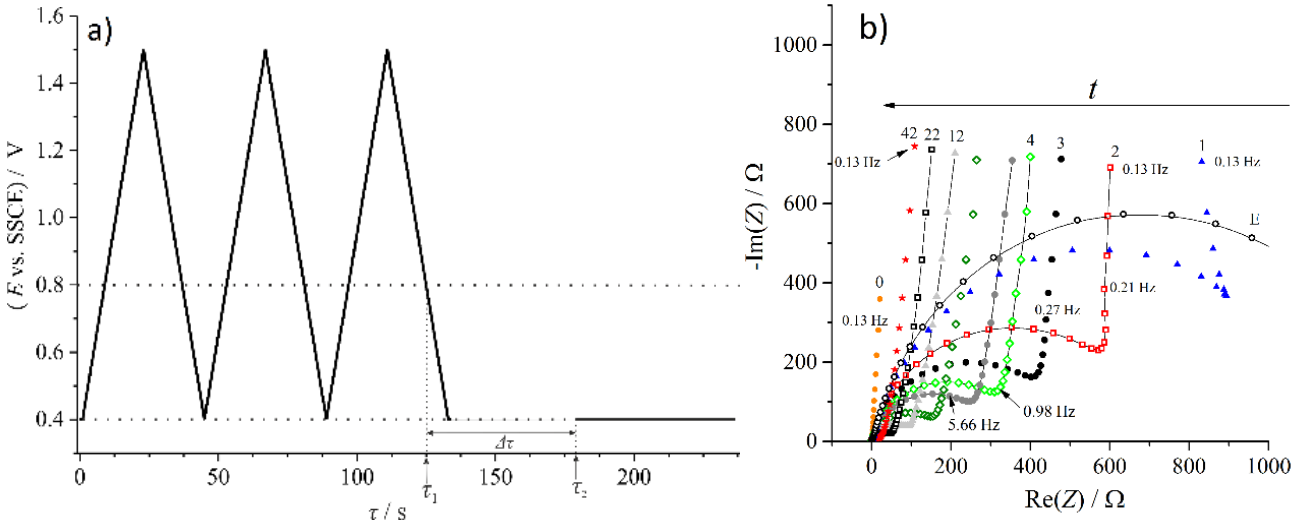

Fig. 5

a) The potential program applied to the GC|PEDOT|0.1 M H_2SO_4 electrode. The impedance measurements started at τ_2. τ_1 *is the estimated end of the overoxidaton process.* $\Delta\tau$ *= 50 s.*

b) Successive (measured) impedance diagrams recorded on the GC|PEDOT|0.1 M H_2SO_4 and

c) Au|PEDOT|0.1 M H_2SO_4 on the electrode at E*= 0.4 V* vs. *SSCE. The solid lines are to guide the eye only: not curve fits.*

The spectra signed by E in Figs. 5 b and 5 c are calculated spectra corresponding to the presumed ends of the overoxidation processes, b) t *= -50 s, c)* t *= -53 s, respectively.*

(The spectra E were calculated using the method of Stoynov [16,17].)

The values of the charge transfer resistances at $t = 0$ s and at the other time instants were estimated by fitting the high-frequency part of the "instantaneous" spectra with the impedance function (Eq. 1) corresponding to the equivalent-circuit analog shown in the inset of Fig. 6.

$$Z(\omega) = R_u + \frac{1}{B(i\omega)^{\alpha} + R_{ct}^{-1}} \quad (1)$$

In Eq. 1 R_{ct} is the charge transfer resistance and R_u is the uncompensated ohmic resistance (which is mainly the resistance of the electrolyte solution between the working and the reference electrode). This simple equivalent circuit is based on the model proposed *e.g.* in [13,35], wherein the high frequency ("double layer") capacitance (C_d) at the substrate/polymer interface has been replaced by a constant-phase element (CPE), which more accurately imitates the nonideal (distributed) behavior of the double layer ($Z_{CPE} = 1/B(i\omega)^{-\alpha}$, where i is the imaginary unit, B and α are the CPE parameters, and ω is the angular frequency, respectively).

The estimated values of the parameters (obtained by complex non-linear least squares (CNLS) fitting program based on the Gauss – Newton – Levenberg - Marquardt method with inverse magnitude weighting) are shown in Table 1. The spectra calculated (simulated) by using the "best-fit" parameters are shown Fig. 6.

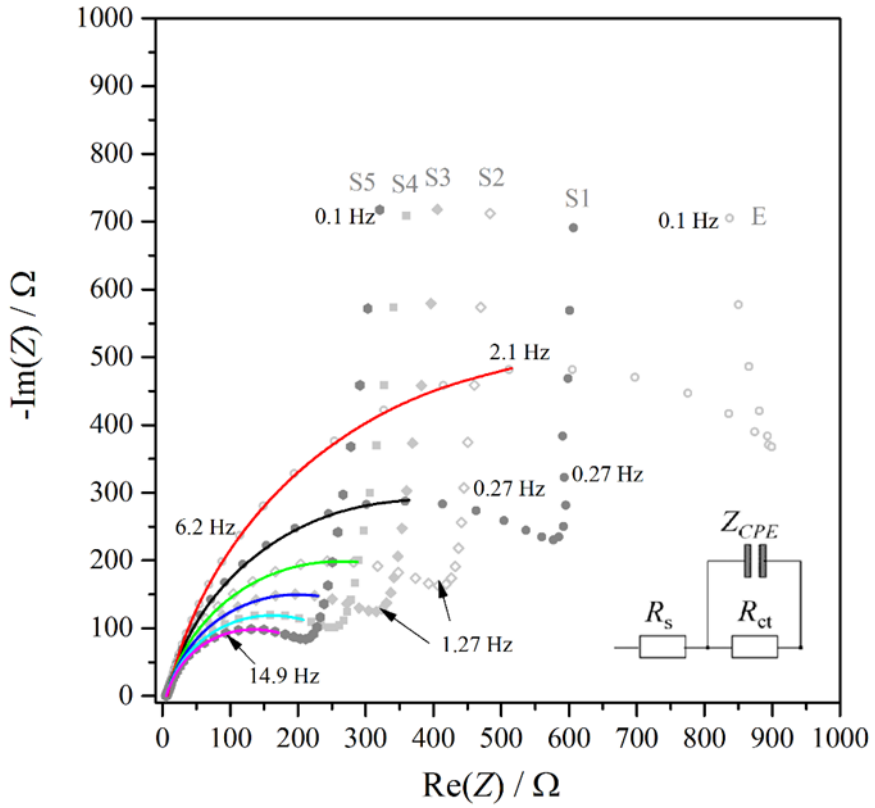

Fig. 6. *Corrected complex plane impedance diagrams ("instantaneous impedances") of the GC|PEDOT|0.1 M H_2SO_4 system calculated for* t *= -50.0 s (E),* t *= 0 s (S1),* t *= 346.6 s (S2),* t *= 692.5 s (S3),* t *= 1039.4 s (S4), and* t *= 1386.7 s (S5), respectively. The solid curves were calculated (simulated) by using the "best-fit" parameters given in Table 1.*

Table 1. *Results of CNLS fitting of impedance data of GC|PEDOT system: the estimated values of the parameters.* R_u *is the uncompensated ohmic resistance (resistance of the solution),* R_{ct} *is the charge transfer resistance,* B *and* α *are the parameters of the CPE,* ΔR_u, ΔR_{ct}, ΔB *and* $\Delta\alpha$ *are the corresponding 95 % confidence intervals.*

data set	t / s	R_u / Ω	ΔR_u / Ω	R_{ct} / Ω	ΔR_{ct} / Ω	B / $\Omega^{-1}s^{\alpha}$	ΔB / $\Omega^{-1}s^{\alpha}$	α	$\Delta\alpha$
E	-50.0	7.8	±1.5	1391.4	±1.3	$2.91\cdot10^{-5}$	$\pm0.12\cdot10^{-6}$	0.878	±0.045
S1	0	7.22	± 0.42	1222.4	±6.7	$2.55\cdot10^{-5}$	$\pm0.41\cdot10^{-6}$	0.863	±0.019
S2	346.6	6.15	± 0.57	728.2	±6.7	$2.11\cdot10^{-5}$	$\pm0.64\cdot10^{-6}$	0.855	±0.037
S3	692.5	5.96	± 0.58	507.2	±5.3	$1.82\cdot10^{-5}$	$\pm0.75\cdot10^{-6}$	0.849	±0.047
S4	1039.4	5.99	± 0.51	384.9	±4.3	$1.93\cdot10^{-5}$	$\pm0.76\cdot10^{-6}$	0.845	±0.051
S5	1386.7	5.69	±0.54	258.6	±3.6	$1.76\cdot10^{-5}$	$\pm0.95\cdot10^{-6}$	0.831	±0.070
S6	1765.0	5.83	±0.42	219.9	±2.9	$1.76\cdot10^{-5}$	$\pm0.87\cdot10^{-6}$	0.829	±0.066
S7	2113.5	5.93	±0.33	190.7	±2.4	$1.76\cdot10^{-5}$	$\pm0.74\cdot10^{-6}$	0.828	±0.059
S8	2464.7	5.39	±0.56	172.6	±3.1	$1.57\cdot10^{-5}$	$\pm0.16\cdot10^{-6}$	0.807	±0.097
S9	2823.9	5.56	±0.42	153.7	±2.5	$1.59\cdot10^{-5}$	$\pm0.99\cdot10^{-6}$	0.809	±0.084
S10	3173.1	5.88	±0.30	138.2	±1.9	$1.62\cdot10^{-5}$	$\pm0.82\cdot10^{-6}$	0.810	±0.071
S11	3522.3	5.73	±0.20	125.6	±1.5	$1.63\cdot10^{-5}$	$\pm0.61\cdot10^{-6}$	0.811	±0.054
S12	3872.1	5.88	±0.14	114.9	±1.1	$1.65\cdot10^{-5}$	$\pm0.47\cdot10^{-6}$	0.812	±0.043

Some of the charge transfer resistance values (the R_{ct} *vs.* t plot) determined for the GC|PEDOT|0.1 M H_2SO_4 by using the "instantaneous" impedances are shown in Fig. 7a. It can be seen from Table 1 (and from Fig. 7a), that the highest value of R_{ct} is about (1391.4±1.3) Ω. This value corresponds to the time instant just after overoxidation of the film. Similarly to the Au|PEDOT|0.1 M H_2SO_4 electrode (see Fig. 7b), starting from this value, R_{ct} decreases continuously with experiment time to a value somewhat higher than the charge transfer resistance of the

pristine electrode. It can clearly be concluded that the charge transfer resistances measured for the GC|PEDOT|0.1 M H_2SO_4 electrode after overoxidation are significantly higher than those measured for the Au|PEDOT|0.1 M H_2SO_4 electrode, however, the relative rate of the relaxation process is apparently higher (the "half-life" of R_{ct} for GC|PEDOT is about $t_{1/2,GC} \approx 400$ s, while for Au|PEDOT $t_{1/2,Au} \approx 860$ s).

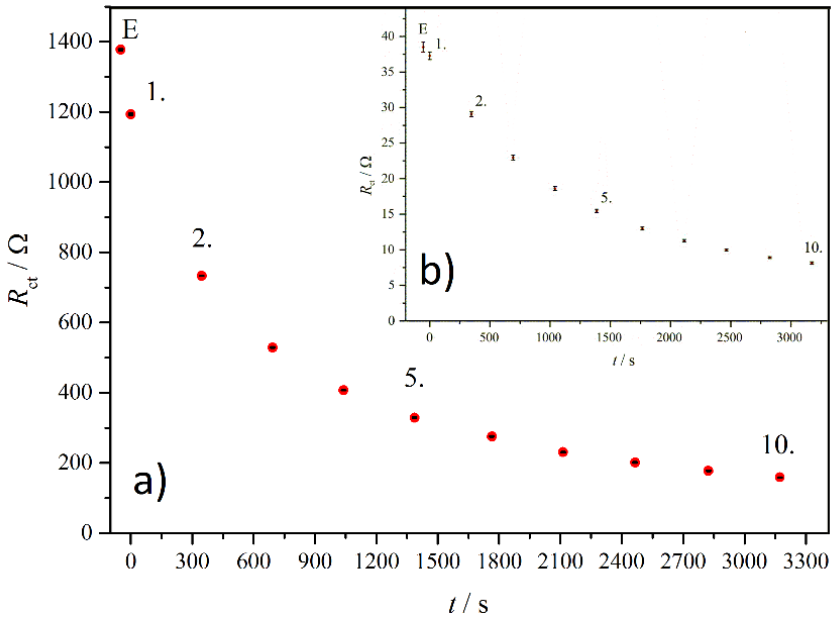

Fig. 7 *Time evolution of the charge transfer resistance during the experiment in the case of GC|PEDOT|0.1 M H_2SO_4 electrode (a) and Au|PEDOT|0.1 M H_2SO_4 electrode (b, see insert).* R_{ct} *values were determined using the calculated impedance spectra. In both cases: The* R_{ct} *value designated by* E *corresponds to the time instant of the presumed end of the overoxidation processes:* t = *-50.0 s (GC|PEDOT) and* t = *-53.0 s (Au|PEDOT).*

As it can be seen from the results, the direction, dynamics and nature of the temporal change in R_{ct} are consistent with the hypothesis outlined in [17] and in the introduction to this study. We can assume that during overoxidation a significant fraction of the polymer chains become detached from the substrate surface. The partial delamination of the polymer layer leads to the exposure of the underlying substrate material to the electrolyte solution. In areas where the substrate is in direct contact with the electrolyte solution, practically no charge transfer across the interface occurs (i.e. the local charge transfer resistance is close to infinite). Nevertheless, the polymer film still present on the substrate after overoxidation remains electroactive. At the electrode potential of $E = 0.4$ V *vs.* SSCE the readsorption of the polymer chains (polymer chain ends) becomes possible, i.e. the number of the polymer chains directly contacted with (adsorbed on) the substrate surface is increasing with the passing time. In other words, during overoxidation the "effective" coverage of the substrate by the polymer decreases, and at less positive potentials the coverage starts to increase again, leading to the decrease of the charge transfer resistance.

The reasoning above leads us to the conclusion that in the case of the GC|PEDOT|0.1 M H_2SO_4 electrode the number of irreversibly oxidized (desorbed or deactivated) polymer chains (or polymer chain ends) per unit area is greater than in the case of the Au|PEDOT|0.1 M H_2SO_4 electrode. However, this fact does not explain the apparent difference in the relative rates of decay of R_{ct} in the two systems.

A plausible mechanistic explanation of this behavior is based on the differences in the chemical states of the substrate surfaces. In the case of Au|PEDOT|0.1 M H_2SO_4 after the last overoxidation CV (at $E = 0.4$ V *vs.* SSCE, the electrode potential was kept at this value during the impedance spec-

troscopy measurements, as well) the whole of the oxide is completely reduced, as is evident from the appearance of the reduction peak in Fig. 1a (and is well known from the electrochemistry of gold [36,37]). On the other hand, it is quite clear from Fig. 4 that immediately after an oxidation cycle up to a positive potential limit of E = 1.4 V *vs.* SSCE, the electrochemical reduction of the surface of glassy carbon at 0.4 V *vs.* SSCE is incomplete. This means, that in the case of the GC|PEDOT|0.1 M H_2SO_4 electrode two processes may occur simultaneously during the impedance measurements: (a) reduction of the oxidized surface of the GC substrate, including the reduction of oxygen-containing surface functionalities and (b) readsorption of the polymer chains (polymer chain ends) on the surface. The extent of the first process will clearly influence the rate at which the other can proceed, manifesting in the increase in the rate of decay of the charge transfer resistance.

Nevertheless, it should be noted here, that other processes may also occur during the overoxidation process, *i.e.* chemical changes in the polymer chains that affect the extent of charging and the conjugation of the PEDOT chains and slow conformational relaxation phenomena of the polymer structure that may not be necessarily influenced by the substrate.

Conclusions

The 4-dimensional analysis method, originally proposed by Stoynov, was successfully applied for the determination of the charge transfer resistance of a glassy carbon|PEDOT|0.1 mol·dm^{-3} sulfuric acid (aq.) electrode corresponding to different time instants after overoxidation. During the impedance measurements carried out almost immediately after the overoxidation procedure the electrode potential was held in the "stability region" of the system (at E = 0.4 V vs. SSCE in the present case). The post-experimental mathematical/analytical procedure could be used also for the estimation of the charge transfer resistance corresponding to the time instant just after overoxidation of the PEDOT film. The decreasing capacitance and the increasing resistance suggest that during overoxidation the electrochemical activity of the film decreases and the charge transfer process at the metal/film interface becomes more hindered than in the case of pristine films. During the impedance measurements the charge transfer resistance decreased continuously with experiment time, the "starting" (calculated) R_{ct} value was approximately 1391 Ω·cm^2. After 50 seconds this value fell to about 1222 Ω·cm^2, i.e. it decreased by ~12 % in the first minute after the overoxidation procedure.

By comparing the properties of the GC|PEDOT|0.1 M H_2SO_4 and the Au|PEDOT|0.1 M H_2SO_4 electrodes a possible mechanistic explanation for the observed behavior has been proposed. This is based on the assumption that in the case of the GC|PEDOT|0.1 M H_2SO_4 electrode two processes may occur simultaneously during the impedance measurements: (a) reduction of the oxidized surface of the GC substrate (including the reduction of oxygen-containing surface functionalities), and (b) readsorption of the polymer chains (polymer chain ends) on the surface.

Acknowledgements*: Support from the Hungarian Scientific Research Fund, the National Research, Development and Innovation Office - NKFI (grants No. K 109036, VEKOP-2.3.2-16.*

References

[1] C. Kvarnström, *Poly(thiophene), in: Electrochemical Dictionary*, 2*nd* edn., A. J. Bard, G. Inzelt, F. Scholz (Eds.), Springer, Heidelberg (2012).
[2] J. Bobacka, A. Lewenstam, A. Ivaska, *J. Electroanal. Chem.* **489** (2000) 17–27.
[3] H. Yamato, M. Ohwa, W. Wernet, *J. Electroanal. Chem.* **397** (1995) 163–170.
[4] N. Sakmeche, S. Aeiyach, J. J. Aaron, M. Jouini, J. C. Lacroix, P. C. Lacaze, *Langmuir* **15** (1999) 2566–2574.

[5] A. Zykwinska, W. Domagala, B. Pilawa, M. Lapkowski, *Electrochim. Acta* **50** (2005) 1625–1633.
[6] M. Ujvári, M. Takács, S. Vesztergom, F. Bazsó, F. Ujhelyi, G. G. Láng, *J. Solid State Electrochem.* **15** (2011) 2341–2349.
[7] G. G. Láng, M. Ujvári, F. Bazsó, S. Vesztergom, F. Ujhelyi, *Electrochim. Acta* **73** (2012) 59–69.
[8] M. Ujvári, J. Gubicza, V. Kondratiev, K. J. Szekeres, G. G. Láng, *J. Solid State Electrochem.* **19** (2015) 1247–1252.
[9] M. Ujvari, G. G. Láng, S. Vesztergom, K. J. Szekeres, N. Kovács, J. Gubicza, *J. Electrochem. Sci. Eng.* **6** (2016) 77-89.
[10] A. Zykwinska, W. Domagala, A. Czardybon, B. Pilawa, M. Lapkowski, *Electrochim. Acta* **51** (2006) 2135–2144.
[11] X. Du, Z. Wang, *Electrochim. Acta* **48** (2003) 1713–1717.
[12] G. G. Láng, M. Ujvári, S. Vesztergom, V. Kondratiev, J. Gubicza, K. J. Szekeres, *Zeitschrift fur Phys. Chemie* **230** (2016) 1281–1302.
[13] G. Inzelt, G. G. Láng, *Electrochemical Impedance Spectroscopy (EIS) for Polymer Characterization, Ch. 3, in: Electropolymerization: Concepts, Materials and Applications*, S. Cosnier, A. Karyakin (Eds.), Wiley-VCH Verlag GmbH & Co. KGaA,Weinheim, 2010.
[14] G. G. Láng, C. Barbero, *Laser techniques for the study of electrode processes, in: Monographs in electrochemistry*, F. Scholz (Ed.), Springer, Berlin Heidelberg (2012).
[15] N. Kovács, M. Ujvári, G. G. Láng, P. Broekmann, S. Vesztergom, *Instrum. Sci. Technol.* **43** (2015) 633–648.
[16] M. Ujvári, D. Zalka, S. Vesztergom, S. Eliseeva, V. Kondratiev, G. G. Láng, *Bulg. Chem. Commun.* **49** (2017) 106–113.
[17] D. Zalka, N. Kovács, K.J. Szekeres, M. Ujvári, S. Vesztergom, S. Eliseeva, V. Kondratiev, G. G Láng, *Electrochim. Acta* **247** (2017) 321–332.
[18] Z. Stoynov, B. Savova, *J. Electroanal. Chem.* **112** (1980) 157–161.
[19] Z. B. Stoynov, B. S. Savova-Stoynov, *J. Electroanal. Chem.* **183** (1985) 133–144.
[20] B. Savova-Stoynov, Z. B. Stoynov, *Electrochim. Acta* **37** (1992) 2353–2355.
[21] G. G. Láng, D. Zalka, *Physiol. Meas.* **39** (2018) 028001(4pp).
[22] V. Horvat-Radošević, K. Kvastek, K. Magdić Košiček, *Bulg. Chem. Commun.* **49** (2017) 119–127.
[23] W. Poppendieck, K. P. Hoffmann, *IFMBE Proc.* **22** (2008) 2409–2412.
[24] A. Stoyanova, V. Tsakova, *J. Solid State Electrochem.* **14** (2010) 1947–1955.
[25] D. Zalka, S. Vesztergom, M. Ujvári, G. G. Láng, *6th Regional Symposium on Electrochemistry - South-East Europe,* Balatonkenese, Hungary, 11-15 June, 2017, Book of Abstracts, pp. 103–104.
[26] G. Láng, M. Ujvári, G. Inzelt, *Electrochim. Acta* 46 (2001) 4159–4175.
[27] P. Melinon, B. Masenelli, *From Small Fullerenes to Superlattices: Science and Applications*, p.74, CRC Press, Taylor&Francis Group, LLC, Boca Raton (2012).
[28] G. M. Jenkins, K. Kawamura, *Nature* **231** (1971) 175–176.
[29] P. J. F. Harris, *Philos. Mag.* **84** (2004) 3159-3167.
[30] R. L. McCreery, *in Electroanalytical Chemistry a Series of Advances*, ed. A. J. Bard, Marcel Dekker, New York, 1991, vol. 17, p. 221.
[31] B. Šljukić, G. G. Wildgoose, A. Crossley, J. H. Jones, L. Jiang, T. G. J. Jones, R. G. Compton, *J. Mater. Chem.* **16** (2006) 970–976.
[32] A. Dekanski, J. Stevanović, R. Stevanović, B.Ž. Nikolić, V.M. Jovanović, *Carbon* **39** (2001) 1195–1205.
[33] Y. Yi, G. Weinberg, M. Prenzel, M. Greiner, S. Heumann, S. Becker, R. Schlögl, *Catal. Today* **295** (2017) 32–40.
[34] K. Magdić, K. Kvastek, V. Horvat-Radošević, *Electrochim. Acta* **117** (2014) 310–321.
[35] G. Láng, G. Inzelt, *Electrochim. Acta* **44** (1999) 2037–2051.
[36] L. D. Burke, P. F. Nugent, *Gold Bull.* ***30*** (1997) 43–53.
[37] L. D. Burke, P. F. Nugent, *Gold Bull.* **31** (1998) 39–50.

J. Electrochem. Sci. Eng. **8(2)** (2018) S9—S10

Open Access : : ISSN 1847-9286

www.jESE-online.org

Supplementary material to

Electrochemical behaviour of poly(3,4-ethylenedioxytiophene) modified glassy carbon electrodes after overoxidation – the influence of the substrate on the charge transfer resistance

Dora Zalka, Soma Vesztergom, Mária Ujvári, Győző G. Láng

Institute of Chemistry, Laboratory of Electrochemistry and Electroanalytical Chemistry, Eötvös Loránd University, Pázmány P. s. 1/A, H-1117 Budapest, Hungary

J. Electrochem. Sci. Eng. **8(2)** (2018) 151-162

The four-dimensional analysis method is based on the assumption for the continuum of the object's state and parameters space. It requires several impedance spectra recorded subsequently at the same set of frequencies (Fig. S1a). Every measured data at a given frequency should additionally contain the time of measurement (these so-called "timestamps" can be the starting or ending times of the measurements of the individual impedance values, arithmetic or other suitably selected averages, *etc.*).

Thus, the experimental data form a set of 4-dimensional arrays, containing frequency, real and imaginary reconstruction of calculated instantaneous impedances. For every measured frequency two one dimensional functions of "iso-frequency dependencies" (*e.g.* for the real and for the imaginary components, Figs S1b and S1c) are constructed. On the basis of the continuity of the evolution, interpolation is performed (e.g. by using interpolating or smoothing cubic spline or other interpolation techniques) resulting in instantaneous projections of the full impedance-time space and "reconstructed" instantaneous impedances related to a selected instant of the time (i.e. the beginning of each frequency scan, Fig S1d). By extrapolation of the iso-frequency dependencies to an instant outside the time interval of the impedance measurements the impedance diagram corresponding to the assumed starting time of the measurement series can be constructed.

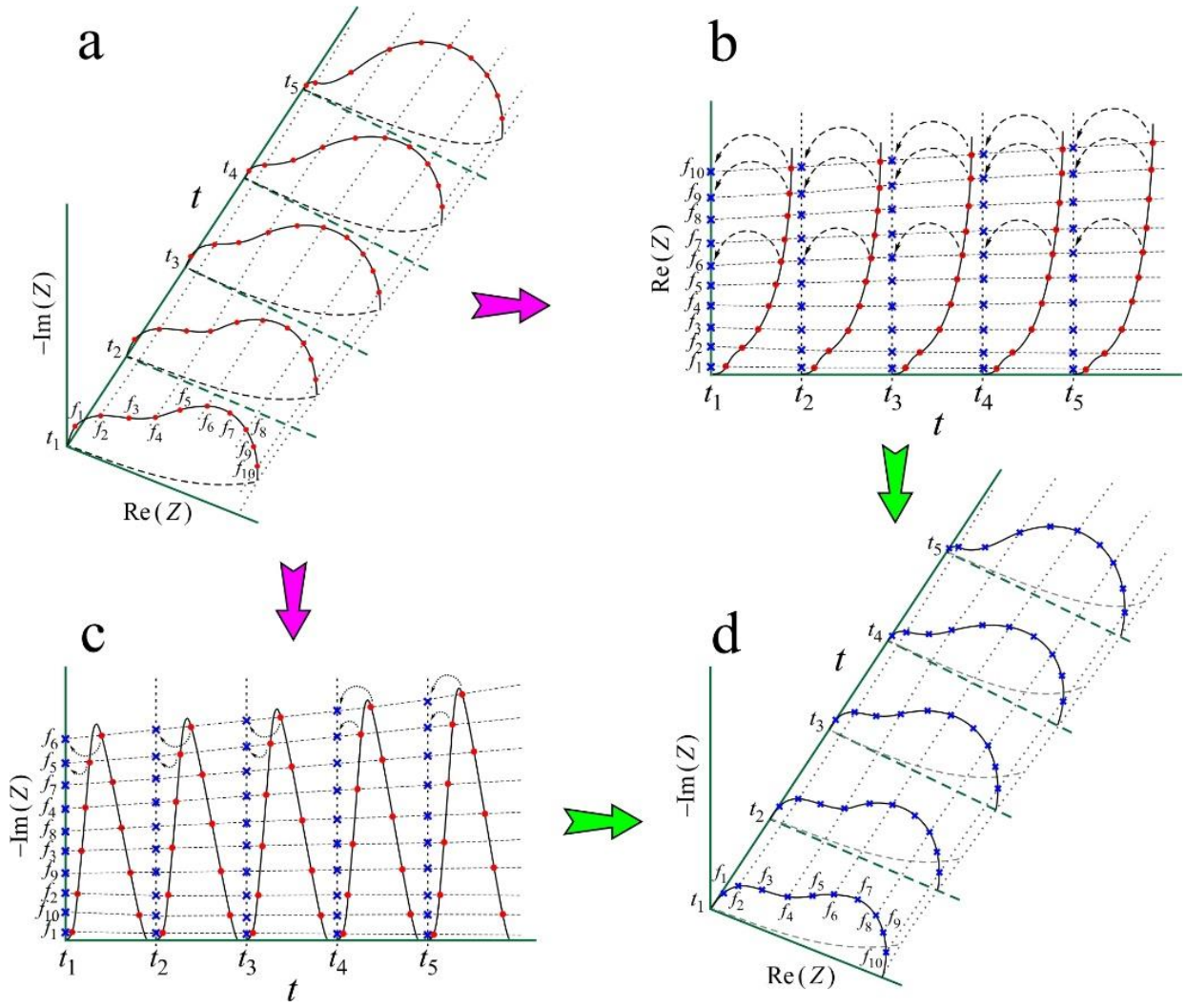

Figure S1. *Scheme of the four-dimensional analysis method. 3-D representation of the impedance and time evolution in the coordinates Re(Z), –Im(Z) and* t *(a), where Re(Z) and Im(Z) are the real and imaginary parts of the complex impedance, respectively,* t *is the time. •: data points (impedances) measured at frequencies* f_i*;* t_i*: starting time of the j-th frequency scan. b) Calculation of the instantaneous (corrected) Re(Z) values (×)by interpolation of the measured Re(Z) data. c) Calculation of the instantaneous (corrected) –Im(Z) values (×) by interpolation of the measured Im(Z) data. d) 3-D representation of the "reconstructed" instantaneous impedances related to the beginning of each frequency scan. ×: corrected data points (impedances) assigned to frequencies* f_i*.*

J. Electrochem. Sci. Eng. **8(2)** (2018) 163-170; DOI: http://dx.doi.org/10.5599/jese.481

Open Access : : ISSN 1847-9286

www.jESE-online.org

Original scientific paper

Electrochemical behaviour of sildenafil citrate at gold and cystein modified gold electrode in acid solution

Jelena Lović✉, Nemanja Trišović[1], Jelena Antanasijević[1], Milka Avramov Ivić

ICTM, Department of Electrochemistry, University of Belgrade, Njegoševa 12, 11000, Belgrade, Serbia

[1]Faculty of Technology and Metallurgy, University of Belgrade, Karnegijeva 4, Belgrade, Serbia

Corresponding author E-mail: ✉jlovic@tmf.bg.ac.rs; Tel.: +381-11-337-0389; Fax: +381-11-337-0389;

Received: November 30, 2017; Revised: February 14, 2018; Accepted: March 21, 2018

Abstract

Electrochemical behavior of sildenafil citrate (SC) at gold and cystein (Cys) modified gold electrode (Au/Cys) in 0.1 M H_2SO_4 was investigated by cyclic voltammetry (CV) and by square wave voltammetry (SWV). Effect of scan rate on the CVs of SC standard was performed in order to examine the mode of transport and irreversibility of process. SC as standard is determined by SWV in acid solution at Au electrode in a range: 10^{-3}, 10^{-2}, 0.1, 0.5, 1 µM and on Au/Cys in a range: 10^{-3}, 10^{-2}, 0.05, 0.1 µM. The presence of Cys causes two-time larger peak currents and shifting of the incipient potential of the SC oxidation to 0.1 V in negative direction. In investigated range of concentration of SC standard in acid solution on modified and unmodified Au electrodes SWV method have excellent linear regression coefficient with value 0.997 promoting SWV for reliable determination of SC.

Keywords

Sildenafil citrate standard; cystein modified electrode; sensitivity; quantitative analysis.

Introduction

Sildenafil citrate (SC) is chemically designated as 1-[[3-(6,7- dihydro-1-methyl-7-oxo-3-propyl-1H-pyrazolo[4,3-d]pyrimidin-5-yl)-4-ethoxyphenyl]sulfonyl]-4-methylopiperazine citrate. SC is the active ingredient of one of the widely used pharmaceutical formulations of Viagra. Studied initially for its use in treatment of hypertension and angina, Viagra was very efficient for the treatment of erectile dysfunction. Nonmedical use of SC has increased over the years [1,2]. SC treats and recovery of extreme tiredness after a long flight [3]. The most common adverse effects of SC use included nasal congestion, impaired vision (blurriness, loss of peripheral vision, photophobia) and headache. Serious adverse effects include severe low blood pressure, heart attack, stroke, increased intraocular pressure, sudden hearing loss [4].

Many various methods for determination of sildenafil citrate in pharmaceutical preparations and biological samples have been described. The most frequently used method for determination of SC is high performance liquid chromatography [5-7]. Other reported methods for confirmation of SC in pharmaceutical preparations or biological fluids are optical methods such as UV-VIS spectrophotometric methods [8], NMR spectroscopy [9] or Electrospray tandem mass spectrometry (ESI-MS-Ms) spectrophotometry [10] and electroanalytical methods [11-15]. Among electrochemical methods different electrodes and voltammetric techniques were used. The SC determination at pH 2.0 was performed by SWV and adsorptive stripping techniques at hanging mercury drop electrode [16]. At glassy carbon electrodes (GC), CV and SWV were applied in determination of SC in the mixture with paracetamol and carvedilol [17] and in biological and pharmaceutical formulations [14]. The cyclic and linear sweep voltammetric methods as well as differential pulse voltammetry (DPV) and SWV at GC were applied for oxidative determination of SC in solutions containing 30 % (v/v) acetonitrile at different pHs [18]. By SWV at Pb film modified GC a new method for determination of SC is developed [19].

Different electrodes were used for electrochemical examination of SC. For example, electroanalytical methods were applied at boron-doped diamond and at diamond paste electrodes [12,20]. Delolo *et al.* used GC modified with a chitosan-supported ruthenium film in order to prepare sensor for SC [13].

The aim of this work is to examine the electrochemical behavior of SC at Au and Au/Cys in 0.1 M H_2SO_4 by CV and SWV. Scan rate studies were carried out to assess whether the process on Au and Au/Cys was under diffusion or adsorption-controlled. Linear dependency of peak currents from concentrations is established using SWV in order to investigate the sensitivity of the electrodes. Also, the linear dependency was constructed as a calibration curve and tested for quantitative determination of SC.

Experimental

Sildenafil citrate, provided by Hemofarm A.D. Stada, was used as SC standard and as content of Sildena® tablets (pharmaceutical formulation) with excipiences: lactose monohydrate, cellulose, microcrystalline, hydroxypropylcellulose, croscarmellose sodium, sodium stearyl fumarate, silica colloidal anhydrous, Opadry II Blue, Opadry fx silver. L-cysteine and H_2SO_4 were purchased from Sigma Aldrich.

For CV and SWV measurements, PGZ 402 Volta Lab (Radiometer Analytical, Lyon, France) was used and the three-electrode electrochemical cell. Polycrystalline gold (surface area 0.5 cm^2) which served as the working electrode, was polished with diamond paste, cleaned with a mixture of 18 MΩ cm deionized water and sulfuric acid and further cleaned with 18 MΩ cm deionized water in an ultrasonic bath. A gold wire was used as the counter electrode and a saturated calomel electrode (SCE) as the reference electrode. All potentials are given *vs.* SCE. The electrolytes were deoxygenated by purging with nitrogen.

Electrode modification and stock solutions were prepared according to [21]. All the solutions used were prepared with high purity water (Millipore, 18 MΩ cm resistivity).

Results and discussion

The electrochemical behavior of SC on Au and Au/Cys electrode was studied by cyclic voltammetry (CV) and its determination in pharmaceutical formulations was carried out by square wave voltammetry (SWV). The CV of SC standard on gold electrode in 0.1 M H_2SO_4 alongside the

voltammetric response of Au electrode in blank solution (dot line) is presented in Fig. 1. In the presence of SC, the CV was changed so that current increase occurs in the region of oxide formation. It can be said that highly developed gold oxide on surface is necessary as a catalyst for the beginning of the SC electrooxidation reaction.

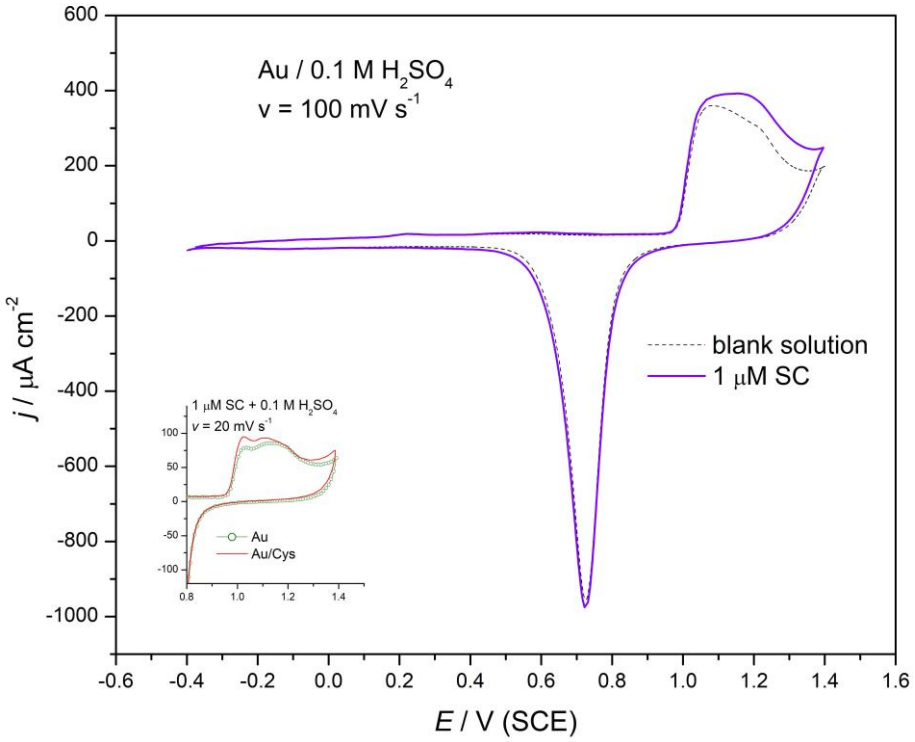

Figure 1. *CV of Au electrode using 0.1 M H_2SO_4 (dot line) and after the addition of 1 μM SC standard (full line), scan rate: 100 mV s^{-1}. Inset: CV of 1 μM SC standard on Au (dash line) and Au/Cys (full line) electrode, scan rate: 20 mV s^{-1}.*

In order to improve the activity, the electrode was modified with cysteine as was previously described [21]. In the inset of Fig. 1 it is show that in the presence of Cys the electrode becomes more active for the electrochemical oxidation of SC. The improved activity of the modified electrode in 0.1 M H_2SO_4 could be due to the increase of the electrode surface area according to the observed differences in morphology of the gold surface modified with Cys as was confirmed by optical microscope [21]. The role of Cys can also be explained by the mechanism proposed by Ozkan *et al.* for the electrochemical oxidation of SC on a GC electrode in an aqueous solution containing 30 % (v/v) acetonitrile [18]. The authors indicated that acid–base equilibrium precedes the electrooxidation of the piperazine moiety at pH 5.5. Cys is chemisorbed on an Au surface through the thiol group, while its amino and carboxylic groups remain available to interact with SC. As suggested by Wang and Du [22], it seems that Cys act as a mediator of the electrode reaction and as an electron-transferring accelerator. Possible mechanism of interaction between SC and Au/Cys is presented in detailed in [21], explaining the observed reactivity for SC electrooxidation.

Sildenafil citrate was used as SC standard and as content of Sildena® tablets (pharmaceutical formulation) containing excipients. Figure 2 show CVs of SC standard and SC in pharmaceutical formulation on modified and unmodified Au electrode. Overlap of CVs confirm that excipients are electrochemically inactive and did not affect the SC electrooxidation.

Furthermore, effect of the scan rate on the CVs of SC standard was studied on Au/Cys electrode as is presented in Fig. 3. Scan rate studies were carried out to assess whether the process on modified gold electrode was under diffusion or adsorption-controlled.

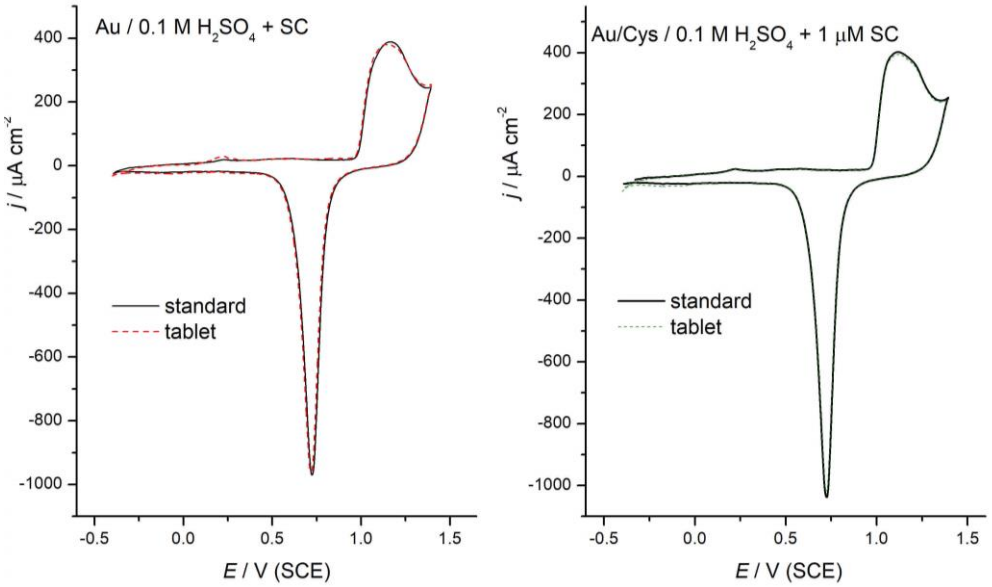

Figure 2. *CV of SC standard (full line) and SC tablet (dot line) on Au electrode (a), CV of SC standard (full line) and SC tablet (dot line) on Au/Cys electrode (b); 1 µM SC + 0.1 M H_2SO_4 scan rate: 100 mV s^{-1}.*

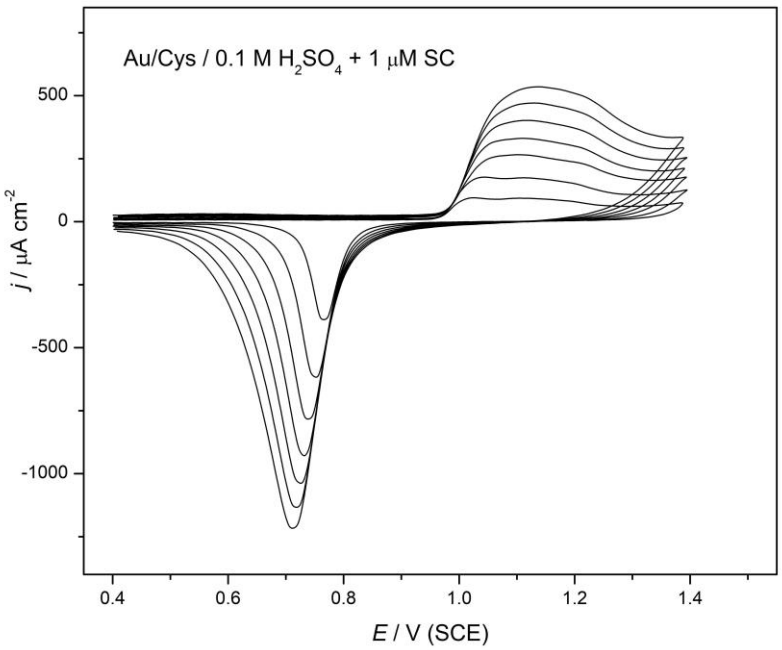

Figure 3. *CVs of SC standard on Au/Cys electrode for different scan rates 20-140 mV s^{-1}.*

Figure 4 demonstrates the dependency of peak current and peak potential from scan rates recorded in the range 20-140 mV s^{-1} (data are taken from Fig. 3). The peak current densities are linearly proportional to the scan rates suggesting adsorption-controlled electrode process (Fig. 4a). Furthermore, plot of logarithm of anodic peak current *vs*. logarithm of scan rate gave a straight line with a slope of 0.89 close to the theoretical value of 1.0, which is expected for an ideal reaction for the adsorption-controlled electrode process [23]. The peak potential was also dependent on scan rate. The plot of E_p versus log *v* was linear suggesting that it is irreversible electrode process (Fig. 4b). Nevertheless, close inspection of the dependency of peak potential from scan rates in backward direction indicates partially deviation from linearity for slower scan rates suggesting the interference of some reaction intermediates on the electrode process. The same experiments were performed on Au electrode exhibiting the same conclusion about the mode of

transport and irreversibility of process. Effect of scan rate on SC at GC [14,18] and at the hanging mercury dropping electrode[24] demonstrate also the adsorption-controlled process.

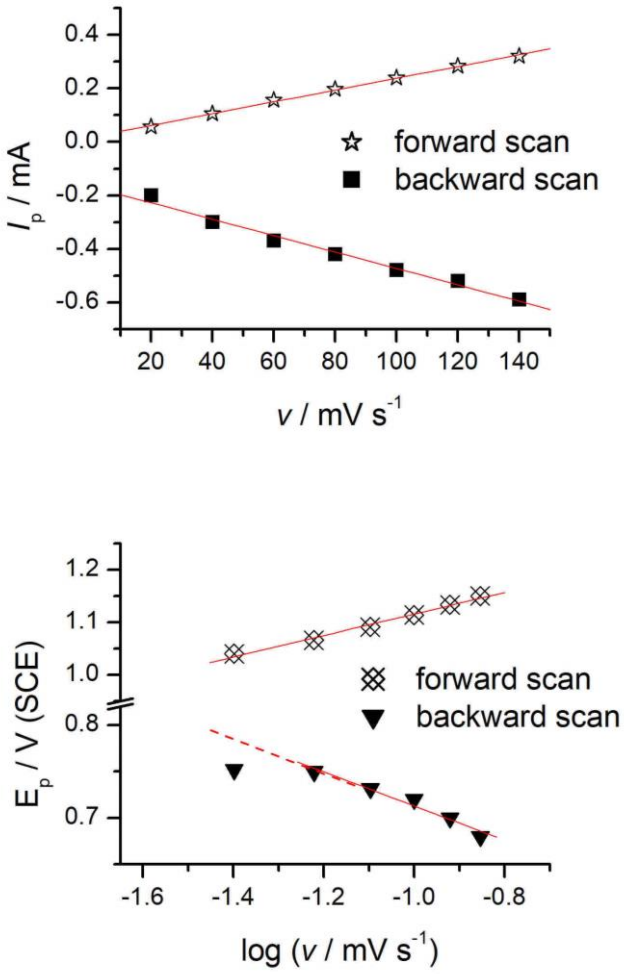

Figure 4. *Electrochemical behavior of SC standard on Au/Cys electrode for scan rates 20-140 mV s^{-1}, presented as dependence of peak current* vs. v *(a) and peak potential vs. log of scan rates (b).*

Apart from apparent increase in the voltammetric response caused using higher scan rates, the significant improvement in sensitivity can be achieved by employing SWV method. In order to establish the optimal parameters in SWV pulse size, scan rate and accumulation time were varied. The peak current appeared with maximum values for an accumulation potential of -400 mV while the accumulation time of 60 s enables electrode surface saturation. With increasing scan rate, the peak current increases also but the peak becomes less sharp and poorly defined. Higher peak current was observed by increasing the pulse size, but the background current also increases. The peak current increases linearly with step size up to 5 mV. Thus, the best defined voltammetric signal for the determination of SC was recorded under the conditions: step size 5 mV, pulse size 25 mV, scan rate 10 mV s^{-1}, accumulation time 60 s at - 400 mV.

SC standard is determined by SWV in 0.1 M H_2SO_4 at Au in a range: 10^{-3}, 10^{-2}, 0.1, 0.5, 1 µM as is shown in Fig. 5. It can be notice that the selected concentrations of SC standard start to oxidize with the beginning of oxide formation on gold electrode. SW voltammograms recorded at Au electrode for increasing amount of SC standard concentrations showed a linear increase of anodic peak currents with the concentration (inset of Fig. 5) with an excellent correlation coefficient (R = 0.997). Obviously, the linear dependency can be used as a calibration curve for quantitative determination, providing a convenient way for quantitative analysis.

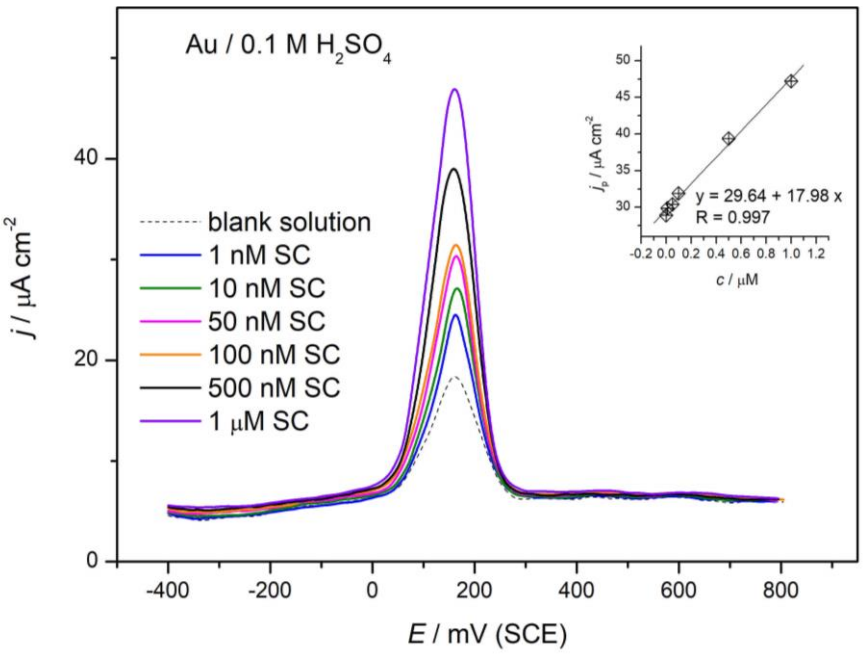

Figure 5. *SW voltammograms of SC standard (10^{-3}, 10^{-2}, 5×10^{-2}, 10^{-1}, 5×10^{-1}, 1.0 μM) on Au electrode using 0.1 M H_2SO_4. Step size 5 mV, pulse size 25 mV and scan rate 10 mV s^{-1}, accumulation time 60 s at -400 mV. Inset: the linear dependency of anodic peak currents vs. concentration of SC standard.*

SC standard is determined by SWV at Au/Cys electrode in a range: 10^{-3}, 10^{-2}, 0.05, 0.1 μM as is shown in Fig. 6. The currents increase with increasing the concentration of SC standard, shifting the peak current towards less positive value. A linear increase of anodic peak currents with the concentration with an excellent correlation coefficient (R = 0.997) is observed and presented in inset of Fig. 6. Comparing the equations for linear dependency of peak currents from concentrations it can be notice that higher slope of calibration curve is obtained on Au/Cys electrode indicating the higher sensitivity of SW voltammetry for concentration detection. Nevertheless, linear dependency can be obtained in extensive concentration range on Au electrode regarding Au/Cys.

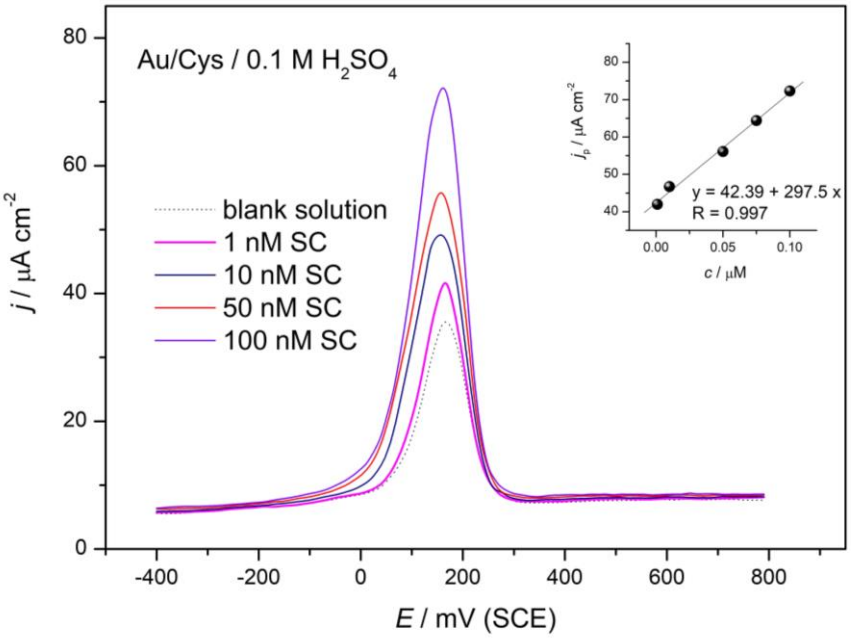

Figure 6. *SW voltammograms of SC standard (10^{-3}, 10^{-2}, 5×10^{-2}, 10^{-1}, 5×10^{-1}, 1.0 μM) on Au electrode using 0.1 M H_2SO_4. Step size 5 mV, pulse size 25 mV and scan rate 10 mV s^{-1}, accumulation time 60 s at -400 mV. Inset: the linear dependency of anodic peak currents* vs. *concentration of SC standard.*

Better insight in the obtained activity of Au and Au/Cys electrode in SC standard electrooxidation can be observed by overlapping of SW voltammograms for a chosen concentration, as is presented in Fig. 7. Comparing the results of SW voltammograms two times larger peak currents and 100 mV more negative incipient potential obtained on Au/Cys in regard to Au electrode can be noticed. It could be explained by possible oxidation mechanism and by different electrode surfaces morphology [21]. Concerning SW voltammogram of SC tablet on Au/Cys electrode, the same shape and peak position was obtained. Examination of the electrochemical behavior of various concentrations of SC tablet by SWV reveal excellent fitting in the calibration curve, as is presented in [**Error! Bookmark not defined.**]. Besides, unknown concentrations of SC tablet are confirmed by HPLC-UV method. It was highlighted that in contrast to HPLC-UV, electrochemical method is more sensitive and can be used for the measurements of very low concentrations of analyte.

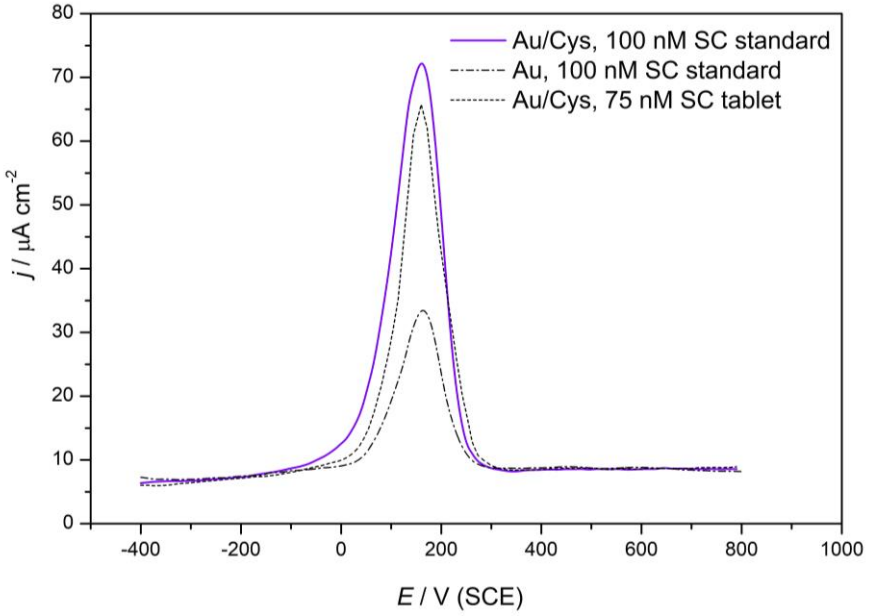

Figure 7. *SW voltammograms of 0.1 µM SC standard on Au and Au/Cys electrode and of 0.75[1] µM SC tablet using 0.1 M H_2SO_4. Step size 5 mV, pulse size 25 mV and scan rate 10 mV s^{-1}, accumulation time 60 s at -400 mV.*

Table 1 presents comparative characteristics of the quantitative determination of SC obtained with different electrochemical methods. The calibration curves provided reliable linear responses on a suitable range although with Au/Cys electrode linear concentration range was extent to a very low concentration (up to nanomoles per liter magnitude order).

Table 1. *Comparison of electrochemical methods for SC determination*

method	electrode	Linear range, M	LOD, M	reference
AdCSV	Bismuth film/GC	10^{-7}-10^{-6}	$1.8x10^{-8}$	[25]
potentiometry	Ppy/Cit/Graphite	$3.4x10^{-5}$-$1.7x10^{-3}$	$3x10^{-5}$	[26]
SWV	screen-printed GC	10^{-6}-$1.4x10^{-5}$	$5.5x10^{-8}$	[14]
SWV	Au/Cys	10^{-9}-10^{-7}	$1.04x10^{-8}$	Present work

Conclusions

Investigation of electrochemical behavior of SC at Au electrode in acid solution reveal that highly developed gold oxide on surface is necessary as a catalyst for the beginning of the SC electrooxidation reaction. Effect of the scan rate on the CVs of SC standard was studied on Au/Cys and Au electrode suggesting adsorption-controlled electrode process since the peak current

densities are linearly proportional to the scan rates. Also, the peak potential was linear dependent on logarithm of scan rate suggesting that it is irreversible electrode process. SWV measurements indicate wider range of currents *vs.* concentrations linearity on Au electrode compared to modified electrode. Nevertheless, with Au/Cys an enlargement of SC anodic currents and shift of the incipient potential of 0.1 V to the negative direction is noticed. In investigated ranges of SC standard concentration in acid solution on modified and unmodified Au electrodes SWV method have excellent linear regression coefficient with value 0.997 and SWV can be used for reliable determination of SC.

***Acknowledgements**: This work was financially supported by the Ministry of Education, Science and Technological Development of the Republic of Serbia, Contract No. H-172060 and H-172013.*

Reference

[1] M. M. Goldenberg, *Clinical Therapeutics* **20** (1998) 1033-1048.
[2] K.M. Smith, F. Romanelli, *Journal of the American Pharmaceutical Association* **45** (2003) 63-72.
[3] P. V. Agostino, S. A. Plano, D. A. Golombek, *Proceedings of the National Academy of Sciences of the United States of America* **104** (2007) 9834-9839.
[4] Viagra U.S. Physician Prescribing Information and U.S. Patient Product Information for Health Care Professionals (PDF). September 2015 (Available online: http://www.pfizer.com).
[5] I. Baranowska, P. Markowski, J. Baranowski, J. Rycaj, *Chemia Analityczna* **52** (2007) 645-671.
[6] C. K. Jeong, H. Y. Lee, M. S. Jang, W. B. Kim, H. S. Lee, *Journal of Chromatography B* **752** (2001) 141-149.
[7] Y.Wang, J.Wang, Y.Cui, J. Fawcett, J. Gu, *Journal of Chromatography B* **828** (2005) 118-121.
[8] A. A. Bunaciu, R. M. El Nashar, H. Y. Aboul-Enein, *Analytical Letters* **44** (2011) 2085-2093.
[9] I. Wawer, M. Pisklak, Z. Chilmonczyk, *Journal of Pharmaceutical and Biomedical Analysis* **38** (2005) 865-870.
[10] M. E. Abdel-Hamid, *Journal of Liquid Chromatography & Related Technologies* **29** (2006) 591-603.
[11] S.-C. Balasoiu, R.-I. Stefan-van Stadena, J. Frederick van Stadena, R.-M. Ionc, G.-L. Radub, H. Y. Aboul-Enein, *Electrochimica Acta* **58** (2011) 290- 295.
[12] E. F. Batista, E. R. Sartori, R. A. Medeiros, R. C. Rocha-Filho, O. Fatibello-Filho, *Analytical Letters* **43** (2010) 1046-1054.
[13] F. G. Delolo, C. Rodrigues, M. Martins da Silva, L. R. Dinelli, F. N. Delling, J. Zukerman-Schpector, A. A. Batista, *Journal of the Brazilian Chemical Society* **25** (2014) 550-559.
[14] R. A. Farghali, R. A. Ahmed, *Internal Journal of Electrochemical Science* **7** (2012) 13008 – 13019.
[15] A. I. Gopalan, K. P. Lee, S. Komathi, *Biosensors and Bioelectronics* **26** (2011) 3018-3022.
[16] J. J. Berzas, J. Rodriguez, G. Castañeda, M. J. Villaseñor, *Analytica Chimica Acta* **417** (2000) 143-148.
[17] I. Baranowska, M. Koper, P. Markowski, *Chemia Analityczna* **53** (2008) 967-981.
[18] S. A. Ozkan, B. Uslu, P. Zuman, *Analytica Chimica Acta* **501** (2004) 227-233.
[19] K. Tyszczuk, M. Korolczuk, *Bioelectrochemistry* **78** (2010) 113-117.
[20] R.-I.S. van Staden, J.F. van Staden, H.Y. Aboul-Enein, *Journal of Solid State Electrochemistry* **14** (2010) 997-1000.
[21] J. Lović, N. Trišović, J. Antanasijević, N. D. Nikolić, S. Stevanović, D. Mijin, D. Vuković, A. Mladenović, S. Petrović, M. Avramov Ivić, *Journal of Electroanalytical Chemistry* **782** (2016) 103-107.
[22] S. Wang, D. Du, *Sensors* **2** (2002) 41-49.
[23] D. K. Gosser, *Cyclic Voltammetry: Simulation and Analysis of Reaction Mechanisms*, VCH, New York, 1993, p. 43.
[24] J. Rodrıguez, J. J. Berzas, G. Castañeda, N. Rodriguez, *Talanta* **62** (2004) 427-432.
[25] H. Sopha, S. B. Hocevara, B. Pihlar, B. Ogorevc, Elec*trochimica Acta* **60** (2012) 274-277.
[26] L. M. Ochiai, E. H. Bindewald, P. Mengarda, L. H. Marcolino-Junior, M. F. Bergamini, *Journal of Applied Polymer Science* **133** (2016) 43762-43767.

J. Electrochem. Sci. Eng. **8(2)** (2018) 171-181; DOI: http://dx.doi.org/10.5599/jese.507

Open Access : : ISSN 1847-9286

www.jESE-online.org

Original scientific paper

A short introduction to digital simulations in electrochemistry: simulating the Cottrell experiment in NI LabVIEW

Soma Vesztergom

Eötvös Loránd University, Department of Physical Chemistry, Pázmány Péter sétány 1/A, 1117 Budapest, Hungary

E-mail: vesztergom@chem.elte.hu; Tel.: +36-20-461-2429

Received: February 9, 2018; Revised: March 28, 2018; Accepted: March 28, 2018

Abstract

A brief introduction to the use of digital simulations in electrochemistry is given by a detailed description of the simulation of Cottrell's experiment in the LabVIEW programming language. A step-by-step approach is followed and different simulation techniques (explicit and implicit Euler, Runge–Kutta and Crank–Nicolson methods) are applied. The applied techniques are introduced and discussed on the basis of Padé approximants. The paper might be found useful by undergraduate and graduate students familiarizing themselves with the digital simulation of electrochemical problems, as well as by university lecturers involved with the teaching of theoretical electrochemistry.

Keywords

Explicit and implicit Euler method; Runge–Kutta methods; Crank–Nicolson method; Padé approximants.

Introduction

At the 6th Regional Symposium on Electrochemistry for South-East Europe (6th RSE–SEE), I gave a keynote lecture [1] on the kinetics of hydrogen evolution in mildly acidic solutions. Under these chemical conditions — at low to moderate pH values ($1 < pH < 4$) — the reduction of H^+ ions and that of water molecules both give a significant contribution to the measured cathodic current. In my talk, I presented digital simulations (and a simplified analytical model) that can describe polarization curves measured on rotating disk electrodes immersed into mildly acidic solutions.

Results presented in my talk at the 6th RSE–SEE were published [2] just a few weeks before the conference. Instead of further discussing these results, I chose to focus more in this paper on the applied method of digital simulation (DS).

DS presents a powerful tool that can be used for the qualitative understanding, as well as for the quantitative description of electrode processes. When carrying out DS, we create a numerical

model of the electrochemical system within a computer and allow this model to evolve according to a set of simple algebraic equations. These equations are derived from the physical laws that govern the electrochemical system under study. In effect, we carry out a simulation of the experiment with the aim to extract numeric representations of current, concentration profiles, potential transients, and so on [3]. The results of digital simulations can then be compared to measured quantities, so that the physical parameters of the system can be fine-tuned in subsequent simulations, until the measured data are reproduced at a desired accuracy.

DS thus allows the determination of kinetic parameters, such as charge transfer rates and diffusion coefficients, *etc*. DS can yield important quantitative information even for complex electrochemical systems where the often-complicated set of partial differential equations, describing the transformation and movement of material, can be solved in closed form with difficulty or not at all [3].

In this paper I give a very brief and practice-oriented introduction to digital simulations and their use in electrochemistry. Instead of reviewing the topic of digital simulations in detail — several good textbooks are dedicated to the subject and are recommended to the reader [3,4] — I choose a rather straightforward approach: that is, giving a step-by-step guide to the simulation of a simple electrochemical problem, that is known as Cottrell's experiment [5].

The paper is intended to be a starting point for undergraduate or graduate students, interested in digital simulations. Furthermore, the paper may also be found useful by university lecturers, as it contains a simpler than usual description and classification of different partial differential equation solving methods, based on Padé's approximants.

Experimental

Cottrell's experiment, first described in 1903 by F.G. Cottrell, is one of the oldest problems in electrochemistry that has a well-known analytical solution. The simulation of Cottrell's experiment is thus expedient, since the success of any simulation can directly be tested [6] by comparison to analytically obtained results.

In order to understand Cottrell's experiment, consider [7] a large planar electrode, of surface A, initially at rest, in contact with a semi-infinite layer of unstirred solution that contains some excess electrolyte and a small amount of a redox-active species R with a bulk concentration of c^{∞}. At the instant $t = 0$, the electrode potential is suddenly changed to a value at which the species R is oxidized to some product O in the one-electron reduction

$$R \rightarrow O + e^- \tag{1}$$

and the concentration of R, close to the electrode surface, is brought to essentially zero.

In this experiment, the reaction rate (and thus, the current) is determined by the rate of transport at which the species R is resupplied at the electrode surface. That is, the partial differential equation governing the system is that describing Fick's law,

$$\frac{\partial c}{\partial t} = D\frac{\partial^2 c}{\partial x^2}. \tag{2}$$

Equation (2) is a second-order partial differential equation where c denotes the concentration and D the diffusion coefficient of the species R, while x and t denote the space and time variables, respectively. To obtain an analytical solution of Equation (2), we take two boundary conditions into consideration: *i.)* that the concentration of the species R is zero at the electrode surface at any $t > 0$ and *ii.)* that the concentration at infinite distance from the electrode surface never changes and remains equal to c^{∞}

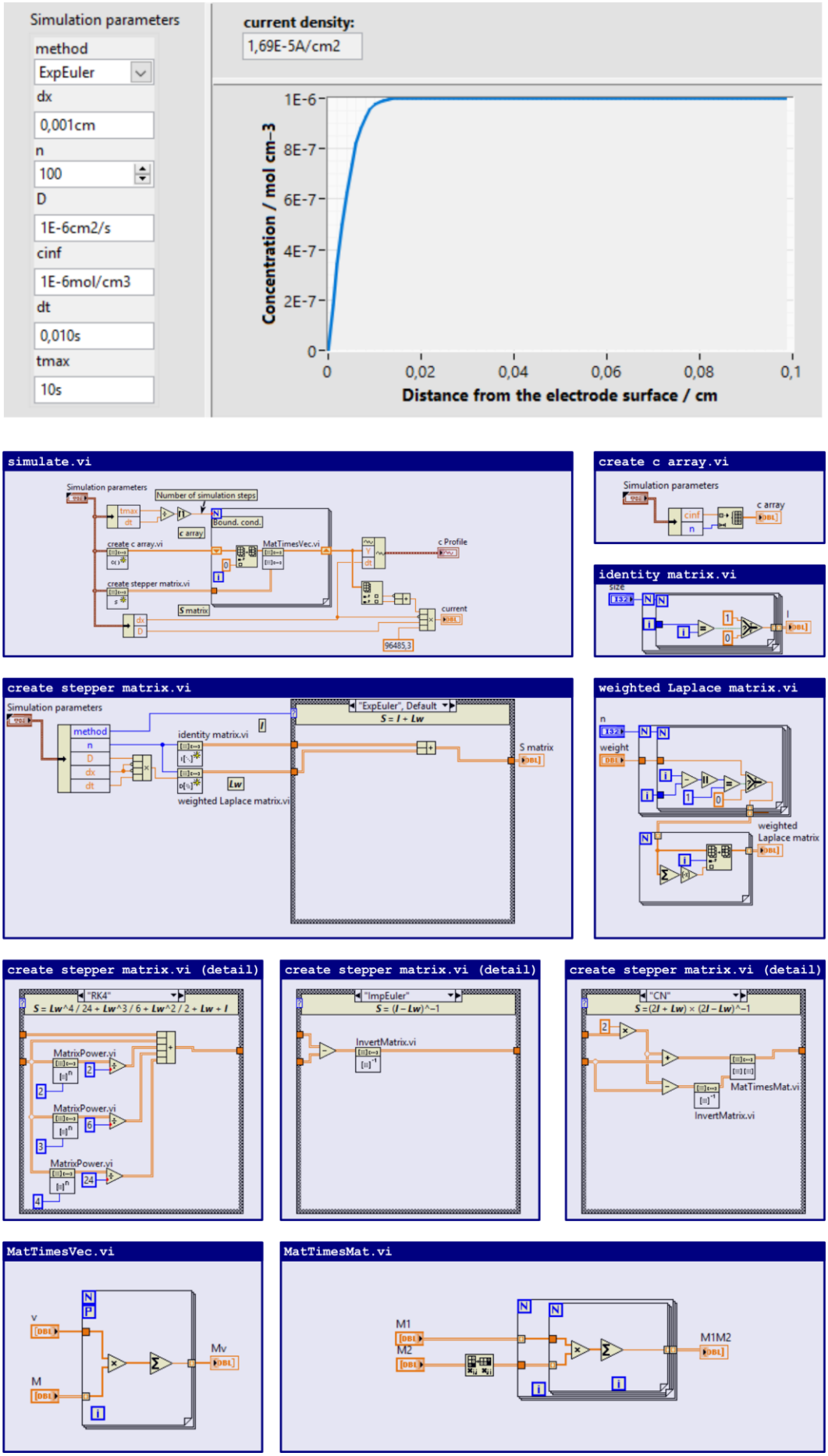

Figure 1. *The graphical user interface (top) of a simple LabVIEW program that simulates Cottrell's experiment. Snippets (code details) are shown in the blue boxes; see the text for explanation*

Taking the above boundary conditions into consideration leads to the solution:

$$c(x,t) = c^{\infty}\,\mathrm{erf}\left(\frac{x}{\sqrt{4Dt}}\right), \tag{3}$$

where the function erf(*z*) denotes Gauss's error function, defined by the integral:

$$\mathrm{erf}(z) = \frac{2}{\sqrt{\pi}}\int_0^z \exp\left(-u^2\right)\mathrm{d}u.$$

The current density $j(t)$, passing the electrode surface at any time $t > 0$ is thus:

$$j(t) = F\,D\lim_{x\to 0}\left(\frac{\partial}{\partial x}c(x,t)\right) = F\,c^{\infty}\sqrt{\frac{D}{\pi t}}, \tag{4}$$

where F = 96485.3 C mol^{-1} is Faraday's constant.

Equation (3) makes it straightforward to calculate the concentration of species R at any given time $t > 0$ at a distance x measured from the electrode surface; while from Equation (4), the well-known Cottrell equation, the current density can be calculated for any $t > 0$. These analytical formulae will be used below for testing the results of digital simulations.

Simulation approaches

LabVIEW, developed by National Instruments, is an easy-to-use, interactive, graphical programming language that helps users write sophisticated programs and applications in a short amount of time without needing a computer science degree [8]. The popularity of LabVIEW continuously increases amongst students and scientific researchers, also in electrochemistry, mostly due to its versatility in measurement automation. However, LabVIEW also provides simple means for digital simulations and I therefore chose to present the basics of simulation algorithms in this programming language. Figure 1, discussed extensively below, shows the user interface of a program written for the simulation of Cottrell's experiment, as well as some details of the code. The main routine is that shown by the `simulate.vi` snippet.

In most digital simulation schemes, we consider the electrolyte solution in terms of discrete and small (Δx wide) volume elements, as illustrated by Figure 2. When we apply this approach to the simulation of Cottrell's experiment in NI LabVIEW, we create a 1-dimensional array of concentrations, containing n entries, which we denote by ***c***. At the start of the simulation process, all entries of the array ***c*** will be set equal to c^{∞} (the bulk concentration). The initialization of the ***c*** array in LabVIEW is shown by the `create c array.vi` snippet of Figure 1.

Each i entry of the array ***c*** (the index i can take values between 0 and $n-1$ in LabVIEW) corresponds to the concentration of the species R at a certain distance from the electrode surface, as shown by Figure 2. For accurate simulations, the Δx width of the control volumes must be small, thus to include a big enough space in the simulations, a sufficiently high number of the control volumes is required. (See Table 1 for numeric parameter values, used for the simulations presented in this paper.)

When carrying out digital simulations, we iteratively modify the entries of the ***c*** array, as shown by the `simulate.vi` snippet of Figure 1. Each iteration step represents a Δt time-step in which we replace the first element of ***c*** with zero (thereby realizing the boundary condition of the experiment) and then multiply the array (vector) ***c*** with a so-called stepper matrix, denoted here by ***S***. As the iteration proceeds, we continuously "update" the ***c*** array, which at the end of the iteration will turn to be a discrete representation of the concentration profile, corresponding to the time t.

Table 1. *Simulation parameters.*

Symbol	Meaning	Value
Δx	width of the control volumes	0.001 cm
n	number of the control volumes	100
D	diffusion coefficient	10^{-6} cm^2 s^{-1}
c^{∞}	bulk concentration	10^{-6} mol cm^{-3}
Δt	time-step	varied between 1 ms and 5 s

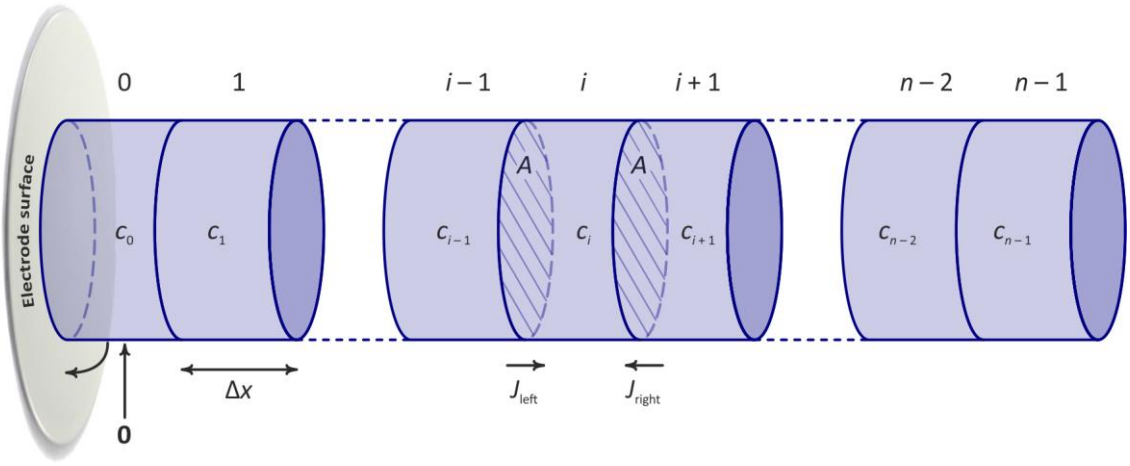

Figure 2. *Scheme for the digital simulation of Cottrell's experiment*

The multiplication of the ***c*** array with the stepper matrix ***S*** in each iteration step mimics the role of transport in the simulation process, thus the construction of the stepper matrix has a deep impact on both the accuracy and the speed of the simulation.

To understand the role of the stepper matrix ***S*** in digital simulations, let us consider Figure 2, and assume that in each control volume shown, the concentration values are different. Let us then try to estimate the changes of concentration in the control volume marked by the index i during a small time-step Δt. Fick's first law of diffusion allows us to calculate the J_{left} and J_{right} fluxes of material from the left-hand ($i-1$) and the right-hand ($i+1$) neighbours, directed to the i^{th} control volume as:

$$J_{\text{left}} = \frac{1}{A}\frac{\Delta n_{\text{left}}}{\Delta t} = -D\frac{c_i - c_{i-1}}{\Delta x} \tag{5a}$$

and

$$J_{\text{right}} = \frac{1}{A}\frac{\Delta n_{\text{right}}}{\Delta t} = -D\frac{c_i - c_{i+1}}{\Delta x}, \tag{5b}$$

where Δn_{left} and Δn_{right} denote the amount of substance arriving to the i^{th} cell from its left and right neighbours, respectively. In each time-step Δt, the amount of substance that enters the i^{th} cell is $\Delta n = \Delta n_{\text{left}} + \Delta n_{\text{right}}$, and taking into consideration the volume of the cell ($A\Delta x$), this results in a

$$\frac{\Delta c_i}{\Delta t} = \frac{\left(J_{\text{left}} + J_{\text{right}}\right)A}{A\Delta x} = D\frac{c_{i-1} - 2c_i + c_{i+1}}{\Delta x^2} \tag{6}$$

concentration change in the i^{th} control volume. We note that the fraction on the right-hand side of Equation (6) approximates the second spatial derivative of the concentration profile, and that Equation (6) is in fact a discretized version, with respect to both space and time, of Equation (2), Fick's second law.

Equation (6) dictates that in a time-step of Δt duration, the change of concentration in the i^{th} control volume depends on the concentrations in the i^{th}, $(i-1)^{\text{th}}$ and $(i+1)^{\text{th}}$ control volumes, as well as on the model parameters D, Δx and Δt. Equation (6) may be re-written in the form of a matrix-vector equation as:

$$\frac{\Delta \boldsymbol{c}}{\Delta t} = \frac{D}{\Delta x^2} \boldsymbol{L}\,\boldsymbol{c} \tag{7}$$

by defining the so-called Laplacian matrix $\boldsymbol{L}$, an $n \times n$ matrix as:

$$L_{i,k} = \begin{cases} 1 & \text{if } i = k \pm 1 \\ -\deg(i) & \text{if } i = k \\ 0 & \text{otherwise} \end{cases}, \tag{8}$$

where $\deg(i)$ is the number of neighbours of the i^{th} control volume. For the simulation scheme shown in Figure 2, the Laplacian — a negative semi-definite matrix — takes the following form:

$$\boldsymbol{L} = \begin{pmatrix} -1 & 1 & 0 & 0 & 0 & 0 \\ 1 & -2 & 1 & 0 & 0 & 0 \\ 0 & 1 & \ddots & \ddots & 0 & 0 \\ 0 & 0 & \ddots & \ddots & 1 & 0 \\ 0 & 0 & 0 & 1 & -2 & 1 \\ 0 & 0 & 0 & 0 & 1 & -1 \end{pmatrix}. \tag{9}$$

Note that Equation (7) contains a finite difference (with respect to time) on its left-hand side, approximating a time derivative. For infinitesimally small time-steps, Equation (7) may be re-written as:

$$\frac{\mathrm{d}\boldsymbol{c}}{\mathrm{d}t} = \frac{D}{\Delta x^2} \boldsymbol{L}\,\boldsymbol{c}, \tag{10}$$

which is a differential equation for the vector $\boldsymbol{c}$. Assuming that the concentration vector $\boldsymbol{c}^{(k)}$ is known at any k^{th} step of the simulation, the $\boldsymbol{c}^{(k+1)}$ vector in the next step, Δt time later, could be calculated by solving Equation (10) in the form:

$$\boldsymbol{c}^{(k+1)} = \exp\left(\boldsymbol{L}_{\text{w}}\right) \boldsymbol{c}^{(k)}, \tag{11}$$

where $\boldsymbol{L}_{\text{w}}$ denotes the so-called weighted Laplacian, defined as:

$$\boldsymbol{L}_{\text{w}} = \frac{D\,\Delta t}{\Delta x^2} \boldsymbol{L}. \tag{12}$$

The LabVIEW code used for the calculation of the weighted Laplacian is shown by the `weighted Laplace matrix.vi` snippet of Figure 1.

As can be seen in Equation (11), the "ideal" choice for the stepper matrix $\boldsymbol{S}$ we introduced before would be that $\boldsymbol{S} = \exp\left(\boldsymbol{L}_{\text{w}}\right)$; the multiplication of the concentration vector $\boldsymbol{c}$ in each simulation step with this matrix could model the time evolution of the system, leaving the resolution of spatial discretization the only factor that limits the accuracy of calculations.

The problem is, however, that the exponential of the weighted Laplacian is not known and can only be approximated. One feasible way of approximating the exponential of a matrix is to truncate its Taylor series at a given order; another, more accurate way, is to use its Padé approximant [9].

It is this latter approach which I will follow here, as many digital simulation techniques — such as the explicit and implicit Euler, the Runge–Kutta and the Crank–Nicolson methods [4] — may be interpreted as techniques relying on the use of different Padé approximants.

Given a function $f(x)$ and two integers $m \geq 0$ and $n \geq 0$, the Padé approximant of the function $f(x)$ of order $[m/n]$ is the rational function:

$$\mathrm{R}(x) = \frac{\sum_{j=0}^{m} a_j x^j}{\sum_{j=0}^{n} b_j x^j}, \tag{13}$$

which agrees with $f(x)$ to the highest possible order, which amounts to:

$$f(0) = \mathrm{R}(0) \tag{14a}$$

$$f'(0) = \mathrm{R}'(0) \tag{14b}$$

$$f''(0) = \mathrm{R}''(0) \tag{14c}$$

$$f^{(m+n)}(0) = \mathrm{R}^{(m+n)}(0) \tag{14d}$$

Equation (14) is a system of Equations, by solving which the parameters a_j and b_j of Equation (13) can be determined up to one degree of freedom; it is usually assumed that $b_0 = 1$.

In what follows, I will use $\mathrm{P}_{m,n}(x)$ to note the Padé approximant of the exponential function $\exp(x)$. Exact expressions for $\mathrm{P}_{m,n}(x)$ are tabulated in Table 2 for different values of m and n. Some Padé approximants to the exponential function are plotted, together with $\exp(x)$, in Figure 3 to show the "goodness" of these approximations.

Padé approximants, when applied to matrices instead of scalars, form the basis of many known simulation techniques, as will be discussed below.

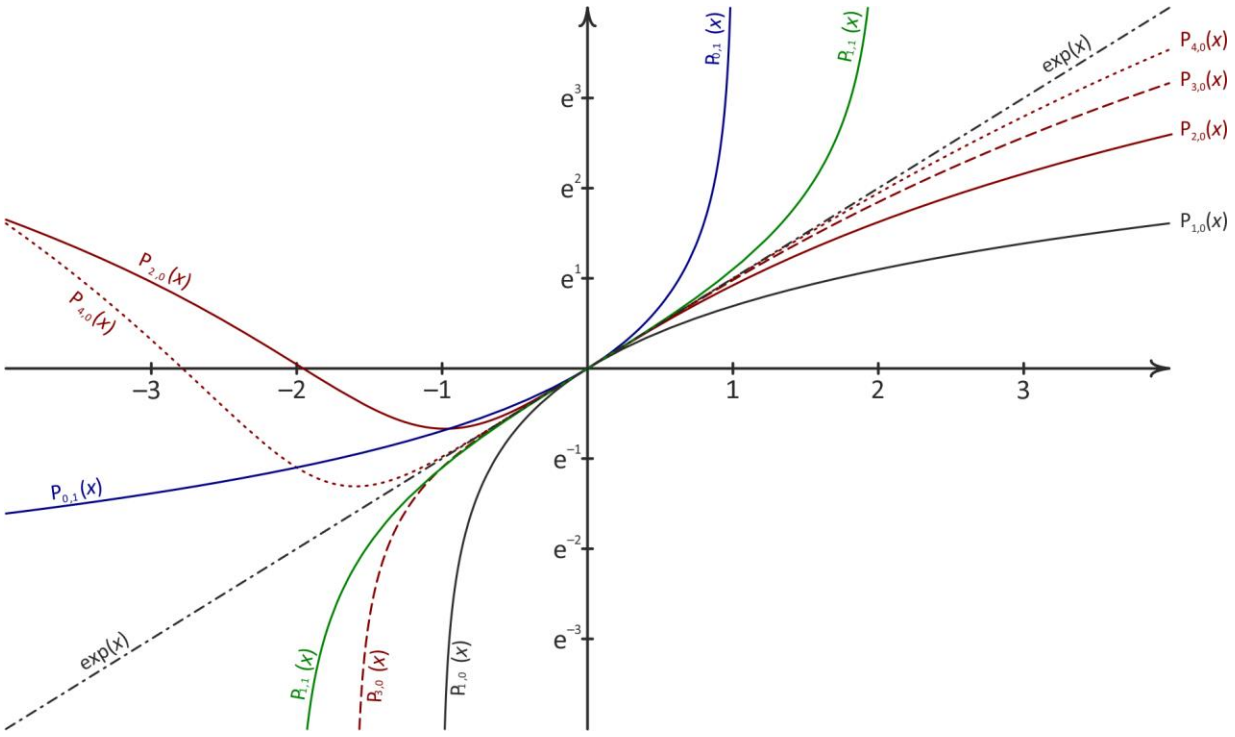

Figure 3. *Some Padé approximants* $\mathrm{P}_{m,n}(x)$ *of the function exp(x)*

Table 2. *Some Padé approximants* $P_{m,n}(x)$ *of the function exp(x)*

$m \backslash n$	**0**	**1**	**2**	**3**
0	1	$\frac{1}{-x+1}$	$\frac{1}{\frac{1}{2}x^2-x+1}$	$\frac{1}{-\frac{1}{6}x^3+\frac{1}{2}x^2-x+1}$
1	$x+1$	$\frac{\frac{1}{2}x+1}{-\frac{1}{2}x+1}$	$\frac{\frac{1}{3}x+1}{\frac{1}{6}x^2-\frac{2}{3}x+1}$	$\frac{\frac{1}{4}x+1}{-\frac{1}{24}x^3+\frac{1}{4}x^2-\frac{3}{4}x+1}$
2	$\frac{1}{2}x^2+x+1$	$\frac{\frac{1}{6}x^2+\frac{2}{3}x+1}{-\frac{1}{3}x+1}$	$\frac{\frac{1}{12}x^2+\frac{1}{2}x+1}{\frac{1}{12}x^2-\frac{1}{2}x+1}$	$\frac{\frac{1}{20}x^2+\frac{2}{5}x+1}{-\frac{1}{60}x^3+\frac{3}{20}x^2-\frac{3}{5}x+1}$
3	$\frac{1}{6}x^3+\frac{1}{2}x^2+x+1$	$\frac{\frac{1}{24}x^3+\frac{1}{4}x^2+\frac{3}{4}x+1}{-\frac{1}{4}x+1}$	$\frac{\frac{1}{60}x^3+\frac{3}{20}x^2+\frac{3}{5}x+1}{\frac{1}{20}x^2-\frac{2}{5}x+1}$	$\frac{\frac{1}{120}x^3+\frac{1}{10}x^2+\frac{1}{2}x+1}{-\frac{1}{120}x^3+\frac{1}{10}x^2-\frac{1}{2}x+1}$
4	$\frac{1}{24}x^4+\frac{1}{6}x^3+\frac{1}{2}x^2+x+1$	$\frac{\frac{1}{120}x^4+\frac{1}{15}x^3+\frac{3}{10}x^2+\frac{4}{5}x+1}{-\frac{1}{5}x+1}$	$\frac{\frac{1}{360}x^4+\frac{1}{30}x^3+\frac{1}{5}x^2+\frac{2}{3}x+1}{\frac{1}{30}x^2-\frac{1}{3}x+1}$	$\frac{\frac{1}{840}x^4+\frac{2}{105}x^3+\frac{1}{7}x^2+\frac{4}{7}x+1}{-\frac{1}{210}x^3+\frac{1}{14}x^2-\frac{3}{7}x+1}$

The $P_{1,0}$ *(explicit Euler) method*

The explicit Euler method is the most straightforward one applied for the solution of partial differential equations. It is based on the $P_{1,0}(x)$ Padé approximation

$$\exp\left(\boldsymbol{L}_{\mathrm{w}}\right) \approx \boldsymbol{I} + \boldsymbol{L}_{\mathrm{w}} = \boldsymbol{S}, \tag{15}$$

where $\boldsymbol{I}$ is the $n \times n$ identity matrix (see the `identity matrix.vi` snippet of Figure 1). When plugged into Equation (11), it yields that

$$\boldsymbol{c}^{(k+1)} = \left(\boldsymbol{I} + \boldsymbol{L}_{\mathrm{w}}\right)\boldsymbol{c}^{(k)}. \tag{16}$$

The construction of the stepper matrix $\boldsymbol{S}$, used for simulations based on the explicit Euler method, is shown in the `create stepper matrix.vi` snippet of Figure 1.

Note that as $\Delta\boldsymbol{c} = \boldsymbol{c}^{(k+1)} - \boldsymbol{c}^{(k)}$, Equation (16) can also be directly obtained by rearranging Equation (10). The explicit Euler method can thus be interpreted as approximating the differential $\mathrm{d}\boldsymbol{c}/\mathrm{d}t$ in Equation (10) with the finite difference $\Delta\boldsymbol{c}/\Delta t$. Consequently, the explicit Euler method, a linear approximation, may only yield accurate results when a small enough time-step Δt is used. In-fact, when $\Delta t > \Delta x^2/2D$, the explicit Euler method fails to converge and gives erroneous results, as will be discussed later.

The $P_{2,0}$*,* $P_{3,0}$ *and* $P_{4,0}$ *(Runge–Kutta) methods*

The overall error of the explicit Euler method can be decreased by taking higher order terms into consideration. This can be achieved by using the $P_{2,0}$, $P_{3,0}$ and $P_{4,0}$ Padé approximants, which are in-fact Taylor series expansions of different orders to the exponential function. This forms the basis of the so-called 2nd, 3rd and 4th order Runge–Kutta methods [10]. While the explicit Euler method could be interpreted as a technique that takes the slope (but not the curvature) of the concentration *vs.* time dependence into account, Runge–Kutta methods aim to correct this error.

When applying Runge–Kutta methods, the stepper matrix $\boldsymbol{S}$ is constructed as

$$\exp\left(\boldsymbol{L}_{\mathrm{w}}\right) \approx \boldsymbol{I} + \boldsymbol{L}_{\mathrm{w}} + \frac{1}{2}\boldsymbol{L}_{\mathrm{w}}^2 = \boldsymbol{S} \qquad \text{for the 2nd order,} \tag{17}$$

$$\exp\left(\boldsymbol{L}_{\mathrm{w}}\right) \approx \boldsymbol{I} + \boldsymbol{L}_{\mathrm{w}} + \frac{1}{2}\boldsymbol{L}_{\mathrm{w}}^2 + \frac{1}{6}\boldsymbol{L}_{\mathrm{w}}^3 = \boldsymbol{S} \qquad \text{for the 3rd order,} \tag{18}$$

and

$$\exp\left(\boldsymbol{L}_{\mathrm{w}}\right) \approx \boldsymbol{I} + \boldsymbol{L}_{\mathrm{w}} + \frac{1}{2}\boldsymbol{L}_{\mathrm{w}}^2 + \frac{1}{6}\boldsymbol{L}_{\mathrm{w}}^3 + \frac{1}{24}\boldsymbol{L}_{\mathrm{w}}^4 = \boldsymbol{S} \qquad \text{for the 4th order method.} \tag{19}$$

The construction of the stepper matrix ***S***, used for simulations based on the 4th order Runge–Kutta method, is shown by the respective `create stepper matrix.vi (detail)` snippets of Figure 1. Note that — similarly to the Euler method discussed above — Runge–Kutta methods are still *explicit*; that is, in each iteration step, they calculate the state of a system at a later time from the state of the system at the current time.

The $P_{0,1}$ (implicit Euler) method

The implicit (also called backward [4]) Euler method differs largely from explicit methods. The method is *implicit*, meaning that it finds a solution for the state of the system at a later time by solving an equation that involves both the current state of the system and the later (yet unknown) state. The stepper matrix used by the implicit Euler method, as also shown by the respective `create stepper matrix.vi (detail)` snippet of Figure 1, is

$$\exp\left(\boldsymbol{L}_{\mathrm{w}}\right) \approx (\boldsymbol{I} - \boldsymbol{L}_{\mathrm{w}})^{-1} = \boldsymbol{S} \tag{20}$$

Note that due to the implicit nature of the method, the creation of the stepper matrix involves matrix inversion. This clearly requires some extra computation, yet implicit methods can become very useful for the solution of stiff problems where explicit methods require the application of impractically small Δ*t* values. As implicit methods are numerically stable, they can be applied with larger time-steps, and as usually the matrix inversion in Equation (20) has to be carried out only once (at the beginning of the iteration), implicit methods still require small computation times.

The $P_{1,1}$ (Crank–Nicolson) method

The method named after Crank and Nicolson [11] was developed for the numerical solution of partial differential equations, but it lies on the basis of the trapezium method of solving ordinary differential equations. The method is *semi-implicit* and is unconditionally stable; although when applied for stiff systems with large time-steps it may still be prone to spurious (decaying) oscillations. The stepper matrix used by the Crank–Nicolson method, as also shown by the respective `create stepper matrix.vi (detail)` snippet of Figure 1, is

$$\exp\left(\boldsymbol{L}_{\mathrm{w}}\right) \approx (\boldsymbol{I} + \tfrac{1}{2}\boldsymbol{L}_{\mathrm{w}})(\boldsymbol{I} - \tfrac{1}{2}\boldsymbol{L}_{\mathrm{w}})^{-1} = \boldsymbol{S}. \tag{21}$$

Comparison of the different simulation methods

As expected, applying Padé approximations of different order for the construction of the stepper matrix ***S*** yields solutions that also behave differently. The efficiency of the methods was tested by simulating concentration profiles corresponding to *t* = 5 s, using the parameter values of Table 1 and Δ*t* values ranging between 1 ms and 5 s. Each simulated concentration profile was compared to the theoretically expected one, Equation (3), and the square-root of the mean squared deviation was plotted as a function of the used time-step in Figure 4.

Figure 4 clearly shows a major difference with respect to the stability of fully explicit (explicit Euler and Runge–Kutta) and implicit (implicit Euler and Crank–Nicolson) methods; at about $\Delta t > \Delta x^2/2D$, all explicit methods begin to diverge (see also Figure 5). Compared to the explicit Euler, the 2nd order Runge–Kutta method brings a significant improvement of the error; this improvement is less significant for the 3rd and 4th order Runge–Kutta methods.

The stability of the implicit Euler and the Crank–Nicolson methods is better (see also Figure 5), although the error of these methods is also significant at larger time-steps.

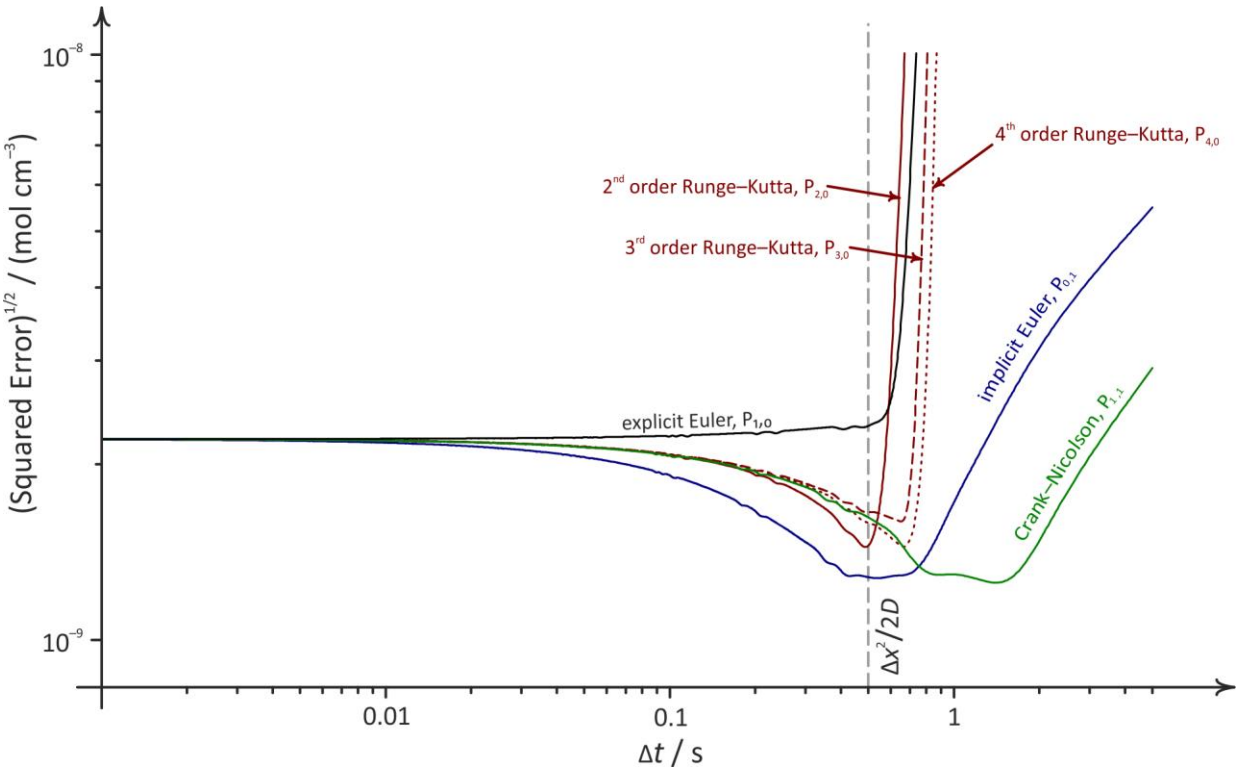

Figure 4. *The error of six different digital simulation methods, as a function of the applied time-step. Other simulation parameters are tabulated in Table 1*

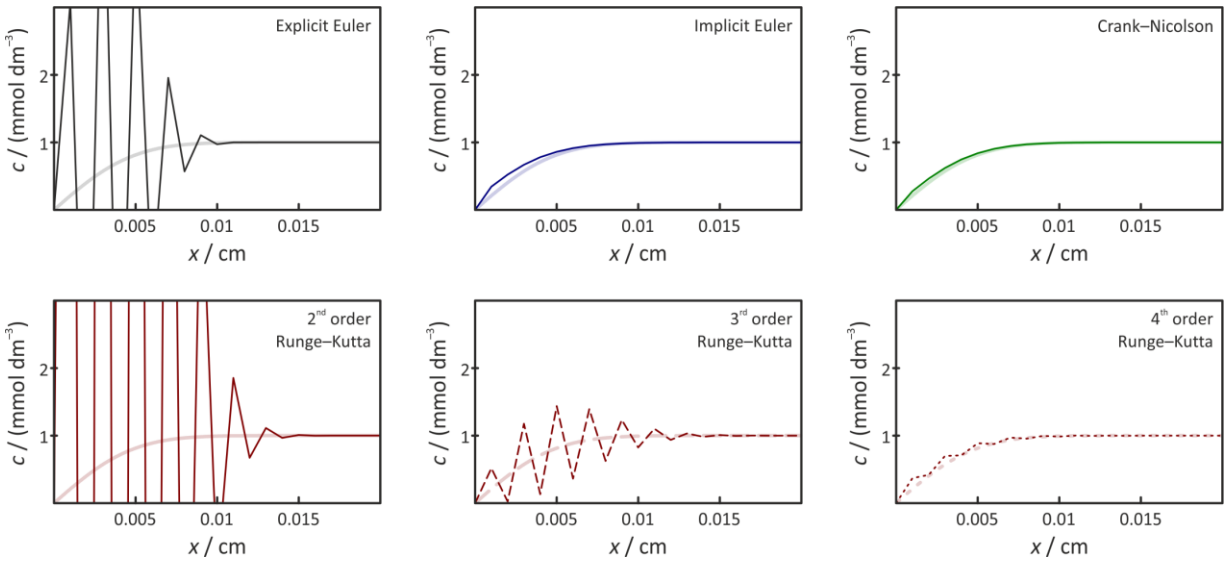

Figure 5. *Concentration profiles simulated using six different methods for t = 7 s, using a relatively large time-step (Δt = 700 ms). Faded thick curves show theoretical profiles, as calculated from Equation (3). For the values of other simulation parameters, see Table 1*

Summary

In this paper I attempted to describe numerical methods used for the digital simulation of a rather simple, however instructive electrochemical problem, Cotrell's experiment. The same techniques may also be used — by modifying the near-electrode boundary condition — for the simulation of more complicated electrochemical experiments, such as cyclic voltammetry. The described simulation strategies may also be extended to take into account homogeneous reactions [12], or effects related to ohmic drop [13,14]. The further discussion of more complicated systems is, however, beyond the scope of this paper: my only intention here was to

give a starting point for undergraduate or graduate students who decided to familiarize themselves with digital simulations. Accordingly, I attempted to describe basic numerical procedures in a simpler than usual manner, following a classification scheme based on Padé's approximants. Readers interested in the topic of digital simulation in more detail are referred to other sources [3,4].

Acknowledgements: *I would like to thank my dear friends and colleagues Éva Valkó and Norbert Barankai for their valuable suggestions with which they aided this work. Financial support from the National Research, Development and Innovation Office of Hungary (under grant PD124079) is gratefully acknowledged.*

References

[1] S. Vesztergom, V. Grozovski, G. G. Láng, P. Broekmann, 6th Regional Symposium on Electrochemistry for South-East Europe, On the Electrolysis of Dilute Solutions of Strong Acids, Balatonkenese, Hungary, 2017, p. 103 (KN103).
[2] V. Grozovski, S. Vesztergom, G. G. Láng, P. Broekmann, *Journal of the Electrochemical Society* **164** (2017) 3171–3178.
[3] A. J. Bard, L. R. Faulkner, *Electrochemical Methods: Fundamentals and Applications*, John Wiley & Sons, New York, 2001, pp. 785–807.
[4] D. Britz, J. Strutwolf, *Digital Simulation in Electrochemistry*, 4th Edition, Springer, Berlin, 2016.
[5] F. G. Cottrell, Zeitschrift für physikalische Chemie **42** (1903) 385–431.
[6] E. Kätelhön, R.G. Compton, *Analyst* **140** (2015) 2592–2598.
[7] A. J. Bard, Gy. Inzelt, F. Scholz (Eds), *Electrochemical Dictionary*, Springer, Berlin, 2008, p. 163.
[8] G. W. Johnson, R. Jennings, *LabVIEW Graphical Programming*, 4th Edition, McGraw-Hill, New York, 2006.
[9] G. A. Baker, P. Graves-Morris, *Padé Approximants*, Cambridge University Press, Cambridge, 1996.
[10] K. A. Atkinson, *An Introduction to Numerical Analysis,* John Wiley & Sons, New York, 1989.
[11] J. Crank, P. Nicolson, Proceedings of the Cambridge Philosophical Society, **43** (1947) 50–67.
[12] S. Vesztergom, N. Barankai, N. Kovács, M. Ujvári, Th. Wandlowski, G.G. Láng, *Acta Chimica Slovenica* **61** (2014) 223–232.
[13] S. Vesztergom, N. Barankai, N. Kovács, M. Ujvári, H. Siegenthaler, P. Broekmann, G. G. Láng, *Journal of Solid State Electrochemistry* **20** (2016) 3165–3177.
[14] S. Vesztergom, N. Barankai, N. Kovács, M. Ujvári, H. Siegenthaler, P. Broekmann, G. G. Láng, *Electrochemistry Communications* **68** (2016) 54–58.

J. Electrochem. Sci. Eng. **8(2)** (2018) 183-195; DOI: http://dx.doi.org/10.5599/jese.536

Open Access : : ISSN 1847-9286
www.jESE-online.org

Original scientific paper

Single and multi-frequency impedance characterization of symmetric activated carbon single capacitor cells

Suzana Sopčić[1], Davor Antonić[1], Zoran Mandić[1], Krešimir Kvastek[2], Višnja Horvat-Radošević[2,✉]

[1]*University of Zagreb, Faculty of Engineering and Technology, Department of Electrochemistry, Marulićev trg 19, 10000 Zagreb, Croatia*
[2]*Ruđer Bošković Institute, Bijenička c. 54, 10000 Zagreb, Croatia*

✉Corresponding author - E-mail: vhorvat@irb.hr

Received: April 9, 2018; Revised: May 4, 2018; Accepted: May 10, 2018

Abstract

Electrochemical impedance spectroscopy (EIS) technique is used for characterization of single cell symmetric capacitors having different mass loadings of activated carbon (AC). Relevant values of charge storage capacitance (C_T) and internal resistance (ESR) were evaluated by the single frequency and multi-frequency analyses of measured impedance spectra. Curve fittings were based on the non-ideal R-C model that takes into account the parasitic inductance, contributions from electrode materials/contacts and the effects of AC porosity. Higher C_T and lower ESR values were obtained not only for the cell with higher mass of AC, but also using the single vs. multi-frequency approach. Lower C_T and higher values of ESR that are generally obtained using the multi-frequency method and curve fittings should be related to the not ideal capacitive response of porous AC material and too high frequency chosen in applying the single frequency analysis

Keywords

Double-layer capacitor; electrical response; porous electrodes; storage capacitance, internal resistance

Introduction

Electrochemical capacitors/supercapacitors are high power energy storage devices composed basically from two electrodes built-up from an active material put on current collectors and immersed in a liquid ionic conductor (electrolyte) [1–8]. In these devices, energy is stored reversibly or quasy-reversibly by either ion adsorption at the electrode/electrolyte interfacial regions (electrochemical double layer capacitors – EDLC), or ion adsorption combined with some fast surface redox (faradaic) reaction (supercapacitors – SC). Various types of EDLC/SCs were already derived, including symmetric and asymmetric devices. Symmetric EDLC/SCs utilize the same

electrode material (usually carbon) for both electrodes, while asymmetric types use different materials for electrodes, including a battery-like electrode in asymmetric hybrid devices [8–10].

Charging/discharging of an EDLC/SC device containing purely capacitive electrodes is initiated by on/off switching of *dc* voltage (*V*) and related to separation of charges in double-layers formed at each electrode in contact with electrolyte. The scheme of the single cell of an EDLC/SC device containing two separated and equal material electrodes (positive and negative) in an electrolyte is presented in Figure 1.

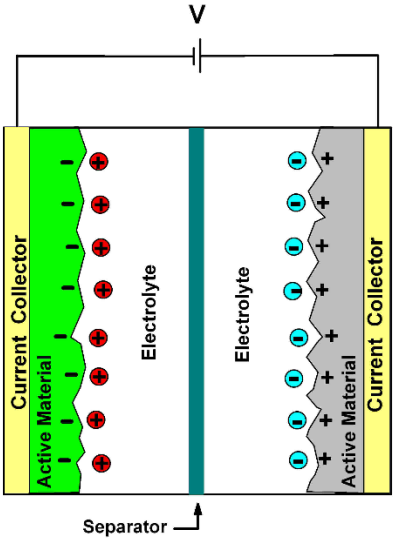

Figure 1. *Schematic presentation of symmetric single cell capacitor*

The charge storage ability (or capacity) of a capacitive cell is determined by the positive and negative electrode capacitance values (C_+ and C_-), what makes the total capacitance (C_T) of cell to be defined as:

$$1/C_T = 1/C_- + 1/C_+ \quad (1)$$

The overall performance of an EDLC/SC capacitive device is usually described in terms of the rated charge storage capacitance (C_T), *dc* voltage (*V*) and electrical series resistance (ESR) values. ESR comprised the internal resistance of a device including resistances of current collectors, electrodes, electrolyte, separator and all contact regions formed in between. The values of these three characteristic parameters (C_T, *V* and ESR) are essential for estimation of important comparative topics for EDLC/SC energy devices such as specific energy ($E_{sp} = C_T V^2/2n$) and the maximal deliverable specific power ($P_{sp(max)} = V^2/4n \times$ESR). Here, *n* denotes the normalization parameter such as mass, volume, surface area, etc. Use of high surface area porous carbon materials, conductive electrolytes with high breakdown potential and highly ion-permeable separators have strongly been recommended for attaining beneficially high C_T and *V* and low ESR values, *i.e.* high energy and high power EDLC/SC devices [11–19].

Determinations of C_T and ESR values for devices containing new materials and also upon conventional testing of EDLC/SCs have usually been performed using different electrochemical techniques. The most commonly used are cyclic voltammetry (CV) and galvanostatic charging/discharging measurements [16–26]. By using CV experiments, C_T values are estimated from the constant (capacitive) currents measured within a voltage window (*V*) at low scan rates. By use of charging/discharging experiments performed at some constant current value within the voltage window (*V*), C_T values are obtained from measured *V vs*. time linear plots. At the same time, the voltage drop appearing at the initiation of the constant current discharge is commonly used for determination of ESR.

Electrochemical impedance spectroscopy (EIS) [25,27–29] is another electrochemical technique that can provide both, C_T and ESR values at various voltage (V) levels of a capacitive device that should be in causal, stable, linear and time invariant conditions. EIS is usually performed by applying a small sinusoidal (current or potential) perturbing signal and measuring impedance (Z) or admittance (Y) vector as a function of the angular frequency (ω). Impedance vector is defined as:

$$Z = 1/Y = |Z| e^{i\varphi} = Z' + iZ'' \quad (2)$$

In eq. (2), $|Z|$ and φ are magnitude and phase angle of impedance vector, while Z' and Z'' are the real and imaginary parts in its complex number presentation. Impedances of capacitive devices are commonly measured in the linear frequency ($f = \omega/2\pi$) range between 50 kHz – 0.01 Hz.

Impedance spectra of EDLC/SC capacitive systems have generally been presented as Nyquist (Z'' *vs*. Z') [11,12,17-19,21,23,24,26,28,30–42], Bode ($\log|Z|$ and φ *vs.* $\log\omega$) [19,24,26,30,31,33, 38,42] and complex capacitance ($Y/i\omega = C$) plots. In this last case, complex capacitance spectra can be presented as C'' *vs*. C' and/or C'' and C' *vs.* $\log\omega$ ($\log f$) plots [12,18,31,33,34,37,40,42].

In applying of either single frequency or multi-frequency EIS method for characterization of capacitive devices, ESR and C_T values are usually obtained using the one time (lumped) constant R–C model [1,2,6,28,37] for a capacitive device, having the impedance/frequency response defined as:

$$Z(\omega) = \text{ESR} + 1/i\omega C_T \quad (3)$$

According to eq. (3), a capacitive device will behave as a pure resistor at high and pure capacitor at low frequencies, with some transition region in between. The product of ESR and C_T determines the time constant capacitor value, ESR × C_T = τ_c. This time constant characterizes the rate of a capacitor charging up to about 63 % of its final capacity (or about 37% of its depletion on discharging) and is important merit in comparing EDLC/SC devices.

ESR and C_T values can be estimated directly from measured impedance values at high (ESR = $Z'_{(\omega\to\infty)}$) and low ($C_T = -1/\omega Z''_{(\omega\to 0)}$) frequencies, respectively. The other way of identifying ESR and C_T parameters is the curve fitting procedure. This procedure is usually made by assigning the impedance function defined by eq. (3) across the entire range of measured frequencies, where all departures can easily be detected through the least square approach.

Departure from eq. (3) has usually been noticed through appearance of inductive impedance (having positive imaginary part) at the highest frequencies [11,17,21,24,35,36,41] and another one impedance showing characteristic –45° phase angle in the transition region between pure resistive and pure capacitive impedance responses [2,18,24,31–36,38–41]. Whereas inductive impedance response has usually been observed for low impedance (highly capacitive) systems, the characteristic –45° phase angle impedance response is almost always noticed in impedance spectra of capacitive devices with highly porous electrodes. Therefore, this impedance was usually ascribed to a distributed electrode structure, reactivity and/or porosity effects [2,35,40]. All these observations changed the ideal R–C model described by eq. (3) to the one which takes into account the parasitic inductance and the effects of electrode porosity according to the following relation [11,18,24,35,36,41,43,44]:

$$Z(\omega) = Z_L(\omega) + R_{HF} + Z_s(\omega) \quad (4)$$

Eq. (4) shows that the total impedance of a non-ideal capacitive device is composed from three impedances, *i.e*. inductive impedance (Z_L), high frequency resistance (R_{HF}) and pore impedance (Z_s). Frequency response of an inductive impedance is defined as $Z_L(\omega) = i\omega L$, where L is inductance that is measurable at high frequencies as $L = Z''/\omega$ [21,24,43]. Frequency response of Z_s, however, is more complex as it should describe the frequency dependence of a capacitance generated at pore walls,

as well as ionic resistance distributed within electrode pores. In order to account for −45° phase angle at high-to-medium frequencies that is followed by pure capacitive response at lower frequencies, various models of $Z_s(\omega)$ have already been recommended in the literature. Some of these models include either a pure capacitor in series with two or more parallel RC combinations [24,36,41,43,44], or the vertical ladder network [45], both mimicking different time constants in the pores. The most frequently, however, the concept based on the De Levie's theory of porous and rough electrodes [46] has been applied by which $Z_s(i\omega)$ is ascribed to the impedance/frequency response of a single rail *RC* transmission line element (TLE) [2,29,35,36,39,43,44,47].

Whereas C_T value is beneficially increased by using highly porous carbon as electrode material, appearance of an additional resistance distributed within the pores is generally considered detrimental. This is because any additional resistance would increase internal resistance, ESR = $R_{HF} + R_s(\omega)$ [31−33] and make the high-frequency resistance $R_{HF} = Z'_{(\omega\to\infty)}$ in eq. (4) to be only a part of ESR.

For some capacitive cells, however, a semicircle impedance response has additionally been noticed at higher frequencies, *i.e.* between R_{HF} and characteristic −45° and/or vertical shape of $Z_s(\omega)$ [18,23,32,33,39,40,43]. This impedance loop has increased ESR by another resistance component and shifted the capacitive response to smaller frequencies [32,33]. Some between many explanations for such impedance response were ascribed to the charge transfer of possible pseudo-capacitive reaction, formation of a passive layer at current collectors, formation of the interfacial region between current collector and electrode material or even pure dielectric polarization effects of the bulk solution [18,32,44]. In spite of diverse interpretation, a semicircle in impedance spectra of capacitive devices can simply be accounted for by a resistor-capacitor (*RC*) combination, defining its impedance/frequency response as $Z_{RC}(\omega)=R_{RC}/(1+i\omega R_{RC}C_{RC})$ [32,39,40,45]. Thereby, eq. (4) that has already been defined as the sum of three impedances becomes enlarged by inclusion of $Z_{RC}(\omega)$ impedance according to:

$$Z(\omega)= Z_L(\omega) + R_{HF} + Z_{RC}(\omega) + Z_s(\omega) \quad (5)$$

Impedance spectra defined by eq. (5) is composed of four characteristic frequency regions and described by six impedance parameters (L, R_{HF}, R_{RC}, C_{RC}, R_s and C_s) that all can be determined by the curve fitting procedure. In these conditions, $C_T = C_s$ and ESR = $R_{HF} + R_{RC} + R_s(\omega)$. In using the single frequency method, however, just contributions of different resistance components to ESR are the reason why ESR should inevitably be defined at lower frequencies [17,19] and why ESR = Z' at f = 1 kHz has been recommended for determination of ESR of technical capacitor devices using the single frequency EIS method [22,27].

Hereinafter, impedance characterization of the single cell (−)AC//AC(+) capacitors, prepared within realization of the ESU-CAP project of the Croatian National Foundation will be elaborated. Single and multi-frequency analyses will be performed and several approaches to analyze impedance data will be applied. The final results concerning total storage capacity (C_T) and internal resistance values (ESR) will be compared and discussed.

Experimental

Preparation of single cell AC//AC capacitors

The electrodes for AC//AC single cell capacitors were prepared from a slurry of the activated carbon (AC), carbon black and polyvinylidene difluoride (PVDF). The pre-determined weights of the slurry were coated onto Al foils pieces of 2 cm^2, dried and hot-pressed, forming electrodes with 6.5

and 20.5 mg of active material. The single cell capacitor assembly was performed within a high purity argon filled glove-box. Glass-fiber was inserted as a separator between two electrodes and solution of 0.25 mol dm^{-3} tetraethylammonium tetrafluoroborate ($TEABF_4$) in acetonitrile (ACN) served as the electrolyte. The capacitors containing electrodes with 3.2 and 10.2 mg cm^{-2} of the total active material were denoted as AC-1 and AC-2, respectively. All details of preparation were described previously [48].

Electrochemical impedance spectroscopy

Among various possibilities and equipment for impedance measurements [49,50], the present impedance measurements were performed using the Biologic Potentiostat SP-200 under EC-Lab software. The AC//AC cells were measured in discharged states at the open circuit voltage (V = 0.00 V) after being charged/discharged in 5 cycles between 0.00 and 2.7 V, at 4 mA cm^{-2} for AC-1 and 10 mA cm^{-2} for AC-2 cell, respectively. AC signal of $\pm$ 14 mV amplitude was applied and impedances at 10 measured points per decade were measured in the range of 1×10^6 to 0.01 Hz. Prior measurements the cells were left for about one hour to attain steady-state which was controlled by subsequent impedance measurements of each cell.

Impedance results were analyzed using the Zview (Scribner Ass.). The complex non-linear least squares (CNLS) program using a presumed model and modulus weighting mode was applied for impedance data fittings. C_T and ESR values obtained by the single frequency method served as initial values for the fitting procedure and all parameters were stated free in calculations. Statistical criteria for defining reasonable fits were small ($\leq 9\times10^{-4}$) standard deviation of the overall fit, χ^2:

$$\chi^2 = \sum_{k=1}^{N}\left[\frac{(Z'_{k(\exp)} - Z'_{k(cal)})^2 + (Z''_{k(\exp)} - Z''_{k(cal)})^2}{\left|Z_{k(cal)}\right|^2}\right] \quad (6)$$

In eq. (6), Z', Z'', k and N are real and imaginary impedances, particular frequency of measurement and total number of measured frequencies (data points), respectively. $|Z|$ is impedance magnitude, while "*exp*" and "*cal*" denote measured and calculated quantities. More details of corrections and statistical criteria for reasonable fits of impedance spectra are described elsewhere [51].

Results and discussion

Single-frequency impedance analysis

Figure 2 shows Nyquist (Z'' *vs*. Z') plots of two tested AC//AC single capacitor cells containing two near equal electrodes with different active material mass loadings (AC-1 and AC-2). Both Nyquist plots showed near vertical lines, indicating capacitive impedance responses for both AC//AC cells. Higher impedance observed for the electrode with less mass of active material (AC-1) is in agreement with literature data on similar AC//AC cells [31].

ESR values that according to eq. (3) should be obtained as $Z'_{(\omega\to\infty)}$, are at $f = 1\times10^5$ Hz estimated as 3.07 Ω for the AC-1 and 2.11 Ω the AC-2 cell. C_T values calculated using $C_T = -1/\omega Z''$ at the lowest measured frequency of 0.01 Hz were estimated to be 0.082 F and 0.297 F for the AC-1 and AC-2 cells, respectively. From these C_T values, specific capacitance per unit mass of one electrode, calculated using C_{sp} (F g^{-1}) = $4 \times C_T/m$, where m denotes the total mass of both electrodes [20], were 25 F/g for the AC-1 and 29 F/g for the AC-2 cell, respectively.

In another way of impedance data presentation, the concept of complex capacitance is applied due to the following capacitive impedance definition [27,29]:

$$Z(\omega) = [Y(\omega)]^{-1} = [\mathrm{i}\omega C(\omega)]^{-1} \quad (7a)$$

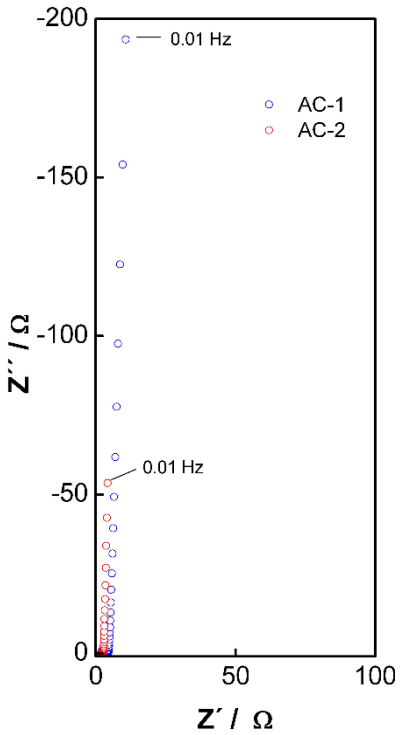

Figure 2. *Nyquist (Z'' vs. Z') plots of AC-1 and AC-2 capacitor cells*

The complex capacitance ($C = Y/i\omega$) has also vector properties and in terms of real and imaginary components can be defined as:

$$C(\omega) = C'(\omega) - iC''(\omega) \quad (7b)$$

For the pure R–C model defined by eq. (3), $C'(\omega)$ and $C''(\omega)$ are defined as:

$$C'(\omega) = -C_T/(1+\omega^2 C_T^2 ESR) \quad (8a)$$

$$C''(\omega) = \omega C_T ESR/(1+\omega^2 C_T^2 ESR) \quad (8b)$$

In this context, $C'(\omega)$ defined by eq. (8a) is a term related to the energy stored, while $C''(\omega)$ defined by eq. (8b) is a term related to the energy dissipation [18,23,31,34,38,42].

As shown in Fig. 3A, C'' *vs*. C' formed semicircle shapes for both AC//AC cells, tending to zero at high and C_T values at low frequencies. In accordance with eq. (8a), C_T values can be scanned directly from Fig. 3B as C' at $\omega \rightarrow 0$. Such determined values were 0.082 F and 0.295 F for AC-1 and AC-2 cells, respectively. As expected, these results are equal to that calculated above using Z'' value at 0.01 Hz.

Time constant (τ_c) values of 0.38 s and 0.77 s for AC-1 and AC-2 cells respectively, were estimated using the relation $\tau_c = (\omega_c)^{-1}$, where ω_c is the cutoff frequency at top of semicircles in Fig. 3A, or from maximums of C'' vs. log ω curve shown in Fig. 3C [18,23,33]. More commonly discussed and 2π times higher values of the relaxation time constants defined as $\tau_0 = (f_0)^{-1}$ [12,18,31,34,38,40,42] were estimated from the maximums *of* C'' *vs*. log f curves shown in Fig. 3C as 2.39 s and 4.83 s, respectively.

Both relaxation time values (τ_c and τ_0) can also be obtained from the phase Bode plots shown in Figure 4, by determining frequency values $f_0 = \omega_0/2\pi$ at which $Z' = Z''$ and $\varphi = -45°$ [30,33,40] as 0.42 and 0.21 Hz, respectively. Using the relation ESR= τ_0/C_T, ESR values were calculated as 4.63 Ω and 2.61 Ω, respectively. Somewhat higher ESR values than were estimated as Z' values at 1×10^5 Hz, suggested some extent of departure between measured data and eq. (3).

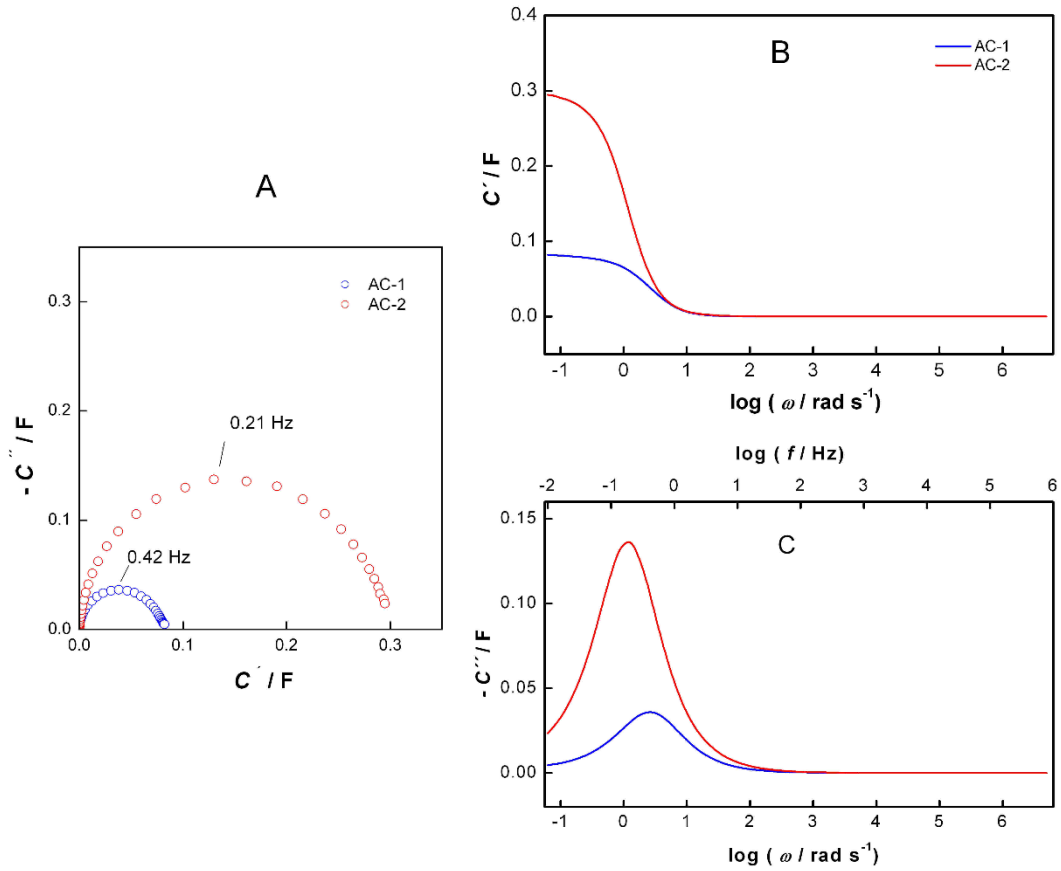

Figure 3. A) *C''* vs. *C',* B) *C'* vs. *log ω and* C) *C''* vs. *log ω and log f dependences of AC-1 and AC-2 capacitor cells*

Bode presentation of a pure *R–C* combination described by eq. (3) is expected to show a linear magnitude line with 0° phase angle at higher frequencies and a sloping linear line with –90° phase angle at lower frequencies. Certain discrepancies from this expectance can be noticed in Figure 4 as appearance of phase angles different than 0° (including positive values) at the highest frequencies of impedance spectra of both single capacitor cells.

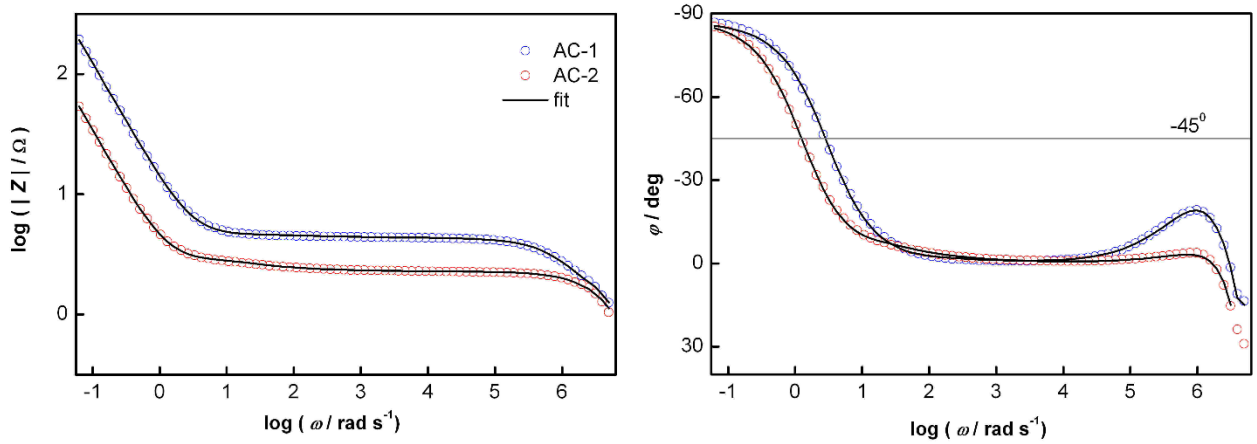

Figure 4. *Bode (log | Z | and φ vs. log ω) plots of AC-1 and AC-2 capacitor cells*

Figure 5 shows more precisely that almost ideal resistive and/or capacitive responses predicted by eq. (3) and labeled by dashed lines are obtained only within limited ranges of frequencies [21,24,28,30,35]. Vertical lines in Fig. 5A shows that frequency independent *Z'* values, suggesting

almost pure resistive cell responses, are for both AC//AC cells obtained within limited regions of high to medium frequencies.

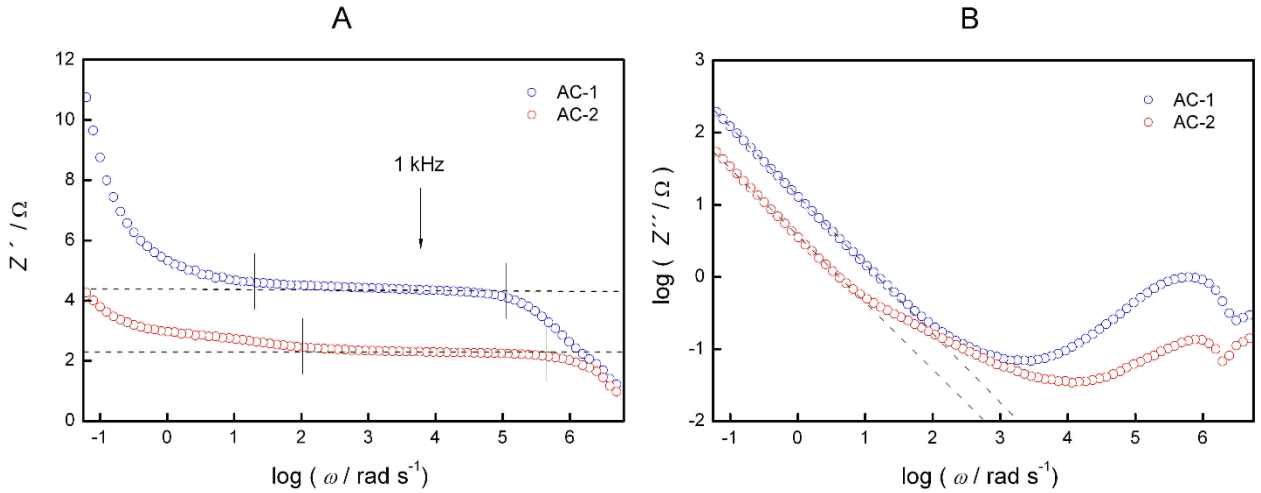

Figure 5. A) *Z' and* B) *log Z'' vs. log* ω *dependences of AC-1 and AC-2 capacitor cells*

The estimated ESR values at the recommended 1 kHz frequency [22,24,28,33] (denoted by the arrow in Figure 5A) are higher than those obtained as ESR = Z' at $f = 1\times10^5$ Hz and are equal to 4.36 Ω and 2.29 Ω for the AC-1 and AC-2 cells, respectively. Fig. 5B shows that the sloping linear lines, suggesting pure capacitive responses are observed at $\omega < 100$ (< 15 Hz) for the AC-1 cell and at $\omega <$ 10 (< 1.5 Hz) for the AC-2 cell, respectively. Pure capacitive responses squeezed to low frequency region have already been noticed in Figure 4.

All these results suggest that the *R*–*C* model described by eq. (3) is insufficient to present impedance of AC//AC capacitor cells but can be used as an approximation at rather low frequencies only. Therefore, in using the single frequency method, C_T should be estimated at the lowest measured frequency, while ESR values should not be estimated at too high frequencies [24,31–33,35].

Multi-frequency impedance analysis

As has already been stated in the Experimental part, impedance spectra of both AC//AC cells were measured over eight decades of frequencies (10^6–0.01 Hz). The results of CNLS fittings of eq. (3) to measured impedance spectra of both AC//AC cells are listed in Table 1. In spite of acceptable standard deviations obtained for C_T and ESR parameters values, huge χ^2 values have indicated the complete fail of the *R*–*C* model for both AC//AC capacitor cells. As is also shown in Table 1, similar has happened after use of the *R*–CPE model, where pure capacitive impedance in eq. (3) is replaced by impedance of the constant phase element (CPE) [26,40,43]. Impedance of CPE, Z_{CPE} (ω) defined by eq. (9) has usually been applied in order to account for some inclination from the ideal vertical capacitive line in Nyquist plots and phase angle different than –90° in Bode plots and ascribed to surface inhomogeneities of various kinds [26,40,43].

$$Z_{CPE}(\omega) = 1/T(i\omega)^{\alpha} \quad (9)$$

In eq. (9), Z_{CPE} (ω) is described by two frequency independent parameters (T and α), where T becomes pure capacitive parameter C for $\alpha = 1$. For $\alpha \neq 1$ and in the terms of eq. (3), the effective capacitance value, $(C_T)_c$, can be calculated using eq. (10) [52,53]:

$$(C_T)_c = T^{1/\alpha} \times \mathrm{ESR}^{(1-\alpha)/\alpha} \quad (10)$$

Table 1. *Results of CNLS fittings of C–R and R–CPE models to impedance spectra (10^6–0.01 Hz) of AC//AC capacitor cells.*

AC//AC	Model	ESR / Ω	C_T / F	T / Fs$^{\alpha-1}$	α	*$(C_T)_c$ / F	χ^2
AC-1	Eq. (3)	4.06±0.08	0.080±0.003	---	--	--	11
	Eqs. (3)+(9)	4.01±0.08	--	0.077±0.002	0.95±0.02	0.072	6.38
AC-2	Eq. (3)	2.33±0.03	0.286±0.008	---	--	--	8.23
	Eqs. (3)+(9)	2.28±0.03	---	0.261±0.008	0.92±0.01	0.249	3.57

*$(C_T)_c$ - calculated by eq. (10)

Fails of either the *R*–*C* model described by eq. (3) or *R*–CPE model described by eq. (3) combined with eq. (9) in the curve fittings of impedance data measured at frequencies from 10^6 to 0.01 Hz, pointed to another impedance(s) influencing the measured impedance spectra of both AC//AC cells. These additional impedances can clearly be noticed in the enlarged view of high-to medium frequency parts of Nyquist plots presented in Figure 6. For both AC//AC cells shown in Figure 6, inductive impedance responses at the highest frequencies (region I) are followed by prominent semicircle paths (region II). Some differences between two cells, however, can be noticed at lower frequencies. Whereas for the AC-1 cell, the semicircular shape dominated down to ~100 Hz after which an almost vertical (capacitive) response is observed, for the AC-2 cell, a semicircular shape is observed down to ~1000 Hz and then followed by the characteristic –45° phase angle type of response (region III) being prominent down to ~1 Hz. Only below 1 Hz, a capacitive line (region IV) becomes dominating for this AC//AC cell. Slow transition, or prominent –45° phase angle response (region III) for the AC-2 capacitor cell can be related to an inhibited transport of electrolyte within a porous structure of active material having higher thickness generated by higher mass loading.

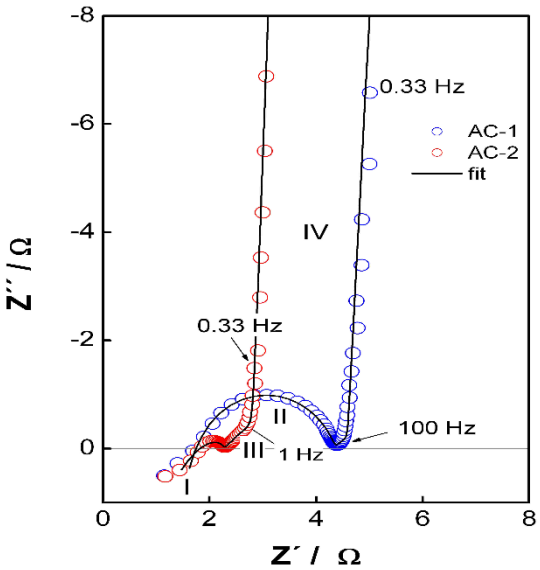

Figure 6. *High-to-medium frequency region of Nyquist plots of AC-1 and AC-2 capacitor cells*

Nyquist plots with four characteristic shapes (I–IV), *i.e.* (inductive, semicircular, –45° and capacitive), have already been observed for EDLC/SC devices [35,43] and discussed here together with eq. (5). In applying eq. (5) as the impedance model equation in the fitting procedure, $Z_s(\omega)$ should be primarily defined. To account for the characteristic impedance –45° shape at

intermediate frequencies followed by an almost purely capacitive response at the lowest frequencies, the TLE concept will be applied. In such a way, $Z_s(\omega)$ in eq. (5) is described in terms of the TLE impedance, $Z(\omega)_{TLE}$, defined by the following relation [2,35,36,40,43,44,47]:

$$Z_s(\omega) = Z_{TLE}(\omega) = R_s(i\omega\tau_s)^{-p} \coth(i\omega\tau_s)^p \quad (11)$$

For highly electronically conducting porous layer, R_s and $C_s = \tau_s/R_s$ in eq. (11) denote the total electrolyte resistance within pores and double-layer capacitance induced at pore walls. In the ideal case, the exponent $p = 0.5$, but due to the same reasoning as for CPE impedance defined by eq. (9), the exponent p in eq. (11) can be lower than ideal 0.5 [35,40], thus making C_s to be similar in its explanation to the CPE parameter T [51]. The characteristic time constant (τ_s) that is determined by pore and electrolyte properties is directly responsible for the characteristic shape of impedance/frequency response. At two ω limits, eq. (11) with p=0.5 becomes reduced to [2,35]:

$$Z_s(\omega\to\infty) = (R_s/C_s)^{0.5}(i\omega)^{-0.5} \quad (12a)$$

$$Z_s(\omega\to 0) = R_s/3 + 1/(i\omega)C_s \quad (12b)$$

Now, it is easy to show that at frequencies higher than $\omega_s = 1/\tau_s$, eq. (12a) defining the phase angle of $-45°$ is operative, while at frequencies lower than $\omega_s = 1/\tau_s$, eq. (12b) is operative describing the ideal R–C response having the phase angle of $-90°$.

Eq. (5) combined with eq. (11) is generally described by six frequency independent impedance parameters (L, R_{HF}, R_{RC}, C_{RC}, R_s and C_s) that are for not ideal impedance responses increased for two more parameters (α and p). The values of these eight frequency independent impedance parameters obtained by CNLS fittings of eq. (5) involving $Z_s(\omega)$ defined by eq. (11) and $Z_{RC}(\omega)$ corrected by eq. (9), to measured impedance spectra of two AC//AC cells are listed in Table 2. The corresponding fitted curves are drawn by full lines in Figures 4 and 6.

Table 2. *Results of CNLS fittings of the eq. (5) combined with eq. (11) to measured impedance spectra of AC//AC capacitor cells*

AC//AC cell	$10^7\times L$/H	R_{HF} / Ω	$10^6\times T_{RC}$ / Fs$^{\alpha-1}$	α	R_{RC} / Ω	R_s / Ω	τ_s / s	p	*T_s / Fs^{2p-1}	χ^2
AC-1	2.60±0.01	1.24±0.03	4.6±0.4	0.82	3.10±0.04	0.71±0.04	0.048±0.003	0.48	0.068	6.9×10^{-4}
AC-2	2.77±0.01	1.0±0.1	3.1±0.4	0.85	1.2±0.1	1.57±0.02	0.428±0.006	0.49	0.273	5.3×10^{-4}

*T_s calculated as τ_s/R_s

Well fitted results indicated by acceptable χ^2 values and low errors of all individual parameters have pointed that eq. (5) was a reasonable model function applied in the impedance analysis of two AC//AC capacitor cells. C_T values calculated from T_s and p values from Table 2 using eq. (10) with $\alpha = 2p$ are listed in Table 3, together with ESR values calculated as ESR = $R_{HF} + R_{RC} + R_s/3$. The corresponding data obtained by the single-frequency method and impedance data plotted in Figures 2, 3 and 5 are also listed in Table 3.

Table 3. C_T *and ESR values of AC-1 and AC-2 capacitor cells obtained by single and multi-frequency methods*

Method		AC-1		AC-2	
	Frequency range	C_T / F	ESR / Ω	C_T / F	ESR / Ω
Single frequency (Fig.3)	--	0.082 (0.01Hz)	3.07 (10^5Hz)	0.297 (0.01Hz)	2.11 (10^5Hz)
Single frequency (Fig.6)	--	0.082 (0.01Hz)	4.36 (10^3Hz)	0.297 (0.01Hz)	2.33 (10^3Hz)
Single frequency (Fig.4)	--	0.082 (0.01Hz)	4.63(0.42Hz)	0.297 (0.01Hz)	2.61 (0.21Hz)
Curve fitting by eqs. (5)+(11)	1×10^6–0.01 Hz	0.065	4.58	0.271	2.72

Comparison of C_T values listed in Table 3 shows that generally lower C_T values were for both AC//AC capacitor cells obtained by the curve fitting procedure performed using eq. (5) combined with eq. (11), than by using the single frequency method and usual approximation $C_T = -1/\omega Z''$ at f = 0.01 Hz. Almost 10–20% lower C_T values obtained for two cells using the multi-frequency method should be ascribed to influence of not ideal responses of capacitances induced at pore walls of AC electrode materials and seen through $2p < 1$ (*cf*. Table 2). ESR values determined by the single frequency method showed significant dependence on the chosen frequency of evaluation, suggesting significant contribution of distributed electrolyte solution resistance within porous AC electrode material to the evaluated data. The present results also show that for here characterized AC//AC cells, the recommended f = 1 kHz is too high for proper ESR evaluations. Only when the frequency of ESR evaluation was rather low, ESR values become similar to that determined by the multi-frequency analysis and curve fitting procedure, where distributed resistance effects have already been taken into account by applying eq. (5) combined with eq. (11).

Conclusions

The characteristic values of total charge capacitance (C_T) and internal resistance (ESR) of two single cell AC//AC capacitors with different quantities of active electrode materials were analyzed using the single and multi-frequency analyses of measured impedance spectra.

Single frequency C_T and ESR values were determined on the basis of ideal *C*–*R* model, using impedance magnitude values measured at low and high (or already recommended) frequencies, respectively. Multi-frequency analysis involving curve-fitting procedure was performed over all measured frequencies and based on the non-ideal *R*–*C* model. Non-ideal *R*–*C* model assumed various impedance contributions including inductive, resistive inherent to the electrode material and/or contacts and that of AC electrode porosity.

Although close C_T and ESR values were generally obtained, not any single frequency result was found to agree with the multi-frequency fitting results. Beneficially higher C_T and lower ESR values were generally obtained using the single frequency method, what can be explained by an assumption of ideal capacitive response and too high frequency value of ESR evaluation. At the other side, lower C_T and higher ESR values obtained using the multi-frequency analysis are based on anticipated contributions from porosity and pore surface inhomogeneity of AC electrode material, which all have been taken into account by the non-ideal *R*–*C* model used for curve fittings.

Acknowledgements: *This work is supported by the Croatian Science Foundation under the Project ESUP-CAP (IP-11-2013-8825). The authors wish to acknowledge Prof. Miran Gaberšček and Dr. Jože Moškon (National Institute of Chemistry, Ljubljana, Slovenia) for their delightful collaboration in this project.*

References

[1] B. E. Conway, *Electrochemical Supercapacitors: Scientific Fundamentals and Technological Applications*, Kluwer Academic Publishers/Plenum Press, New York, USA, 1999.
[2] R. Kötz, M. Carlen, *Electrochimica Acta* **45** (2000) 2483-2498
[3] J. R. Miller, P. Simon, *Science* **321** (2008) 651-652
[4] A. G. Pandolfo, A. F. Hollenkamp, *Journal of Power Sources* **157** (2006) 11-27
[5] P. Sharma, T. S. Bhatti, *Energy Conversion and Managenment* **51** (2010) 2901-2912
[6] A. K. Shukla, A. Banerjee, M. K. Ravikumana, A. Jalajakshi, *Electrochimica Acta* **84** (2012) 165-173.
[7] Y. Wang, Y. Song, Y. Xia, *Chemical Society Reviews* **45** (2016) 5925-5950
[8] J. W. Long, D. Bélanger, T. Brousse, W. Sugimoto, M. B. Sassin, O. Crosnier, *Materials Research Society Bulletin* **36** (2011) 513-522

[9] D. Cericola, R. Kötz, *Electrochimica Acta* **72** (2012) 1-17
[10] M. F. El-Kady, M. Ihns, M. Li, J. Y. Awang, M .F. Mousavi, L. Chaney, A. T. Lech, R. B. Kaner, *Proceeding of the National Academy of Sciences of the United States of America*, *PNAS*, **112** (2015) 4233-4238
[11] E. Frackowiak, F. Béguin, *Carbon* **39** (2001) 937-950
[12] C. Portet, G. Yushin, Y. Gogotsi, *Carbon* **45** (2007) 2511-2518
[13] L.-L. Zhang, X. S. Zhao, *Chemical Society Reviews* **38** (2009) 2520–2531
[14] M. Inagaki, H. Konno, O. Tanaike, *Journal of Power Sources* **195** (2010) 7880-7903.
[15] Y. Li, K. Sheng, W. Yuan, G. Shi, *Chemical Communications* **49** (2013) 291-293
[16] G. Xiong, C. Meng, R.G. Reifenberger, P.P. Irazoqui, T.S. Fisher, *Electroanalysis* **26** (2014) 30-51
[17] C. Lekakou, O. Moudam, F. Markoulidis, T. Andrews, J. F. Watts, G. T. Reed, *Journal of Nanotechnology*, **2011**, ID 409382, 2011. DOI:10.1155/2011/409382
[18] A. Lewandowski, A. Olejniczak, M. Galinski, I. Stepniak, *Journal of Power Sources*, **195** (2010) 5814-5819
[19] M. Arulepp, L. Permann, J. Leis, A. Perkson, K. Rumma, A. Jänes, E. Lust, *Journal of Power Sources*, **133** (2004) 320-328
[20] M. D. Stoller, R.S, Ruoff, *Energy & Environmental Science*, **3** (2010) 1294-1301
[21] F. Rafik, H. Gualous, R. Gallay, A. Crausaz, A. Berthon, *Journal of Power Sources* **165** (2007) 928-934
[22] A. Burke, M. Miller, *Electrochimica Acta* **55** (2010) 7538-7548
[23] J. Eskusson, A. Jänes, A. Kikas, L. Matisen, E. Lust, *Journal of Power Sources* **196** (2011) 4109-4116
[24] N. Devillers, S. Jemei, M.-C. Péra, D. Bienaimé, F. Gustin, *Journal of Power Sources* 246 (2014) 596-608
[25] D. K. Kampouris, X. Ji, E.P. Randviir, C. E. Banks, *Royal Society of Chemistry Advances* **5** (2015) 12782-12791
[26] A. Allagui, T. J. Freeborn, A. S. Elwakil, B. Maundy, *Scientific Reports* **6** 38568 (2016). DOI: 10.1038/srep38568
[27] P. Kurzweil, *Proceedings of the 14th International seminar on double-layer capacitors*, Deerfield Beach, Fl. USA, Dec. 6-8 2004
[28] R. Kötz, M. Hahn, R. Gallay, *Journal of Power Sources*, **154** (2006) 550-555
[29] M. Itagaki, S. Suzuki, I. Shitanda, K. Watanabe, *Electrochemistry* **75** (2007) 649-655.
[30] F. Lufrano, P. Staiti, M. Minutoli, *Journal of Power Sources* **124** (2003) 314-320
[31] P.L. Taberna, P. Simon, J.F. Fauvarque, *Journal of the Electrochemial Society* **150** (2003) A292-A300
[32] C. Portet, P.L. Taberna, P. Simon, C. Laberty-Robert, *Electrochimica Acta* 49 (2004) 905-912
[33] A. Jänes, E. Lust, *Journal of Electroanalytical Chemistry* **588** (2006) 285-295
[34] P. L. Taberna, C. Portet, P. Simon, *Applied Physics A: Materials Science & Processing* **82** (2006) 636-646
[35] O. Bohlen, J. Kowal, D.-U. Sauer, *Journal of Power Sources* **172** (2007) 468-475
[36] A. Hammar, R. Lallemand, P. Venet, G. Coquery, G. Rojat, J. Chabas, https://hal.archives-ouvertes.fr/hal-00411480 (01.12.2017)
[37] J. R. Miller, R. A. Outlaw, B. C. Holloway, *Science* **329** (2010) 1637-1639
[38] K. Sheng, Y. Sun, C. Li, W. Yuan, G. Shi, *Scientific Reports* **2** 247 (2012) DOI: 10.1038/srep00247
[39] X.-Z. Sun, X. Zhang, B. Huang, Y.-W. Ma, *Acta Physico-Chemica Sinica* **30** (2014) 485-491
[40] B. Batalla Garcia, A. M. Feaver, Q. Zhang, R.D. Champion, G. Cao, T.T. Fister, K.P. Nagle, G. T. Siedler, *Journal of Applied Physics* **104** 014305 (2014). DOI:10.1063/1.2949263
[41] L. Zheng, X. Hu, Z. Wang, F. Sun, D.G. Dorrell, *Journal of Power Sources* **287** (2015) 129-138
[42] Z. Wu, L. Li, Z. Lin, B. Song, Z. Li, K.-S. Moon, C.-P. Wong, S. L. Bai, *Scientific Reports* **5** 10983 (2015). DOI:10.1038/srep10983
[43] E. Karden, S. Buller, R. W. De Doncker, *Electrochimica Acta* **47** (2002) 2347-2356
[44] X. Zhang, Y. Sun, J. Song, A. Wu, X. Cui, *Journal of Applied Mathematics* 2014, ID 726108 http://dx.doi.org/10.1155/2014/726108
[45] S. Fletcher, V.J. Black, I. Kirkpatrick, *Journal of Solid State Electrochemistry* **18** (2014) 1377-1387
[46] R. De Levie, *Advances in Eletrochemistry and Electrochemical Engineering* **6** (1967) 329-397
[47] M. Itagaki, S. Suzuki, I. Shitamida, K. Watanabe, H. Nakazawa, *Journal of Power Sources* **164** (2007) 415-424

[48] S. Sopčić, Z. Mandić, D. Antonić, J. Moškon, M. Gaberšček, *6th Regional Symposium on Electrochemistry of South-East Europe, Book of Abstracts*, Balatonkenese, Hungary, 2017, p. 123.
[49] A. W. Bott, *Current Separators* **17** (1998) 53-59
[50] Q. Meyer, S. Barass, O. Curnick, T. Reisch, D. J. L. Brett, *Journal of Electrochemical Science and Engineering* **3** (2013) 107-114
[51] K. Magdić, K. Kvastek, V. Horvat-Radošević, *Electrochimica Acta* **117** (2014) 310-321
[52] G. J. Brug, A. L. G. Van den Eeden, M. Sluyters-Rehbach, J. H. Sluyters, *J. Electroanal. Interf. Chem.* **176** (1984) 275-295
[53] B. Hirschorn, M.E. Orazem, B. Tribollet, V. Vivier, I. Frateur, M. Musiani, *Electrochimica Acta* **55** (2010) 6218-6227